Development and Application of a XUV Laser Light Source for Photoelectron Spectroscopy of Solutions

Im Fachbereich Physik der Freien Universität Berlin eingereichte Dissertation zur Erlangung des Grades eines Doktors der Naturwissenschaften (Dr. rer. nat.)

vorgelegt von:

Jan Metje

angefertigt am:

Helmholtz-Zentrum Berlin für Materialien und Energie
Institute of Methods for Material Development
Albert-Einstein-Straße 15
12489 Berlin

September 2016

Gutachter:	Prof. Dr. Emad F. Aziz
Zweitgutachter:	Prof. Dr. Bernd Abel
Disputation:	14.12.2016

Contents

List of Figures

Abbreviations

AC	autocorrelation
ATI	above threshold ionization
BBO	barium borate
CC	cross correlation
CCD	charge coupled device
CTTS	charge-transfer-to-solvent
DM	drift mode
DMSO	dimethyl sulfoxide
DSSC	dye-sensitized solar cell
EAL	effective electron attenuation length
FEL	free electron laser
FROG	frequency resolved optical gating
FWHM	full width at half maximum
HHG	high harmonic generation
HOMO	highest occupied molecular orbital
IMFP	inelastic mean free path
IR	infrared
LAPE	laser assisted photoemission
LUMO	lowest unoccupied molecular orbital
MCP	multi-channel plate
MD	molecular dynamics
NMR	nuclear magnetic resonance
OPA	optical parametric amplifier
ORZP	off-axis reflection zone plate
PES	photoelectron spectroscopy

PEY	partial electron yield
RMS	root mean square
SFA	strong field approximation
SHG	second harmonic generation
SPIDER	spectral phase interferometry for direct electric-field reconstruction
TDCM	time-delay compensated monochromator
TEY	total electron yield
TOF	time-of-flight
TPP	tetraphenylporphyrin
UHV	ultra-high vacuum
UV	ultraviolet
VBE	vertical binding energy
VIS	visible
WAM	wide angle mode
XUV	extreme ultraviolet

1. Introduction

Since the early days of laser physics, it has been the aim to extend the available range of photon energies beyond spectral regions of infrared (IR), visible and ultraviolet (UV) light, yet preserving the special characteristics of laser light. Besides the research for novel active laser media, the quest for new wavelengths always included the use of nonlinear optics. Today, a large spectral region from deep UV to far IR range is made accessible by converting laser light in nonlinear optical processes occurring in crystals. For photon energies larger than those in the UV range, the large number of atomic and molecular resonances in any medium leads to high absorption of radiation. Therefore, crystals are inefficient for nonlinear optical applications involving photons exhibiting energies much above 7 eV [1, 2]. Even the absorption in air is so high that experiments with such radiation have to be conducted in an ultra-high vacuum (UHV) environment, making them technically even more demanding. Nevertheless, it is this strong interaction with matter that makes UV, extreme ultraviolet (XUV) and soft X-ray radiation such a valuable tool for an experimentalist to study physical and chemical properties of matter such as bonding or charge transfer. For these experiments, a tunable light source providing radiation from the UV to X-ray range, ideally delivered in short pulses for a high time resolution, is needed. Large scale facilities such as synchrotrons cover this range of photon energies and have provided invaluable results, but their time resolution is usually limited to picoseconds. Free electron lasers (FELs) have started to operate in a similar region of photon energies, while providing ultrashort pulses at the same time. For time resolved studies, where the FEL probe pulse has to be synchronized with a laser pump pulse, the temporal resolution is often limited to values above 100 fs due to a time jitter introduced in the FEL cavity [3].

This problem is circumvented through intrinsic synchronization, when the XUV probe pulse is generated from the same laser as the pump pulse. Here, the technique of high harmonic generation (HHG) in rare gases comes into play. The occurrence of odd harmonics of an intense laser field has been observed as early as the late 1970s and 80s [4, 5]. At medium laser intensities, where the strength of the atomic field is much larger than that of the electric field of the laser, nonlinear optical processes can be described in terms of perturbation theory. With the availability of more powerful lasers producing intensities in the range of 10^{14} W/cm^2 and above, new nonlinear phenomena emerged, which could not be explained in the framework of perturbation theory any more. New theoretical description for these cases had to be invented. Among different approaches based on both, fully quantum mechanical and semi-classical treatments, the "three-step model" introduced by Corkum [6] has received the greatest attention. It allows a basic understanding of high harmonic generation.

The potential of the HHG process to serve as a small-scale source for XUV laser light has been proposed soon after its discovery [7]. Since then, numerous experimental setups have been developed further increasing the range of applications for XUV lasers. These include photoelectron spectroscopy (PES), both time-resolved [8, 9] and static [10, 11], generation of attosecond pulses [12] and their application, seeding of FELs [13–16] and microscopy applications[17–20]. Each of these approaches results in a setup which has special features suitable for the desired application. Especially the development of modern femtosecond laser technology has allowed to study ultrafast electron dynamics in time-resolved PES experiments with XUV light pulses. With the use of Ti:sapphire lasers driving the HHG process, XUV light pulses with femtosecond duration and photon energies up to 100 eV can be generated [21]. When mid-IR lasers are used, photon energies in the keV range can be generated in the high harmonic process [22]. Thereby, these light sources compete against third generation synchrotrons [23] and free electron lasers.

In the present work, a setup employing femtosecond XUV light from high harmonic generation was developed for time-resolved PES of liquids. While such setups have been described already, the distinctiveness of this device lies in the new way pursued to conserve the ultrashort time duration of the laser pulses. In spectroscopy experiments employing conventional XUV gratings, light pulses are inevitably stretched, thereby deteriorating the good time resolution originally provided by the laser. Sophisticated grating techniques have been invented to circumvent this problem, often at the expense of photon flux. In the present setup, a new type of monochromator based on a single off-axis reflection zone plates (ORZPs) will be employed instead.

While the first part of the manuscript is devoted to the development and characterization of the experimental setup with a focus on the zone-plate monochromator, the second part describes applications of XUV PES on liquids. In a PES experiment, the incident electromagnetic radiation maps the structure of the occupied electronic states onto continuum states above the vacuum level. The electronic structure of the occupied states is then inferred from the measured kinetic energy distribution of the free electrons. Through this direct measure of the energy of occupied states, various properties such as chemical environment, solvation or the life times of excited states can be investigated. For decades, PES has been used for the characterization of gases and solid materials. High quality radiation produced by lasers, synchrotrons and FELs has lead to a wealth of results. Nevertheless, the potential of PES experiments is not exhausted yet, with new fields emerging such as PES of liquids or PES under near-ambient conditions.

Specifically, the setup will be tested for two fields of application. In the first test study, steady state XUV photoelectron spectroscopy of aqueous sodium halide solutions of varied ion concentration are taken.

The second test study evaluates the capability of the setup to acquire transient photoelectron spectra of porphyrin solutions for the case of a hemin-dimethyl sulfoxide (DMSO) solution.

Part I.

High-harmonic laser light monochromatized with reflection zone plates

2. Introduction to Part I

The first part of the thesis describes the development and characterization of the experimental setup for time-resolved PES of liquids. As outlined in the main introduction, the setup is based on the generation of ultrashort XUV light pulses via the technique of HHG. To understand and optimize the harmonic generation, the three-step model presented by Corkum [6], which explains the HHG process in a microscopic picture, is described. A description of the macroscopic parameters influencing phase matching, which is the key for efficient harmonic generation, is included.

The resulting XUV spectrum incorporates a large number of odd harmonics of the driving laser. For a spectroscopic experiment, a single harmonic has to be selected with a high spectral purity and focused to the interaction region of the PES experiment. Spectral selection is routinely accomplished by monochromators based on diffraction gratings. However, these monochromators induce a path difference of the beam trajectories, that results in a tilt of the pulse front. The pulse front tilt translates to a large temporal stretch of the light pulses. This is unfavorable for ultrafast applications. Therefore, special effort is taken in the present work to reduce the pulse shape distortion. The monochromator employed here is based on an adaption of a reflective Fresnel zone plate, which has been widely used in X-ray imaging [24–26]. In contrast to the imaging applications, where a full elliptical structure is used, the zone plate for monochromation developed at BESSY II for this work makes use of only a peripheral fraction of the structure, thus being called an off-center reflection zone plate (ORZP).

This novel type of monochromator combines reflection, focusing and dispersion properties in one optical element, thus offering a high transmission, a high spectral purity and good pointing stability of the XUV beam. So far, the potential of ORZP monochromators in the XUV range has been shown before only with respect to its chromatic and focusing properties [27]. In the soft X-ray range, such a monochromator is currently employed in the femto-slicing beamline at the synchrotron BESSY II, monochromatizing synchrotron light pulses with a duration of 100 fs [28]. The present work presents the first combination of an ORZP monochromator with a HHG light source, enabling to conduct ultrafast time-resolved PES experiments in the XUV range with femtosecond time resolution. The expected advantage of the zone-plate monochromator is its high efficiency pared with a low time distortion of the XUV pulses.

A detailed description of the ORZP is given in a separate section of this part and it is compared to other commonly used techniques for monochromatizing XUV light, such as diffraction gratings and multilayer mirrors.

The UHV system that was developed for harmonic generation and the delivery of

monochromatized XUV light pulses to the interaction region of the PES experiment is described in detail below. This includes the design of the UHV-compatible mechanics for positioning the zone-plate monochromator and the refocusing mirror.

The performance of the ORZP monochromator as dispersive element for ultrashort XUV light pulses is inferred theoretically and experimentally. The results of ray-tracing studies acquired during the optimization of the ORZP structure are presented. A series of experiments have been performed to measure the key parameters of the monochromatized light. These include the determination of the XUV focus size at the interaction region of the PES experiment, the evaluation of the spectral purity and spectral bandwidth of the monochromatized HHG light, and, most importantly, the duration of the monochromatized XUV pulses.

In the summary of the first part of the manuscript, the results acquired for the ORZP are compared to the key parameters reported for other grating-based setups. These include setups based on double-grating time-delay compensated monochromators (TDCMs), which represents a competing approach specially designed for ultrafast applications.

3. Concepts of high harmonic generation and monochromators

3.1. Basic theory for high harmonic generation

The theoretical description of the HHG process of IR lasers in noble gases involves two aspects: the microscopic response of individual gas atoms, and the macroscopic response of the nonlinear medium, which arises from the coherent sum of the atomic contributions. The single-atom response is described on the basis of a semi-classical model developed by Corkum [6], which delivers the major characteristics of the process. The employment of the HHG process as a basis for a table-top XUV light source requires an efficient macroscopic response of the nonlinear medium. Therefore, the relevant parameters for maximizing the coherent sum of the atomic contributions are evaluated.

3.1.1. High harmonic generation on the atomic level: the three-step model

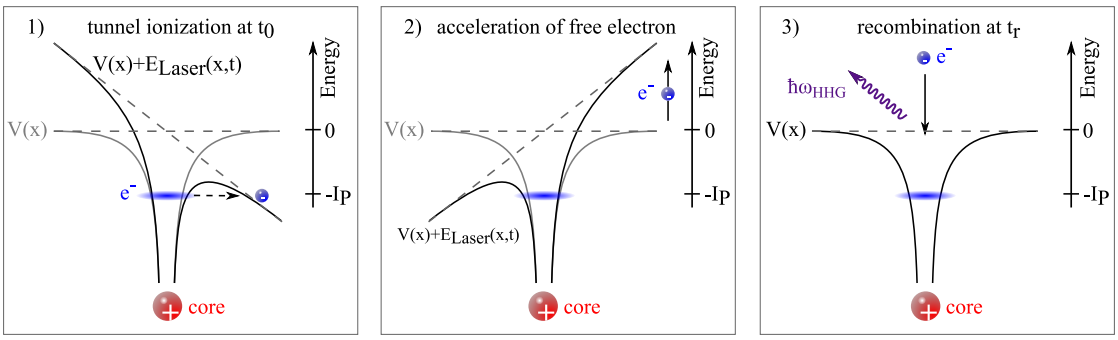

Figure 3.1.: Scheme of the three-step model describing high harmonic generation. The three steps are: 1) tunnel ionization, 2) acceleration of the free electron away from and back to the parent ion, and 3) recombination of the electron with its parent ion leading to the emission of a high energy photon $\hbar\omega_{HHG}$.

Perturbation theory is based on the assumption that the electric field of the laser is smaller than the atomic electric field. While this applies for low-order nonlinear optical processes, it is not valid anymore for high-order processes involving laser intensities of 10^{14} W/cm^2 and above. Other models have to be used in this strong

field regime to describe processes such as HHG. The simplest model describing the HHG process is the so called three-step model developed by Corkum [6]. The three steps of this semiclassical model, which are also illustrated in figure 3.1, are:

1. Tunnel ionization of a bound electron resulting in a free electron of zero kinetic energy.
2. Acceleration of the free electron in the external laser field away from and back to the parent ion.
3. Recombination of electron and parent ion to the ground state atom under emission of a photon.

Initially, the electrons are bound in the atomic potential V(x). Application of a strong electric field from a focused intense laser results in a distorted potential V(x)+E_{Laser}(x,t). In this strongly asymmetric potential exists a probability for an electron to tunnel through the low side of the potential barrier. This quantum mechanical effect is called tunnel ionization and results in a free electron of zero kinetic energy.

In the second step, this free electron is then accelerated in the oscillating laser field away from and back to the parent ion. Subject to the phase of the laser, the electron can gain a large kinetic energy during this step as shown in the curse of this section. The motion of the electron is described in the framework of classical mechanics. It is required that the driving laser for HHG should exhibit a high degree of linear polarization, since otherwise the free electron would not return to the parent ion.

The electron recombines with its parent ion to the ground state in the third step, emitting a single photon of high energy $E_{HHG} = \hbar\omega_{HHG}$. Hereby, E_{HHG} is the sum of the kinetic energy acquired by the electron in the second step and the atomic ionization potential I_p:

$$E_{HHG} = E_{kin} + I_p \quad . \tag{3.1}$$

Analysis of the second step

A detailed analysis of the classical motion of the electron in the laser field within the second step yields some of the basic properties of the high harmonic spectrum. The motion of the accelerated electron can be described by the following differential equation:

$$m_e\ddot{x} = -eE_{Laser}(x,t)\ cos\,(\omega t) \tag{3.2}$$

with m_e being the electron mass, e denoting the electron charge and $E_{Laser}(x,t)$ describing the envelope of the laser pulse. Assuming that this envelope is constant within one cycle of the optical field, the integration of equation (3.2) results in:

$$\dot{x} = \dot{x_0} - \frac{eE}{m_e\omega}\ sin\,(\omega t) \tag{3.3}$$

Furthermore taking the assumption that the free electron has zero kinetic energy directly after tunnel ionization ($\dot{x_0} = 0$) yields the mean kinetic energy averaged over one laser cycle, which is called ponderomotive energy U_p:

$$U_p = \frac{e^2 I}{2 m_e c \epsilon_0 \omega^2} \quad . \tag{3.4}$$

Analysis of the above equations yields the result that electrons can only return to the parent ion and recombine with it if they are released at a phase of the laser cycle larger than $\pi/2$. This result directly leads to the fact that the harmonic spectrum exhibits a maximum energy U_r^{max}, that constitutes the cut-off law:

$$U_r^{max} = 3.17\ U_p + I_p \tag{3.5}$$

From equations (3.4) and (3.5) it can be easily verified that there are three possible ways to increase the cut-off energy U_r^{max} and thereby the available spectral range of the high harmonic radiation. Firstly, a higher laser intensity will result in a higher ponderomotive energy and, thus in an increase of the cut-off energy. This method is only possible up to a specific saturation value I_{sat}, though. Secondly, a driving laser with a lower frequency ω can be used. Nowadays, IR radiation from Ti:sapphire lasers or optical parametric amplifiers (OPAs) are routinely used, as they provide high intensities together with ultrashort pulses. Thirdly, the choice of a generation medium with a higher ionization potential I_p increases the cut-off. It has been shown that the use of Helium and application of mid-IR frequencies allows to generate high harmonics up to the keV region [22].

While the three-step model describes the occurrence of high harmonics and the existence and location of the cut-off energy fairly well, it fails to explain the restriction of the HHG light to odd harmonics, though. In classical mechanics, a free electron should be able to acquire any kinetic energy below the cut-off energy in the electric field of the laser, depending on its time of ionization with respect to the phase of the electric field. Thus, the occurrence of odd harmonics has to be added a posteriori. The same argument that is routinely used to explain the absence of even harmonics in low-order nonlinear optical processes in centrosymmetric systems holds for high harmonic generation in gases. In the dipole approximation, the even order nonlinear susceptibilities vanish in centrosymmetric media. Therefore, no even order harmonic processes are observable. In the case of high harmonic generation, the volume filled with a gas represents a centrosymmetric medium, which explains the absence of even order harmonics. An alternative way to explain the restriction to odd harmonics applies selection rules for dipole transitions.

A model that delivers odd harmonics intrinsically is the Lewenstein model [29]. This quantum mechanical approach makes use of the strong field approximation (SFA). SFA and Lewenstein model are not presented in this work, since the depth of the results of this model exceeds the parameters necessary for the design and the operation of the beamline based on a HHG light source.

3.1.2. High harmonic generation on the macroscopic level: phase matching for high conversion efficiencies

The three-step model presented in section 3.1.1 describes the single atom response of the nonlinear medium to the high intensity driving laser. For an efficient conversion of IR photons to XUV photons, different atoms in the medium have to respond coherently to the IR field. This can be achieved by minimizing the phase difference that is built up between the IR and XUV radiation during the generation process along the path of the light. This minimization is called phase matching. The phase difference $\delta\Phi_q$ accumulated between the infrared laser field and its q-th harmonic along the propagation direction z is described by He *et.al.*[30] as:

$$\delta\Phi_q(z,t) = \int \Delta k_q(z',t)dz' + q\ arctan\left(\frac{z}{z_R}\right) + \alpha_j I(z,t) \tag{3.6}$$

This phase difference has three contributions. The first term in equation (3.6) describes the phase build-up due to the propagation of the IR and XUV radiation in the partially ionized gas. The difference in k-vectors:

$$\Delta k_q(z,t) = k_{XUV} - k_{IR} \tag{3.7}$$

due to dispersion within the nonlinear medium is influenced by the presence of neutral atoms and free electrons [31, 32]. Since the gas density is spatially non-uniform within the generation volume, with a lower value at the edges of the interaction region, the density of ionized electrons follows this non-uniformity as well. Additionally, the amount of free electrons follows the temporal and spatial intensity profile of the laser beam. As a result, the k-vector mismatch $\Delta k_q(z,t)$ is a function of space and time. The second term in equation (3.6) accounts for the Gouy phase introduced by focusing a Gaussian beam, where z_R denotes the Rayleigh length of the laser focus. The third term denotes the phase accumulated by the free electron during the second step of the three-step model. Thereby, α_j denotes the specific proportionality factor eligible for a given harmonic and a given electron trajectory (long or short)[30].

While the individual contributions to the phase difference between IR driving laser and XUV harmonic radiation can be calculated [30, 32], in a practical application phase matching can be achieved by controlling the following parameters:

- The power of the driving laser, which determines the laser intensity within the generation medium. Thereby it influences $\Delta k_q(z,t)$ due to the ionization rate of the medium and the phase accumulated during the motion of the free electron.

- The gas pressure also influences $\Delta k_q(z,t)$ due to the amount of atoms in the generation volume. It also influences the amount of reabsorption of the XUV light by the medium [33]. Though the latter effect is not related to phase matching itself, it influences the conversion efficiency of the nonlinear process.

- The Rayleigh length of the focus and its position with respect to the medium determine the Gouy phase and also influence the local pump intensity within the nonlinear medium. Hence focal position and laser power are coupled parameters.

- The length of the generation medium along the direction of light propagation.

The subsequent sections describing the experimental setup for high harmonic generation will refer to the mentioned parameters and the equipment chosen for their control.

3.1.3. Technical approaches for high harmonic generation

Different approaches for generating high harmonic radiation in noble gases from high-intensity lasers have been developed. In the straightforward way, a focused laser beam is overlapped with a gas jet. While this approach requires the least alignment effort, the conversion efficiency remains low due to little control of the phase matching parameters presented in the previous section. This is because the interaction length of the nonlinear medium and the local gas pressure are difficult to control. Furthermore, since the gas quickly spreads in the vacuum, a large amount of gas is consumed. The gas consumption can be reduced by employing a pulsed gas valve synchronized with the laser pulse [9]. Phase matching parameters are still difficult to control, but the efficiency is increased if a sequence of pulsed gas valves is connected in a series [34].

The control of phase matching is facilitated if the harmonic radiation is generated in a gas-filled cell [30]. Then, the interaction length can be chosen, and larger, more defined values of the gas pressures can be applied without increasing the gas consumption much. Since the entrance and exit apertures of the cell have to be overlapped with the laser beam, the alignment effort is larger. This is usually encountered by the use of replaceable gas cells, into which the laser drills its own apertures.

Further control of phase matching parameters and even higher efficiencies are achieved if the harmonic radiation is generated in a gas filled hollow fiber [35]. Then, the length of the nonlinear medium and the gas pressure can be greatly increased if the laser runs in a self-focusing mode of the fiber. Gas pressures as high as 80 bar [22] can be applied.

3.2. Techniques for monochromation of XUV light

The requirements imposed upon monochromators are outlined in the following list. A monochromator should:

- possess sufficient dispersion power to separate the spectral regions of interest with a high suppression of neighboring harmonics

- exhibit a high transmission in the desired spectral range
- refocus the divergent XUV radiation to the interaction region
- maintain a high temporal resolution
- provide pointing stability upon change of spectral region

Several concepts of monochromators are presented in the following section and reviewed according to the above mentioned requirements. Not all requirements can be optimally fulfilled at the same time, though.

3.2.1. Diffraction gratings

Selecting a specific region out of a spectrum provided by e.g. a synchrotron source or a HHG light source, is routinely done by diffraction gratings. The periodic structure of transparent lines from a transmission grating, or of grooves from a reflection grating, leads to a strong interference pattern of the beam behind the grating. The spectrally dependent redirection of the radiation in the interference pattern allows the selection of a specific spectral interval. Diffraction theory is extensively described in the literature [36, 37] and many experiments using high harmonic laser radiation employ diffraction gratings for spectral selection [9, 11, 38, 39]. The famous Bragg-formula for the diffraction angles α, in which constructive interference occurs, has the form:

$$n\lambda = d\ sin\,(\alpha) \tag{3.8}$$

Here, λ denotes the wavelength, n represents the diffraction order and d is the distance between the grooves of the grating. The geometrical condition for constructive interference in a certain direction is fulfilled when the path difference between rays reflected from adjacent facets of the grating equals a multiple of the wavelength. As a direct consequence of this relation, the temporal envelope of an ultrashort light pulse is affected. Pulses are inevitably stretched in time. The inflicted time delay can be estimated when the first diffraction order is considered, where the mentioned path difference equals one wavelength. Assuming a grating with 500 lines per millimeter, which is a typical line density for XUV monochromators [38, 40], a wavelength of 38 nm and a light spot of one millimeter size, the path difference for the outermost rays is as large as 19 μm. This translates into a time delay of nearly 64 fs for each millimeter spot size. Since the gratings in XUV and soft X-ray applications are usually used in grazing incidence to maintain a high reflectivity, light spots have large footprints and ultrashort pulses are easily stretched to a couple of hundred femtoseconds or even a few picoseconds.

Grating-based monochromators provide high spectral selection but exhibit medium transmission efficiency of approximately 10 % [41]. Refocusing of the diffracted, divergent radiation can be accomplished by using curved gratings [38] or plain gratings together with refocusing mirrors. Spherical or toroidal gratings

are much more complicated to produce, and therefore more expensive. The incorporation of focusing mirrors naturally reduces the overall efficiency of the system. The efficiency of a grating-based monochromator can be greatly increased by using blazed gratings [41].

Time-delay compensated grating monochromators

Sophisticated techniques have been developed to overcome the problem of temporal stretch inflicted on a light pulse by diffraction gratings. A common approach is the installation of a second grating in the beam path. This grating is mounted in the way that the monochromatized light is incident at an angle which is equal to the angle of the opposite diffraction order used by the first grating. In this geometry, the path difference induced by the first grating is compensated by the second grating, and the resulting temporal stretch is zero. Such a monochromator is therefore called time-delay compensated monochromator (TDCM). The potential of a setup employing a TDCM to compress XUV pulses has been investigated by Villoresi [42], showing that a path length difference of a few micrometers can been achieved.

Although setups employing a TDCM offer exceptional short pulses, their transmission efficiency is usually very small, in the order of a few percent [43]. This is a consequence of their design, which typically includes two gratings and up to four mirrors [11]. Here, the good temporal characteristics of these monochromators are traded off at the expense of photon flux. The larger number of optical elements also makes alignment more complicated and reduces the pointing stability of the system.

A TDCM exhibiting a higher efficiency was presented by Poletto *et.al.* [44]. By incorporating two blazed gratings which are, in contrast to a traditional geometry, illuminated along their grooves, allows for an efficiency of 18 % together with a XUV pulse duration of 8 fs.

3.2.2. Multi-layer mirrors

The reflection coefficient of materials is very small for XUV radiation and X-rays if the incident angle is smaller than the critical angle which marks the onset of total external reflection. Nevertheless, the overall reflectivity of a mirror can be greatly increased if its surface is covered with alternating layers of materials exhibiting suitable thickness and refractive index. Then, the reflections from usually 100-1000 layers interfere constructively, thus resulting in a high reflectivity. These multilayers either consist of a heavy and a light material, e.g. W and C, where the layer of the heavy material is much thinner than that of the light material $d_A \ll d_B$. Or they are made of two light materials of similar thickness $d_A \approx d_B$, e.g. Si and Al. Analogous to the Bragg diffraction of X-rays in a crystal lattice, constructive interference of X-rays reflected from a multi-layer mirror is achieved when the path difference between adjacent reflections equals multiples of the wavelength λ:

$$n\lambda = 2\ d\ sin\,(\theta_m)\ , \tag{3.9}$$

with d=d_A+d_B being the thickness of a pair of layers and θ_m being the incident angle of the X-rays. From equation (3.9), it is obvious that a multi-layer mirror is designed to maximize the reflection coefficient only for specific wavelength and incident angle. The wavelength range can be changed by varying the incident angle, though. Accordingly, such multilayer mirrors can be regarded as volume gratings and employed for spectral selection of harmonics. Due to the high reflection coefficient of the multilayer structure, monochromators based on such mirrors yield high transmission efficiencies. If a high reflection coefficient can be achieved with a few hundred layers only, then multilayer mirrors exhibit also excellent time characteristics. However, despite that they are designed for a specific wavelength, their reflectivity for adjacent spectral regions is too large to sufficiently suppress neighboring harmonics.

An example of a monochromator for HHG radiation between 66 eV and 73 eV based on two multilayer mirrors was presented by Siffalovic *et.al* [8]. The low temporal stretch of only 2 fs induced to the XUV pulses and the constant pointing of the HHG beam are advantages of the device. With the ratio of neighboring harmonics being 10:1, it has limited selectivity, though.

The possibilities to realize a time compensated monochromator based on multilayer mirrors has been investigated by Poletto *et.al.* [45]. Such a device is capable of delivering XUV pulses of 8 fs duration over a large range of photon energies at constant beam pointing. With two additional reflections from normal toroidal mirrors for collimating and focusing the beam at the entrance and exit of the monochromator, the transmission efficiency of the device is decreased to 5 %. Furthermore, the change of photon energy requires to tilt both mirrors and additionally to move one, which increases the alignment effort and decreases the pointing stability of the system.

Only recently, a multilayer mirror for ultrafast spectroscopy below 100 fs designed for XUV radiation from a FEL has been presented [46], though a precise pulse length is not given.

3.2.3. Zone plates

In traditional optics, a Fresnel zone plate is a diffractive structure of alternating transparent and opaque circular areas. Radiation transmitted through the transparent areas of the structure propagates an additional path compared to radiation propagating through the center of the structure (see figure 3.2). If the additional path length equals a multiple of the wavelength λ, constructive interference occurs. Therefore, a zone plate acts like a condenser lens. The description of zone plates given by Myers [47] yields the same formula as for a thin lens $\frac{1}{f} = \frac{1}{R_1} + \frac{1}{R_2}$, where f denotes the focal length of the lens, R_1 is the distance to the object, and R_2 is the distance to the image. Since a zone plate focuses due to diffraction, it represents a highly chromatic device, where each wavelength experiences a different focal length.

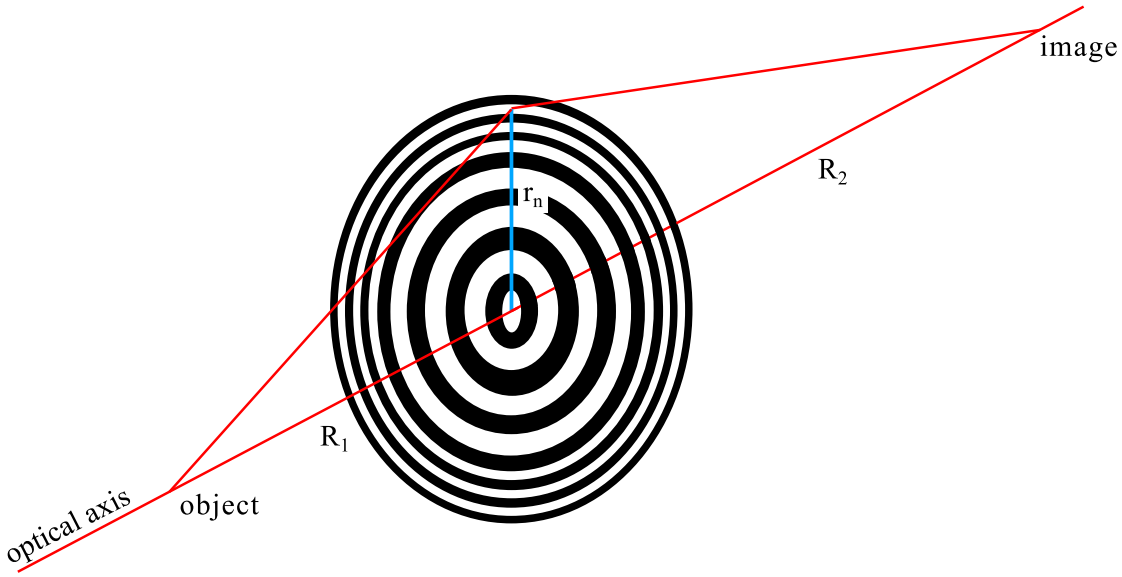

Figure 3.2.: Scheme of a traditional zone plate used in transmission geometry. The red lines indicate the path of the central ray (optical axis), and a ray passing through an outer zone with radius r_n (light blue). The distance from the object to the zone plate is denoted by R_1, and the distance from the zone plate to the image is denoted by R_2.

The focal length f of a zone plate follows the equation:

$$f = \frac{r_n^2}{2n\lambda} \tag{3.10}$$

with r_n being the radius of the n^{th} zone and λ being the wavelength. Since its focal length depends on the wavelength, the zone plate can also be employed as a monochromator. This can be especially beneficial in applications where strongly divergent radiation has to be collected, and at the same time monochromatized. Usually two optical elements, one for collimation and one for dispersion, would have to be used in such a case. The zone plate acts as a condenser lens with a high numerical aperture and as a monochromator at the same time, thus making a second element obsolete. This was demonstrated by Voigt *et.al.* [48] in the case of monochromatizing XUV radiation from a plasma source. In such applications, apertures of suitable size have to be placed in the beam path after the zone plate to block unwanted spectral regions which would deteriorate the resolution. This is especially true for the zeroth order, which propagates along the optical axis and can be blocked by a opaque center of the zone plate structure. Voigt *et.al.* [48] reported a resolution of $\Delta\lambda/\lambda = 600$.

3.3. The off-axis reflection zone plate

The applicability of a Fresnel zone plate to monochromatize XUV radiation can be considerably increased compared to a conventional full-circle zone plate described in the previous section. Firstly, to obtain an efficient optical device for the spectral range of XUV light, the circular structure of the zone plate is projected onto a reflecting plain surface [49], making it suitable for photon energies from 1 to 1500 eV as it was first suggested by Basov *et.al.* [50]. The resulting pattern of circular grooves is depicted in light blue color in figure 3.3. Secondly, the incident harmonic light impinges the reflecting structure under a grazing incidence angle to achieve a high reflectivity. Thirdly, the most notable difference compared to a conventional full-circle zone plate is the fact that not the full elliptical lens structure is illuminated, but only an outer part of the structure marked in deep blue color [50, 51]. This off-axis illumination turns the reflection zone plate into

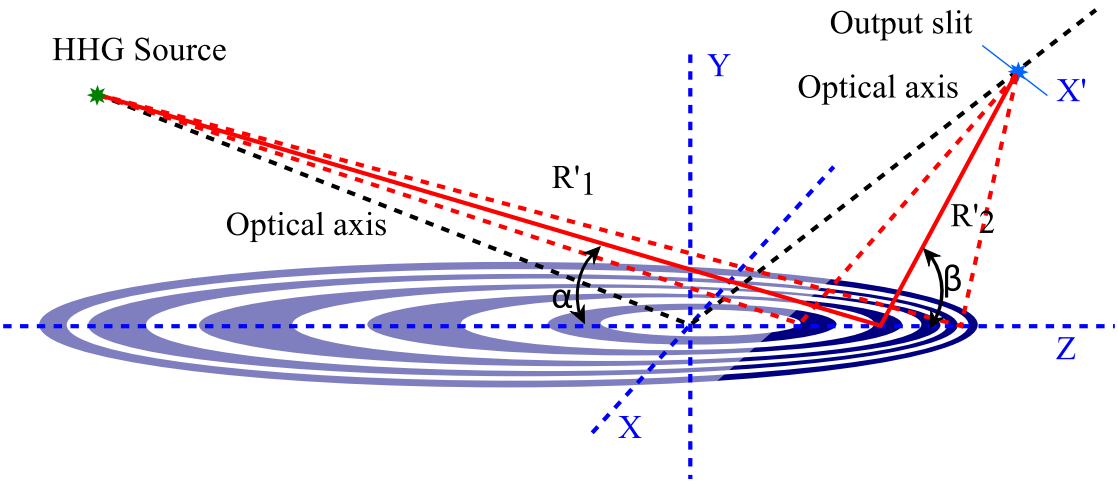

Figure 3.3.: Scheme of an off-axis reflection zone plate. The elliptical structure of a traditional zone plate is depicted in light blue while the off-axis area that is actually illuminated is marked in dark blue color. Each wavelength is diffracted and focused by the structure to different points on the optical axis. R_1 denotes the distance from the HHG source to the center of the zone plate and R_2 denotes the distance to the focal spot. R'_1 and R'_2 indicate the relevant distances to the center of the off-axis area. Reprinted with permission from ref. [52].

an ideal monochromator. Although the radiation incident onto this section is not propagating along the optical axis anymore, it is still diffracted to points that lie on the optical axis. Hence, each wavelength does not only experience its own focal length, as described in equation (3.10), but now it also follows its own propagation direction downstream of the zone plate, which is different from the optical axis. Therefore, the structure of an ORZP can be designed to focus the first diffraction order of a specific wavelength to a point at a certain position. A slit placed at that position transmits the desired harmonic but blocks all other harmonics, which

are diffracted and focused differently. Additionally, the specular reflex (zero-order reflection) can be easily separated. Thus, the ORZP combines the advantages of a traditional zone plate with a high spectral separation due to the high off-center line density. Since the exact location of the illuminated area on the elliptical structure can be freely chosen, the path length difference of the diffracted light can be tuned so that the introduced pulse stretch can be kept below a chosen maximum. This can only be done at the expense of energy resolution, so that a balance has to be found for the layout of the zone plate for a specific application.

Additional to the mentioned advantages, the focusing properties of the zone plate monochromator supersede the use of additional focusing mirrors in the beamline, thus increasing the throughput of the whole system.

Just as for the conventional zone plate, the geometrical demagnification factor M of the ORZP is given by the ratio of entrance arm R_1' and exit arm R_2' (see figure 3.3):

$$M = \frac{R_2'}{R_1'} \tag{3.11}$$

making it possible to adjust the spotsize of the XUV radiation downstream of the monochromator to the size of the sample (in the present work the liquid jet). With a HHG source size ΔS, and a given demagnification M, the focal spot $\Delta x'$ produced by the zone plate equals:

$$\Delta x' = \frac{\Delta S}{M}. \tag{3.12}$$

giving a measure for the minimal slit size of the monochromator. The energy dispersion ΔE in the slit plane of the zone-plate monochromator is dependent on the square of the XUV photon energy E, the central line density d of the structure, the diffraction angle β, and the inverse of the length of the exit arm R_2' [28]:

$$\frac{\Delta E}{\Delta x'} = \frac{E^2 d \sin\beta}{hcR_2'} \quad , \tag{3.13}$$

Here, h and c denote the Planck constant and speed of light, respectively. With a given entrance angle α, the optimal line density d can be calculated according to an equation presented in [28]:

$$d = \frac{\lambda}{\sin\alpha}\left[\left(1+\cot^2\alpha+\left(\frac{R_2'}{\Delta x'}\frac{\Delta E}{E}\right)^2\right)^{\frac{1}{2}} - \cot\alpha\right] \quad . \tag{3.14}$$

In an experimental setup with a fixed geometry, i.e. fixed incident angle, distances R_1' and R_2' and groove distance d, a monochromator based on ORZPs is restricted to operate with a single harmonic of the driving laser. This restriction can be overcome if several off-center zone plates optimized for different high harmonics are manufactured in an array on a single substrate (see figure 5.3). Then, a change of the laser harmonic can be accomplished by translating the substrate along the array of zone plates [28] without any further alignments.

3.4. Supplementary techniques

Supplementary techniques have been developed to select individual laser harmonics out of a XUV spectrum. Among them are approaches employing metallic filters of suitable transmission and approaches where harmonic generation is realized in a noncollinear arrangement of several laser beams [53, 54].

Experiments where harmonic selection is conducted with metallic filters allow a high transmission of the desired spectral range through the filters. Furthermore, since no diffractive element is used, the pulse stretch is minimal. The spectral transmission of such a filter-based monochromator can be too broad, though, since it may be difficult to find materials exhibiting sufficiently steep absorption edges. Thus, an unwanted amount of intensity from neighboring harmonics may be transmitted. Furthermore, the limited choice of filter materials limits the possible choice of XUV wavelengths.

4. Experimental setup

The experimental setup for time resolved XUV photoelectron spectroscopy consists of a driving laser, a stage employing low-order nonlinear optics to generate the desired pump beam for time-resolved PES, the HHG beamline and the experimental vacuum chamber for the PES experiment. A scheme of the experimental setup is depicted in figure 4.1. It can be grouped into four sections, the generation stage, spectral separation, refocusing to the experiment, and the experimental chamber. The individual components are described in the following section.

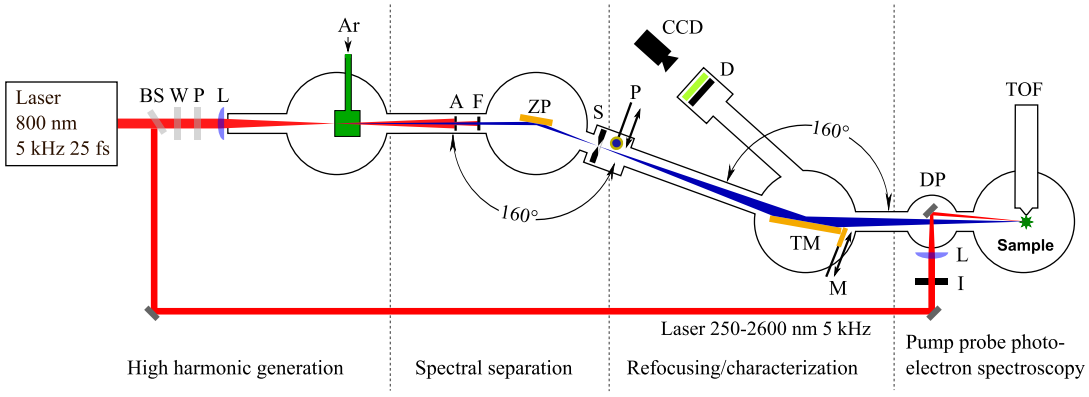

Figure 4.1.: Elements of the HHG beamline including the experimental chamber for time-resolved PES. Reprinted with permission from ref. [52].

The driving laser and the HHG beamline up to the refocusing section are located in a clean room, which is temperature and humidity controlled. Locating the experimental chamber for time-resolved PES outside of this room yields the advantage that the controlled atmosphere in the clean room is undisturbed while conducting experiments. This allocation of equipment results in a minimum distance between the refocusing mirror and the position of the liquid jet, though, as the experimental chamber for PES has some size itself.

4.1. Layout of the HHG Beamline

4.1.1. Femtosecond laser system

As pointed out in the introduction, Ti:sapphire lasers producing ultrashort IR light pulses are routinely used for high harmonic generation. The driving laser for the present high harmonic generation, as well as for the low harmonic generation

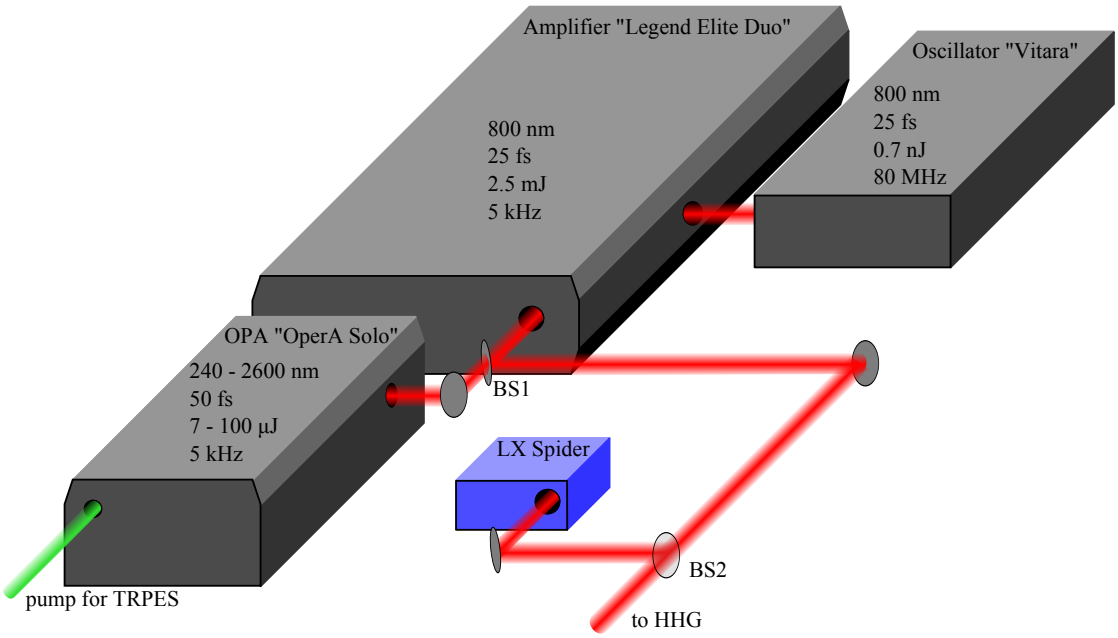

Figure 4.2.: Elements of the femtosecond laser system including oscillator, regenerative amplifier and optical parametric amplifier.

or the OPA, is a commercially available femtosecond laser system from Coherent. The layout of the laser system is schematically shown in figure 4.2. It consists of the oscillator model "Vitara", delivering light pulses of 25 fs duration with an average power of 550 mW at a repetition rate of 80 MHz. The spectrum of the light pulses after the oscillator is modified in the spectral shape filter "SSF" for efficient amplification in the regenerative amplifier "Legend Elite Duo". The amplifier is operating at a repetition rate of 5 kHz. It delivers an average optical power of 12.5 W with the pulse duration of 25 fs. The beam is expanded after the amplifier to a size of 12 mm ($1/e^2$ criterion) and split with a pulse energy ratio of 3/2. The large beam size reduces the influence of air fluctuations on the intensity of the high-power laser light. For the same reason the optics tables are covered and connected with tubes.

IR light pulses up to a pulse energy of 1.5 mJ are available from the reflection of the beam splitter (BS1) to drive the HHG process. In a first approach to regulate this pump energy and thus influence the HHG efficiency via phase matching, the laser intensity of this part was regulated with an iris aperture. This is a cheap and quick method to start with, but it comes with some drawbacks. The accuracy and reproducibility of the aperture mechanics are low. Furthermore, a progressively closed aperture introduces more and more interference fringes in the spatial profile of the beam. Although the mean power may be ideal for efficient high harmonic generation, the local pump intensities vary with the interference pattern. This leads to regions of too low intensity coexistent to regions of too high intensity for efficient conversion, eventually resulting in overall low output of XUV light. Additionally, the focal spot size changes in the generation region with changes of

aperture size. These variations are then transferred to the interaction region of the PES measurement via the XUV optics of the beamline.

A more advanced approach uses a combination of a half-wave plate and a thin-film polarizer. The rotation of the waveplate controls the ratio of s- and p-polarized light, and therefore, the fraction of pulse energy transmitted through the polarizer. This method leaves the spatial profile and focal spot size undisturbed, and settings are easily reproducible. Furthermore, the laser polarization is cleaned from any elliptical contribution. Waveplate and polarizer are the models OA232 and OA541 supplied by FEMTOLasers, and specially designed to support the broad spectrum of ultrashort light pulses. The laser pulses are focused loosely into an argon filled cell by a 600 mm lens mounted on a translation stage. The laser light for generating high harmonic radiation is characterized by a device from APE (model LXSpider) employing the technique of spectral phase interferometry for direct electric-field reconstruction (SPIDER).

Pump light generation for pump-probe PES experiments

The laser light transmitted through the beam splitter (BS1) exhibits a power of 1 mJ. This part of the laser output is used to generate the pump light for the pump-probe PES experiment. Three alternatives are available to adapt this light to the specific pump photon energy required for a particular sample system. In the first option, the IR laser light is employed to excite the sample without further modification of the photon energy. This facility is chosen for the cross correlation (CC) experiment used to characterize the zone plate (see section 5.5). The second option allows to generate the second or third harmonic of the IR laser light through nonlinear optical processes in a home-built stage based on barium borate (BBO) crystals. This alternative is used in the time-resolved PES experiments on hemin dissolved in DMSO (see section 8.5). Finally, a commercially available OPA (Coherent, model "OperASolo") allows to choose the photon energy of the pump light in the large range between 5.16 and 0.48 eV.

4.1.2. High harmonic generation

Out of the different technical approaches described in section 3.1.3 for generating XUV light though the process of HHG from an intense IR laser, the method employing a gas filled cell is chosen. For generating high-order harmonics with photon energies up to several tens of eV in argon, the use of a cell represents an unpretentious system to start with. At the same time it opens the way to more sophisticated setups when either a higher photon flux or higher photon energies are desired. The confinement of the generation volume into a cell allows to use a larger range of gas pressures, while consuming smaller amounts of gas as compared to a free gas jet. At the same time, the alignment effort is smaller than compared to an approach employing a gas filled waveguide.

The stainless steel cell hosting the argon atmosphere for HHG is connected to an injection lance via a connection system using Swagelok's VCR metal gaskets.

A scheme of this system is depicted in figure 4.3. During operation, the lance is vertically inserted through a lock (L) into the generation chamber (C). The lock allows the exchange of the lance without breaking the vacuum. The system is sealed at the top of the lock with an o-ring pressed against the lance. Upon removing the lance, the vacuum chamber is closed by a gate valve (GV) between chamber and lock before the lock is opened to the air and the lance is taken out completely.

The cell has two openings allowing the laser to pass horizontally through it. The openings are initially sealed with an aluminum tape glued around it. The focused laser then drills its own entrance and exit apertures into the tape, ensuring minimal gas leakage. The bottom of the cell is designed to fit into a special receptacle placed at the bottom of the vacuum chamber. Thus, the cell is always placed in the same position when the lance is inserted into the vacuum. This construction prevents any need for further adjustments of the cell with respect to the laser focus once the laser beam is aligned.

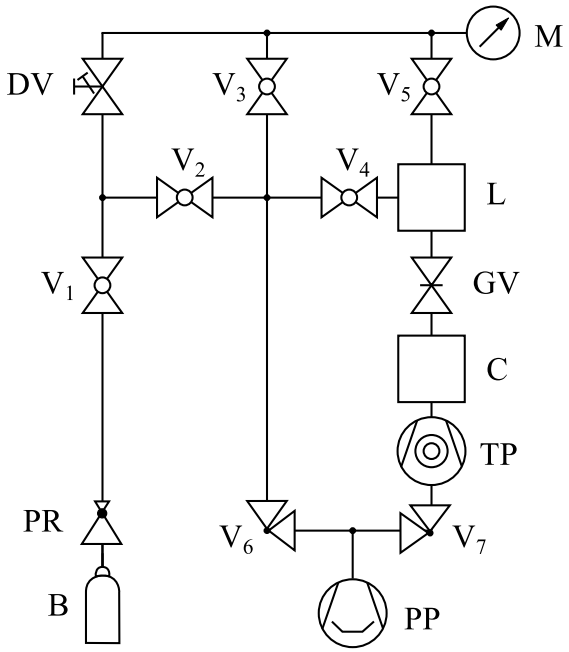

Figure 4.3.: Piping and instrumentation diagram of the gas supply for HHG in a gas filled cell. The gas bottle is labeled B, while valves are denoted V_{1-7}, the dosing valve is labeled DV and the gate valve GV. The gas cell is labeled C, the turbo pump TP and the prevacuum pump PP. The function of the individual parts is described in the text.

As a nonlinear medium argon 4.8 is supplied from a gas bottle (B) stored in a safe cabinet. The bottle is connected via a pressure regulator (PR) to the gas line. A dosing valve (DV) is used to regulate the pressure in the cell up to 40 mbar measured by the manometer (M) at the top of the injection lance. To establish a clean argon supply, every section of the supply tubes can be evacuated by the oil pump (PP) through the valves V_1 to V_6. The oil pump also generates

the prevacuum for the turbomolecular pump (TP) connected to the generation chamber.

During operation, the residual pressure in the generation chamber is in the order of 10^{-4} to 10^{-3} mbar. To retain low pressures in the subsequent vacuum chambers housing the monochromator and refocusing mirror, a differential pumping stage is connected between the generation chamber and the vacuum chamber for spectral selection. A removable aperture is installed between the differential pumping chamber and the monochromator. This aperture significantly reduces the heat impact of IR radiation onto an ultra-thin aluminum filter, which is installed to block the residual IR light. The filter transmits approximately 70 % of the XUV light, but blocks the IR light. In the course of the experiment, the aluminum foil has been moved from this place and has been installed behind the exit slit of the monochromator to extend the lifetime of the foil.

4.1.3. Spectral selection of high harmonics

From the group of high harmonics generated from the IR laser, a specific harmonic has to be chosen to conduct the spectroscopy experiment. For the spectral separation a novel type of monochromator employing ORZPs is used. The design and performance of this monochromator are presented in detail in chapter 5.

The present section addresses the design of the vacuum chamber and the custom-made manipulator for positioning the monochromator in the UHV environment. While the ORZPs offer some unique advantages, their full potential can only be exploited when they are precisely aligned with respect to the incident XUV laser beam. Therefore, the manipulator for positioning the monochromator has to control the motion of six axes (three translational and three rotational axes) with sufficient precision. In particular, the motors for the translational axes should provide a positioning precision better than 5 µm and the rotational axes should support a precision better than 1 µrad. Additionally, the three rotational axes should intersect each other in one point in the center of the monochromator surface. Since the laser beam is propagating in a plane located at a height of 165 mm above the optics table, the construction of the six-axes manipulator also has to be adapted to this low height. At the same time it has to be strong enough to move and support the weight of the monochromator. Furthermore, it has to be UHV compatible in the order of 10^{-9} mbar. The design satisfying the aforementioned constraints is shown in figure 4.4. Displayed is the version for the refocusing mirror. The manipulator consists of two sections. The lower part (light blue) controls the horizontal linear motions along the directions labeled as x- and y-axis, and, mounted on top of this part, is the translation stage controlling the vertical motion (dark gray) along the direction labeled as z-axis. The linear translation stages are equipped with piezo-driven motors from "Nanomotion". Their motion is induced by piezo actuators via the slip-stick-effect. A number of piezo actuators are pressed on a ceramic strip attached to the translation stage, thereby holding the stage in position. During motion, oscillations of the actuators push the stage in the desired direction. The number of piezo actuators per translation stage determines

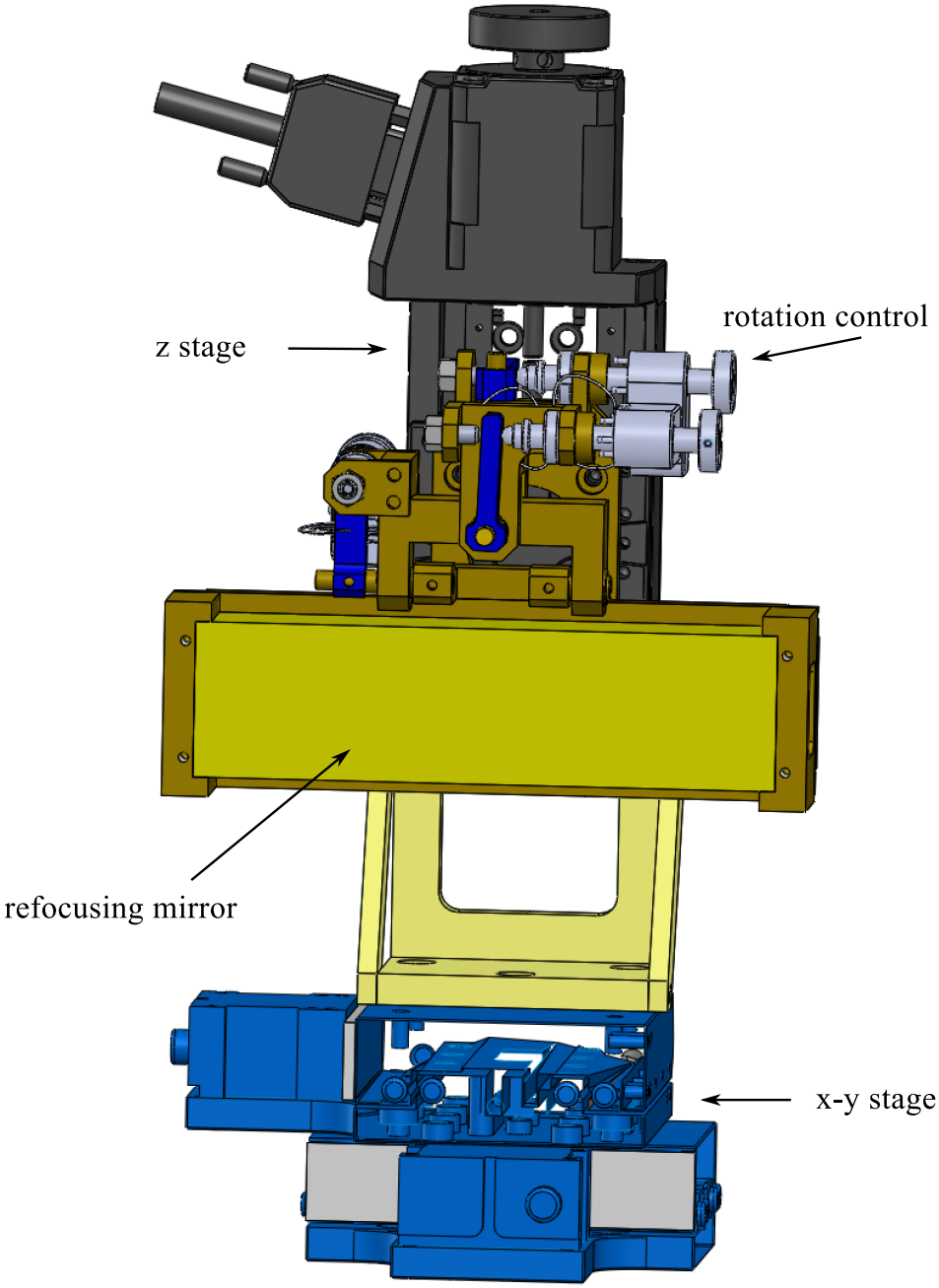

Figure 4.4.: Manipulator for XUV optics. The image shows the version for the refocusing mirror. The x-y stage controlling the horizontal movement is depicted in light blue while the stage for the vertical movement is depicted in dark grey. Attached is the module (dark yellow) controlling the rotational axes with the piezo actuators (light grey) pushing the levers (blue).

the holding force of the stage. The optical encoders (models Renishaw RGH25) incorporated in the stages allow to position them with a precision of 100 nm. Attached to this x-y-z-stage is the module controlling the rotations (dark yellow) and holding the monochromator substrate. Each rotational axis is driven by a piezo actuator (Newport model 8321-UHV) depicted in light gray. The actuator pushes a lever (blue) which translates the linear motion into a rotation. With a step size of approximately 30 nm and a lever length of 30 mm, the lever drive allows to achieve the desired precision of approximately 1 µrad. The rotational axes are not equipped with encoders due to limitations in space inside the vacuum chamber and limited capacity of the translation stages carrying weight. The manipulator is housed in a cylindrical vacuum chamber standing upright on the optics table. Figure 4.5 depicts a cutaway drawing of the vacuum chamber exposing the manipulator inside. The chamber body is equipped with flanges for the electrical feedthroughs used for wiring the motors and encoders. The entrance and exit flanges for the XUV radiation are welded at an angle of 20° with respect to each other, as this is the deflection angle of the monochromator (see section 5.1). Opposite of the entrance and exit flanges, two small flanges are welded to the chamber that allow to pass a laser beam used for alignment of the chamber and of the manipulator. With this construction, the vacuum chamber can be precisely positioned on the table. Once aligned, the chamber was fixed with clamps to the optics table.

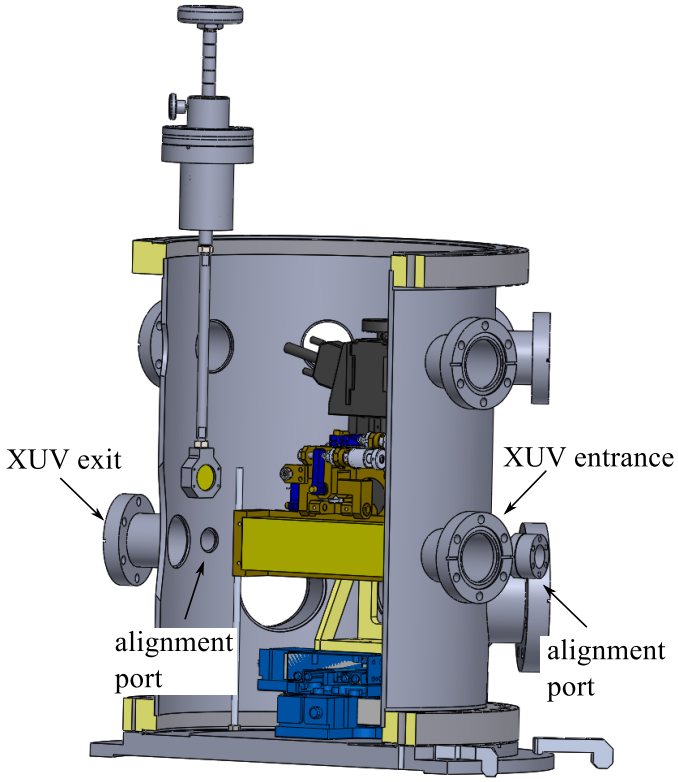

Figure 4.5.: Cutaway drawing of the monochromator chamber showing the inner part with the manipulator and the zone plate substrate.

The sidewall of the vacuum chamber can be dismounted from its bottom. This construction greatly simplifies access to the manipulator within the chamber. In this way, the manipulator can be assembled on the chamber bottom and it can be easily aligned under ambient conditions. After installation and orientation of the monochromator, the sidewall is re-attached to the chamber bottom. Special guide pins in the bottom plate ensure that the chamber wall position is reproducible.

Exit slit

While the dispersion of harmonics is induced by reflection zone plates, a slit placed in the focal plane of the monochromator is used for selecting a desired harmonic. The slit follows a design approach established at FU Berlin. The cylindrical vacuum chamber housing the slit mechanism is mounted on a manual x-y translation stage. This stage allows for precise positioning of the slit perpendicular and along the XUV beam path. Figure 4.6 displays a cutaway drawing of the slit chamber exposing

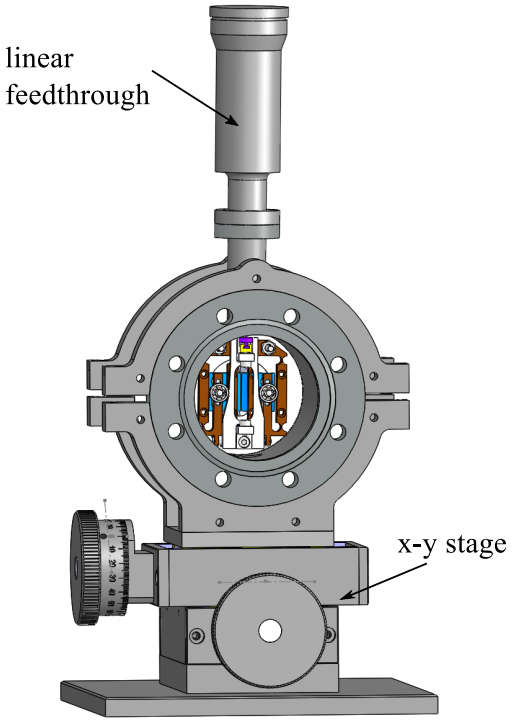

Figure 4.6.: Cutaway drawing of the slit and the surrounding vacuum chamber. The linear feedthrough pushes vertically downwards on the copper spring (orange) which translates the vertical motion to a horizontal motion to move the slit (blue).

the slit and some of the mechanics. To adjust the slit width, the rod of a linear feedthrough pushes against a copper spring that translates the vertical motion of the feedthrough into a synchronous horizontal motion of the two blades that form the slit.

Behind the slit chamber, a cubical vacuum chamber is mounted on the optics table. This cube allows to insert an aluminum foil into the beam path to block residual IR radiation. A photodiode can be inserted into the beam path directly behind the foil in order to measure the XUV photon flux. The photodiode is the XUV compatible model G1127-04 from Hamamatsu.

4.1.4. Refocusing of high harmonics

Downstream from the slit chamber, the vacuum chamber housing the refocusing mirror is placed on te optics table. The refocusing mirror redirects and focuses the XUV light onto the liquid jet located in the the vacuum chamber for the PES experiment. Details of the toroidal refocusing mirror are given in section 5.1.5 where the results of the ray tracing for the beamline are presented. The vacuum chamber of the refocusing mirror and the design of the six-axes manipulator supporting the mirror are very similar to that of the chamber housing the monochromator. Due to the weight of the mirror, the vertical z-axis is controlled by the UHV-compatible translation stage "LS-65" from "Physical Instruments".

The design of the vacuum chamber includes a translational feedthrough that allows to insert an additional plane gold-coated mirror into the beam path after the refocusing mirror. This construction enables to send the XUV light to an imaging detector to evaluate the intensity distribution in the XUV focus. The detector consists of a combination of a double-stack multi-channel plate (MCP) and a phosphor screen. The image on the phosphor screen is recorded with a charge coupled device (CCD) camera. Imaging detector and CCD camera can be moved on a translation stage along the path of the re-directed beam to measure the size of the focus created by the refocusing mirror.

4.2. Experimental setup for time-resolved photoelectron spectroscopy

The vacuum setup for time-resolved photoelectron spectroscopy has been developed in our laboratory for the investigation of liquid samples [55]. However, the PES experiments conducted during the characterization of the zone-plate monochromator employed argon gas as sample. Since the peculiarities of the setup arise from handling liquids in a vacuum environment, and are related to the liquid micro-jet technique which is introduced in section 7.3, the setup is described in more detail in a later section (see section 7.4). Here, a brief description is given only.

The vacuum chamber for the PES experiments is connected to the beamline for high harmonic generation so that the XUV beam passes horizontally in front the photoelectron time-of-flight (TOF) spectrometer opening. During the work presented in this thesis, the setup for XUV photoelectron spectroscopy was equipped with two different TOF electron spectrometer. In a first approach, a homebuilt TOF spectrometer with a single magnetic lens following the design of Kruit and Read [56] was used. Later, it was exchanged with a commercially available TOF

spectrometer from SPECS (THEMIS 600) which employs a set of electrostatic lenses and has been adapted to suit to the liquid-jet setup. The versatility that comes with the use of different electrostatic lens modes in the latter spectrometer is found to be advantageous over the larger collection of electrons by the magnetic bottle TOF spectrometer. Both devices are described in detail below. Argon gas is introduced into the chamber via a dosing valve. The pump beam for time-resolved studies is introduced through a glass window on the side of the vacuum chamber. A small mirror redirects the pump beam so that it intersects the XUV beam at a small angle in front of the electron spectrometer.

4.2.1. Magnetic bottle time-of-flight electron spectrometer

A part of the results presented in this chapter has been published in the following paper:

"Time-of-flight electron spectrometer for a broad range of kinetic energies"

Alexander Kothe, Jan Metje, Martin Wilke, Alexandre Moguilevski, Nicholas Engel, Ruba Al-Obaidi, Clemens Richter, Ronny Golnak, Igor Yu. Kiyan, and Emad F. Aziz, Rev. Sci. Inst., Vol. 84, 023106 (2013), DOI: 10.1063/1.4791792

The distinctive feature of this type of spectrometer is an increased collection of electrons compared to a conventional drift-tube TOF spectrometer. In the latter case, the acceptance angle, which is the solid angle of the electron cloud that reaches the detector, is solely determined by the geometry of the spectrometer. Namely it is defined by the length of the flight tube and the detector area. In comparison to this simple design, the implementation of an inhomogeneous magnetic field in the magnetic-lens spectrometer enables to increase the detection angle up to 4π steradians. This is achieved by a magnetic field that has a large field strength at

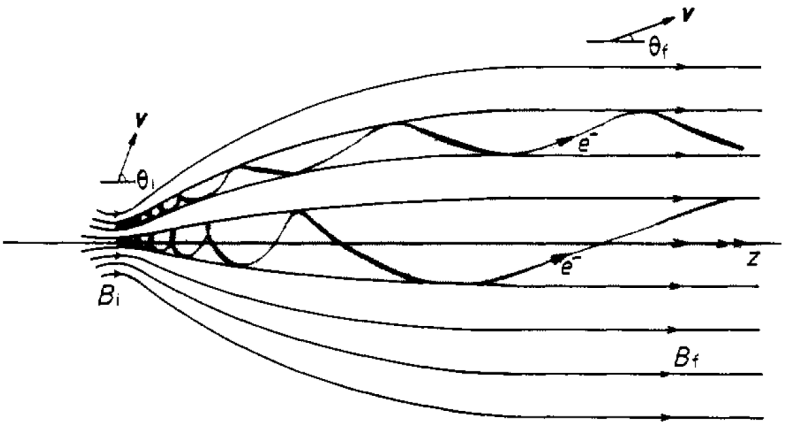

Figure 4.7.: Field lines of the bottle-shaped magnetic field, reprinted with permission from ref. [56]. The high-field region is the point of photoionization, whereas the electrons are detected at the end of the low-field region.

the point of photoionization, but whose strength then gradually decreases in the direction towards the detector, before it eventually turns into a weak homogeneous field parallel to the axis of the drift tube (see figure 4.7). Due to the shape of the magnetic field, the spectrometer is named "magnetic bottle" type.

The photoelectrons emitted from the sample experience a Lorentz force in the magnetic field, which depends on the local magnetic field strength and on the component of their velocity vector perpendicular to the local direction of the magnetic field. The Lorentz force causes the electrons to circle around the local direction of the magnetic field. Since the electrons also have a velocity component parallel to the local magnetic field, the resulting movement is in a spiral motion around the direction of the magnetic field. Simultaneously, the perpendicular component of the velocity will be decreased in favor of an increase of the parallel component, since the kinetic energy of the electrons is conserved.

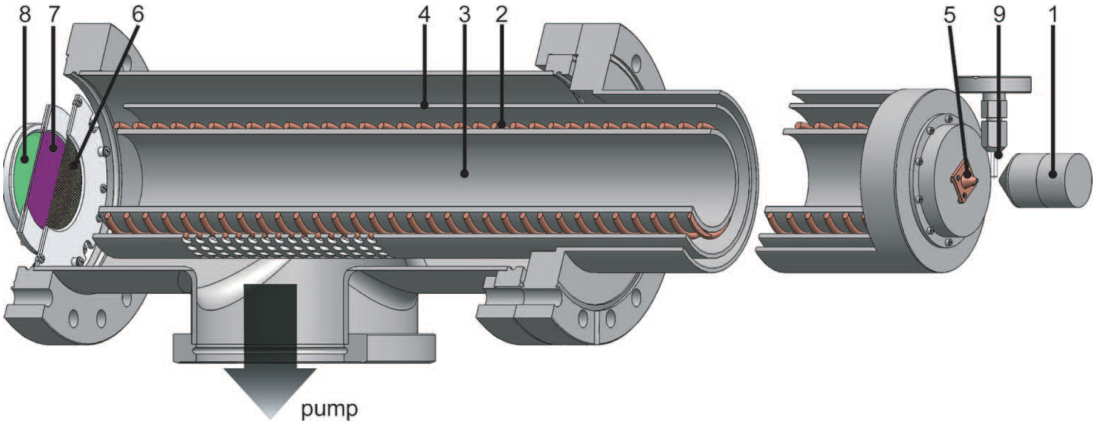

Figure 4.8.: Cutaway drawing of the magnetic bottle TOF spectrometer reprinted with permission from ref. [57]. Displayed are only the entrance (right) of the spectrometer and the rear part with the detector (left). The permanent magnet (1) creates the inhomogeneous magnetic field, which gradually turns into a homogeneous field determined by the solenoid (2) in the drift tube (3). The mu-metal shield (4) screens the flight region from outer magnetic fields. A stack of meshes (6), a double-stack MCP (7) and phosphor screen (8) compose the detector. The skimmer (5) reducing the spectrometer entrance and the nozzle (9) introducing the micro-jet are also shown.

The requirements imposed on the spectrometer due to the presence of the liquid sample and the use of a magnetic lens result in the layout depicted in figure 4.8 taken from Kothe *et.al.* [57]. The spectrometer consists of two sections, each carrying a turbomolecular pump. For simplicity, only the entrance of the spectrometer and the rear section housing the detector are displayed. The permanent magnet (1) creates the inhomogeneous magnetic field, which is eventually converted into a homogeneous field determined by the solenoid (2) in the drift tube (3). The permanent magnet is composed of a conical soft iron tip, a stack of cylindrical SM_2Co_{17} magnets and

a cylindrical soft iron end. The number of magnets determines the field strength. In the applied configuration two magnets have been used, each of them creating a magnetic field strength of 384 mT at the flat surface [58]. The solenoid is created from a Kapton-isolated copper wire. Its 500 turns per meter are laid on the drift tube with a distance between each other so that the inner part of the spectrometer can be evacuated through the perforated drift tube (holes are not shown in figure 4.8). With a current of 2 A, which was routinely used during the experiment, the coil generates a magnetic field of 1.26 mT. The mu-metal shield (4) screens the flight region from outer magnetic fields. In contrast to the drift tube, it is perforated only in front of the two turbomolecular pumps to allow for pumping the drift tube but to ensure high magnetic screening at the same time. The detector at the rear end of the drift tube consists of a stack of copper meshes (6), a double stack MCP (7) and a phosphor screen (8). In a first approach, only one mesh was mounted in front of the MCP. In this configuration, the mesh was grounded while the MCP front was kept at a bias potential of 300 V. This setting allows to accelerate the the photoelectrons to kinetic energies that meet the optimum MCP efficiency, and, at the same time, ensures a field-free flight region. A potential of 1.5 kV was applied across the double stack MCP for amplification of the photoelectron events. The cloud of electrons exiting the rear of the MCP is pulled onto the phosphor screen (8) by applying a potential of 2.4 kV between the back of the MCP and the phosphor screen. The screen fulfills two functions. On the one hand, it acts as a collecting anode for the photoelectrons where the current draining from the screen is used as the measurement signal. On the other hand, the electrons hitting the phosphor layer lead to a glowing of the screen. The resulting light emitted from the screen is captured through a viewport by a CCD camera facilitating the alignment of the XUV beam in front of the spectrometer. The results of the spectrometer calibration, which are published in ref. [57], and discussed below, were acquired with this configuration.

In a second approach, the front of the detector was upgraded with two additional copper meshes. This configuration allowed to apply a reverse voltage between the first and the second mesh, thus acting as a high-pass filter. The electrons that have passed the filter are then accelerated to their original energy between the second and third grid, before they are accelerated by a potential of 300 V onto the front of the MCP.

A gold-coated conical skimmer (5) reduces the entrance opening of the spectrometer and guarantees low pressure within the drift tube. A ball valve is located just behind the skimmer, so that the spectrometer can be separated from the vacuum chamber, in case the latter has to be vented. The interaction region (9) where the XUV light intersects the liquid jet and creating the photoelectrons is represented by a glass nozzle.

The data acquisition is conducted in the counting mode of photoelectron events. Here, each single electron event on the front of the MCP is amplified to a small electrical pulse draining from the phosphor screen. This pulse is decoupled from the bias high voltage of the screen by a high-pass filter. To prevent damage inflicted

by fast high voltage sparks on electronics downstream of the decoupling box, a spark protection module is used at the circuit exit. The measurement signal is then amplified by a two stage amplifier and processed by a fast digitizer computer card from Roentdek GmbH (model "bNdigo5").

Characterization of the magnetic bottle TOF

The magnetic bottle TOF spectrometer was characterized at the BESSY II beamline U41PGM to obtain the parameters for the conversion of flight time to electron kinetic energy, as well as to determine its energy resolution and collection efficiency. The test procedure used soft X-ray radiation to generate photoelectrons from argon similar to the routine described in ref [59]. The spectrometer was operated in the single grid configuration described in section 4.2.1 employing only one grounded grid in front of the MCP.

The spin orbit splitting of the residual Ar^+-ion produces a splitting of the 2p ionization channel into a doublet formed by the $^2P_{3/2}$ and $^2P_{1/2}$ contributions. Additionally, the photoelectron signal incorporates a contribution from Auger LMM decays of the argon 2p hole [60]. The part of the spectrum consisting of the photoelectron signal originating from the argon 2p doublet with a binding energy of 250.6 eV and 248.4 eV [61] is used for calibrating the spectrometer. This a suitable choice to produce low-energy electrons with the available range of photon energies of the beamline U41 starting from 180 eV. The equation underlying the energy conversion has the following form:

$$E_{(kin)} = \frac{m_e}{2} \frac{L^2}{(t - t_0)^2} \tag{4.1}$$

The kinetic energy E_{kin} is calculated from the ionization potential I_p and the photon energy provided by the beamline $E_{h\nu}$. The spectrometer length is represented by the variable L. The time offset t_0 is dependent on the readout electronics and the cable length. The fit of equation 4.1 to the data yields a length of the spectrometer of L = 102 cm.

The energy resolution of the TOF spectrometer has been evaluated from the calibration series for the configuration with the magnetic lens and for the lens-free conventional configuration. Results for the magnetic bottle configuration (filled red circles) and the field-free device (open black circles) for kinetic energies between 5 and 750 eV are presented in figure 4.9. The energy resolution of the spectrometer operated in the two configurations shows a different behavior, especially in the range of low kinetic energies. Therefore, the data are represented in a graph with a double logarithmic scale. The resolution is generally better for the lens-free spectrometer, which is due to the more complicated path of the photoelectrons performing the spiral motion in the magnetic lens. At medium kinetic energies around 50 eV, the relative resolution $\Delta E/E$ of the magnetic bottle TOF spectrometer improves. Here, the velocity component perpendicular to the magnetic field lines is large, resulting in a larger spiral radius. Since the fast photoelectrons exit the lens area sooner, the collection of electrons is reduced, which improves the resolution. At high kinetic

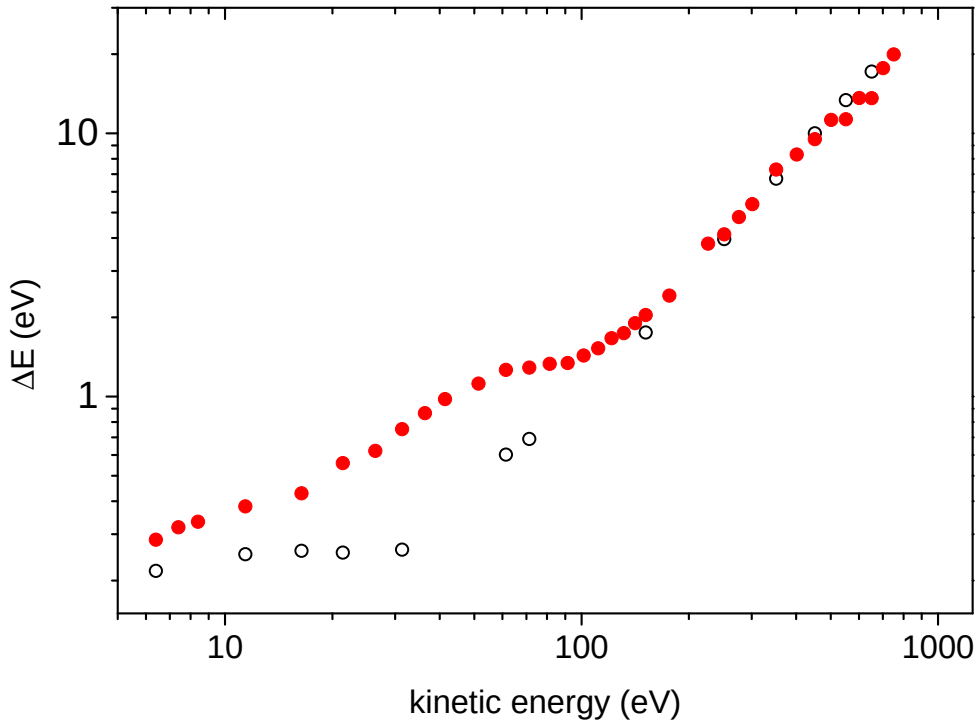

Figure 4.9.: Energy resolution of the magnetic bottle TOF spectrometer (filled red circles) reprinted with permission from ref. [57]. The corresponding resolution of a field free spectrometer is represented by open circles.

energies above 200 eV, the resolution of the two devices approach the same value. Here, the limiting factor for the resolution is the finite response time of the readout electronics.

Further evaluation of the Auger LMM signal allows the determination of the collection efficiency of the magnetic bottle TOF spectrometer. At low kinetic energies up to 50 eV, the collection efficiency is increased by more than two orders of magnitude compared to a conventional TOF spectrometer [57]. In this range, it decreases only slowly with increased electron kinetic energy. At higher kinetic energies, the collection efficiency decreases stronger. The maximal detection angle of 25° in the case of low kinetic energies is much larger than that of a conventional TOF, but still lower than the value of $\pi/2$ reported in refs [56, 62]. This is caused by the skimmer at the spectrometer entrance, which is installed to reduce the amount of evaporating sample transmitted to the spectrometer in an experiment with a liquid jet, but also blocks a part of the photoelectron trajectories.

4.2.2. Electrostatic lens spectrometer SPECS THEMIS 600

During the work for this thesis, the homebuilt magnetic bottle TOF spectrometer was exchanged against a commercially available TOF spectrometer with a system

of electrostatic lenses incorporated in the drift tube. The spectrometer is the model THEMIS 600 supplied by SPECS and was adapted to suit the liquid jet setup. This includes the installation of a skimmer which reduces the spectrometer opening and facilitates to maintain a good vacuum inside the device when operating with liquid samples. Furthermore, a valve is installed behind the skimmer to disconnect the spectrometer from the experimental chamber. Three turbomolecular pumps, each with a pumping speed of 300 L/s, pump the spectrometer during operation. The electrostatic lens system of the spectrometer allows a number of modes of operation. In the drift mode (DM), the lenses are switched off and the spectrometer corresponds to a conventional TOF spectrometer. In this mode, the device has its best energy resolution of approximately 25 meV at an electron kinetic energy of 20 eV. This is only limited by the geometry of the spectrometer. The second mode that is used during this work is the wide angle mode (WAM). In this mode, the electrostatic lenses are operated in a way that allows the largest collection angle of $\pm 13°$. Figure 4.10 displays the simulated electron trajectories in the WAM.

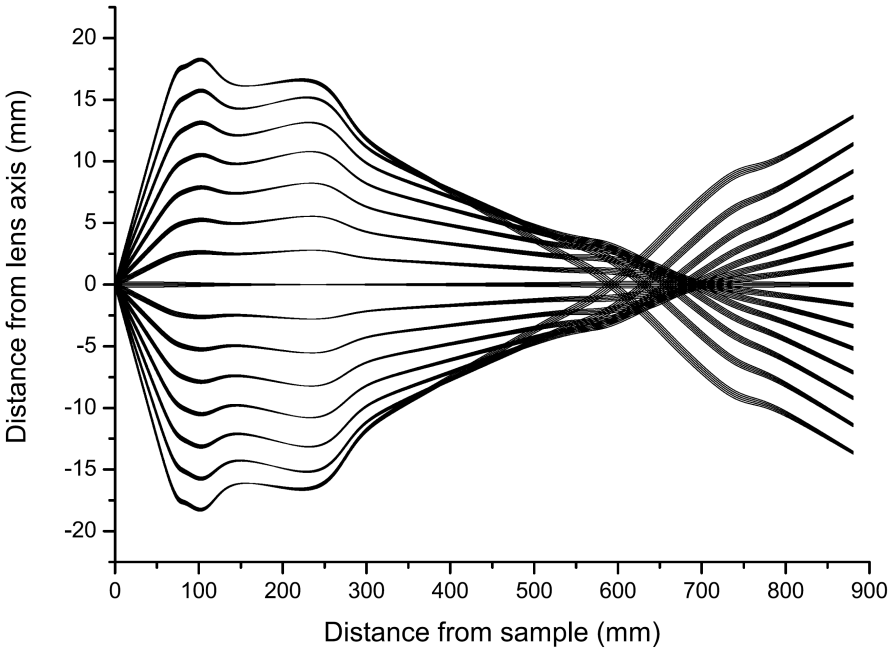

Figure 4.10.: Simulated electron trajectories of the THEMIS TOF spectrometer operated in the WAM, reprinted with permission from ref. [63]. The dimensions suit the larger model THEMIS 1000.

An iris aperture is placed at the position of the node of the electron trajectories. Closing this aperture allows to establish a differential pumping geometry without loosing many photoelectrons. A second aperture is located in front of the detector, which may be closed for differential pumping, but it decreases the strength of the photoelectron signal.

The delayline electron detector of the spectrometer consists of a double stack MCP and two wires that are laid in turns perpendicular to each other. When a cloud

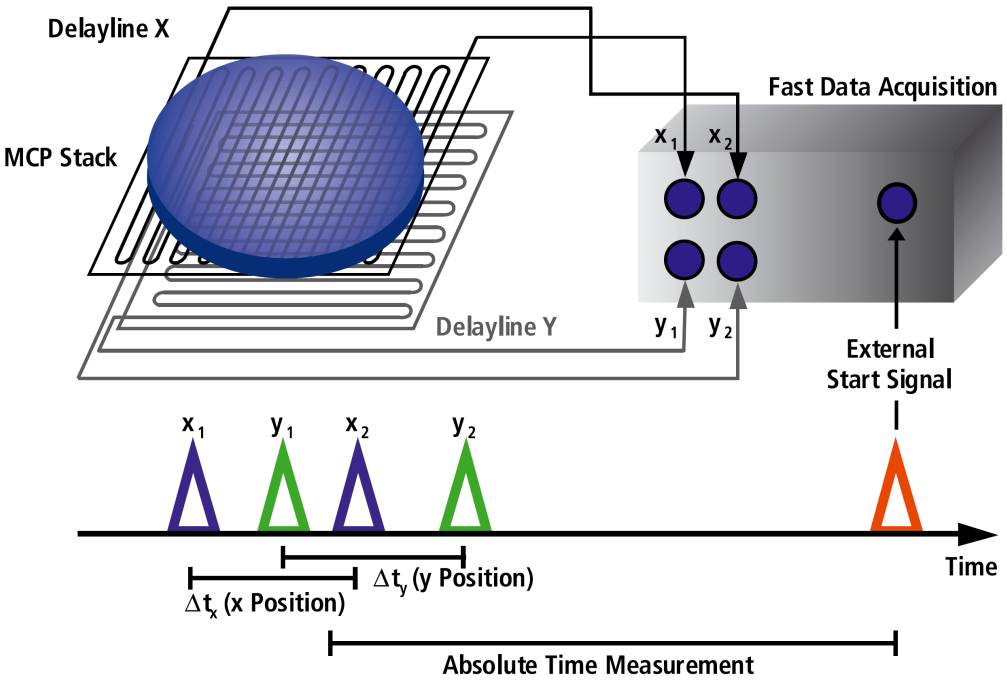

Figure 4.11.: Scheme of the delayline detector with the readout electronics, reprinted with permission from ref. [63]. The lower part of the drawing displays the pulse train of four measurement signals caused by an electron event on the grid.

of electrons exits the MCP and impinges on the wires, a current pulse travels to each ends of the wires creating a pulse train of four measurement signals. The pairwise analysis of the runtime of the signals allows the localization of the origin of electron events on the grid formed by the wires. Additional to the determination of the kinetic energy, the spatial evaluation of the detector signal allows the determination of the angular momentum of the electrons. Figure 4.11 displays a scheme of the delayline detector with the readout electronics taken from ref [63].

5. The off-axis reflective zone plate monochromator

A part of the results presented in this chapter has been published in the following article:

"Monochromatization of femtosecond XUV light pulses with the use of reflection zone plates"

Jan Metje, Mario Borgwardt, Alexandre Moguilevski, Alexander Kothe, Nicholas Engel, Martin Wilke, Ruba Al-Obaidi, Daniel Tolksdorf, Alexander Firsov, Maria Brzhezinskaya, Alexei Erko, Igor Yu. Kiyan, and Emad F. Aziz

Optics Express Vol. 22, pp 10747-10760 (2014), DOI:10.1364/OE.22.010747

5.1. Ray tracing: monochromator performance and beamline layout

The ray tracing program "RAYREFLEC", which was developed at Helmholtz-Zentrum Berlin [64], was used to design the layout of the beamline for harmonic generation and calculate the efficiency of the optical elements. Based on a set of parameters describing the source of the XUV light, the propagation of the XUV beam is simulated according to the equations describing the function of the optical elements and taking into account the material properties stored in the database of the program. From the ray tracing analysis, the intensity distributions on the surface of the optical elements and in two image planes located at the position of the slit and in the interaction region at the position of the PES experiment are presented.

5.1.1. Beamline efficiency

The efficiency of the beamline in the spectral range of XUV light depends on parameters such as surface roughness and coating material of the optical elements, as well as on the grazing incident angle of the XUV light. To find optimum conditions for the present setup, the reflectivity of a mirror for XUV light was simulated for different coating materials and geometrical parameters. The results are shown in figure 5.1. For each set of parameters, the solid lines represent reflectivity data for s-polarized light, while the dashed lines represent reflectivity data for p-polarized light. Metal coatings represent 40 nm thick layers deposited on a SiO_2 substrate. Panel (1) displays the influence of the coating roughness

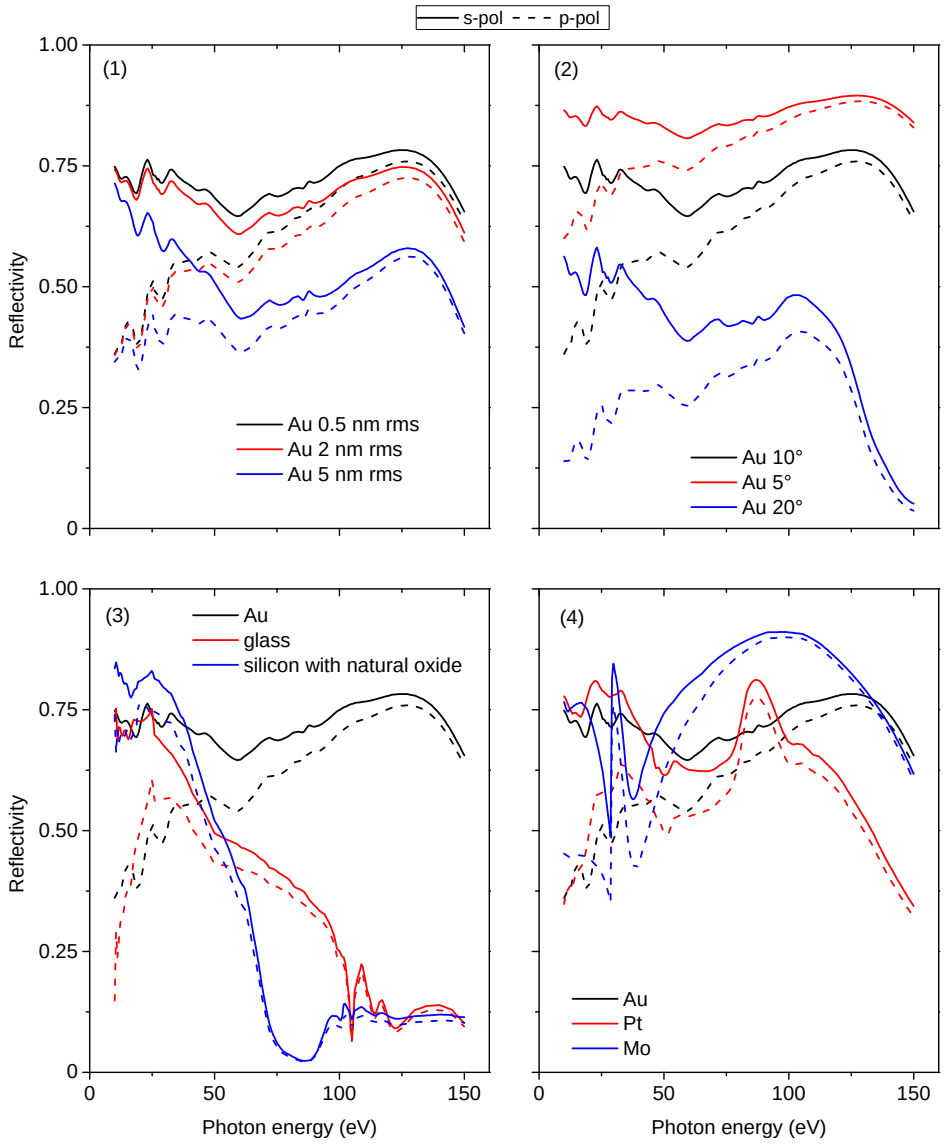

Figure 5.1.: Simulated reflectivity data for different XUV mirror configurations. The metal coatings have a thickness of 40 nm and are deposited on a SiO_2 substrate. The solid lines represent reflectivity data for s-polarized light, while the dashed lines represent reflectivity data for p-polarized light. Panel (1) illustrates the influence of coating roughness on the reflectivity of the mirror, exemplified on the case of a gold coating. Panel (2) displays the reflectivity of a gold layer for light incident under a grazing incident angle of 5, 10 and 20°. Panel (3) demonstrates the different reflectivities of a gold coating, a bare SiO_2 substrate and a silicon substrate with a natural oxide layer. Panel (4) compares the reflectivities of gold, platinum and molybdenum.

on the reflectivity in the case of a gold layer. The smaller the roughness of a reflecting surface is, the smaller is the loss of photons due to scattering. This is more pronounced for higher photon energies. Mirrors with a surface roughness much below 1 nm have high production costs, though. In the present spectral range from 10 to 150 eV, a root mean square (RMS) roughness of 0.5 nm has a sufficiently high reflectivity while still being affordable. Panel (2) compares the reflectivity of a gold layer for light incident under three different grazing incident angles, namely 5, 10 and 20°. Small incident angles lead to high reflectivities due to the smaller refractive index for XUV light in media compared to vacuum. Due to the geometrical constraints in the laboratory, a grazing incidence angle of ten degrees was chosen as a compromise. Panel (3) displays reflectivity data of a bare SiO_2 substrate and a silicon substrate with a natural oxide layer in comparison to a gold-coated mirror. While the silicon substrate with the natural oxide exhibits a higher reflectivity than gold in the range of low photo energies, its reflectivity significantly decreases at energies above 50 eV. Panel (4) compares the reflectivity of a gold-coated substrate to that of a platinum and molybdenum coating, which are common materials in x-ray optics. While molybdenum exhibits the highest reflectivity of these three materials around 100 eV, it has an absorption band around 40 eV leading to strong variations in reflectivity.

Based on the simulations, a gold coating and a grazing incident angle of 10° were chosen for the optical elements. This choice yields the best reflectivity for the photon energy range between 10 and 100 eV. The deflection angle of the reflected beam, which is twice the grazing incident angle, is therefore equal to 20°.

5.1.2. XUV light source

The rays for the ray tracing simulation emerge from a XUV light source which is assumed to have a circular shape with a Gaussian intensity distribution in the x-y-plane perpendicular to the propagation direction z. The divergence of the rays is assumed to have a Gaussian distribution as well. The parameters of the source are listed in table 5.1. Results from the ray tracing are presented for rays with a photon energy of 32.55 eV, which corresponds to the 21^{st} harmonic of the IR laser. The spectral bandwidth of the emitted light was set to a value of 150 meV (full width at half maximum (FWHM)), which is a typical value for comparable HHG sources [38].

width (FWHM)		depth	divergence (FWHM)	
x (μm)	y (μm)	z (μm)	x (mrad)	y (mrad)
100	100	100	1.2	1.2

Table 5.1.: Geometrical parameters used in the ray tracing algorithm describing the XUV light source.

5.1.3. The off-axis reflection zone plate

Since the XUV source at the start of the beamline has a size of 100 µm, and a thin liquid jet of 25 µm is the target for the PES experiment at the end of the beamline, the zone plate is designed to demagnify the beam size in the focal plane. The demagnification factor $M = R'_2/R'_1$ was chosen to be 35/100. The distance between the HHG source and the center of the ORZP was set to be 1000 mm, leading to a distance of 350 mm between the ORZP and the slit, according to the given demagnification factor. This results in a focus size of the monochromatized XUV light in the slit plane of 35 µm.

Having fixed the geometrical parameters such as the deflection angle and the demagnification factor, the entrance angle α, the exit angle β and the energy resolution ΔE are calculated from equation (3.13). The results are listed in table 5.2. The entrance angle acquires the value α =9.6°, the exit angle acquires the value

$E/\Delta E$	α (°)	β (°)	R'$_1$ (mm)	R'$_2$ (mm)
167	9.6	10.4	1000	350

Table 5.2.: The energy resolution and geometrical parameters of the zone plate monochromator, reprinted with permission from ref. [52].

of β =10.4°, and the energy resolution acquires a value of $E/\Delta E = 167$. Combining the source parameters listed in table 5.1 and the geometrical parameters listed in table 5.2, the size of the footprint of the XUV light on the ORZP structure is inferred from the ray tracing simulations. As it is displayed in figure 5.2, the choice of a small incident angle of 9.6° leads to a large footprint of more than 20 mm in the horizontal direction. Therefore, a substrate with a diameter of 50 mm was chosen for manufacturing the dispersive structure. In the vertical direction, the ORZP structure should have a size of 4 mm to sufficiently capture the incident XUV beam. Since a single ORZP is designed to select a specific harmonic, the approach presented by Brzhezinskaya *et.al* [28] suggests to manufacture several ORZP structures on a single substrate, to extend the spectral range of the monochromator. The large diameter of the substrate allows to manufacture several ORZP structures of 4 mm width on its surface. In the present layout, three ORZPs are combined on the substrate, namely for selecting the 17^{th}, 21^{st} or 25^{th} harmonic. The structures exhibit a size of 38 by 4 mm. A change between the harmonics implies a change between ORZP structures. This is accomplished through a linear translation of the substrate along its surface so that the corresponding structure is illuminated by the HHG beam. Figure 5.3 depicts an image of the gold-coated substrate accommodating the three dispersive structures.

The optimal line density for the ORZPs is calculated from equation (3.14), resulting in the values listed in table 5.3.

The dispersive structures of the ORZPs are manufactured by e-beam lithography and reactive ion etching on a silicon substrate. Due to the high quality of manufacturing processes in the semiconductor industry, the silicon substrate exhibits

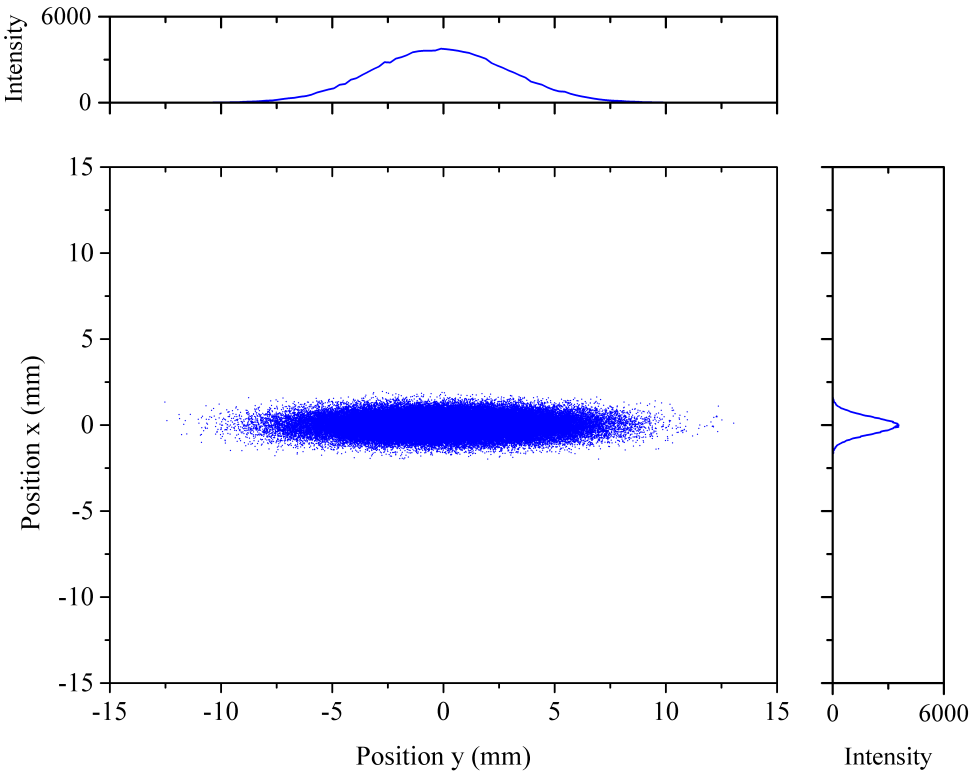

Figure 5.2.: Footprint of the XUV light on the monochromator substrate obtained from the ray tracing analysis.

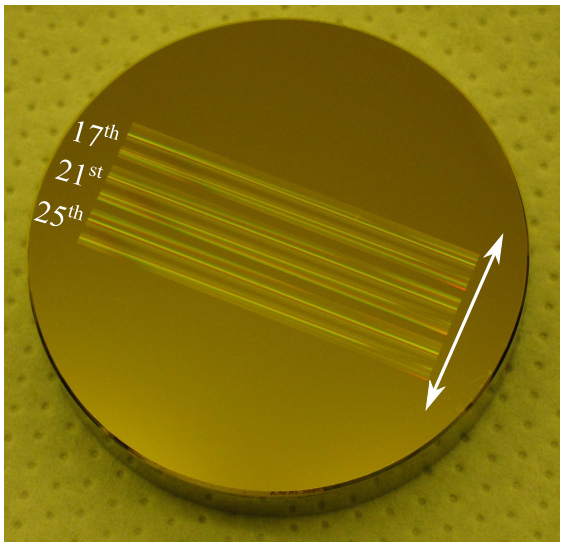

Figure 5.3.: Image of the gold-coated silicon substrate incorporating the three ORZPs for selecting the 17^{th}, 21^{st} and 25^{th} harmonic, respectively. The substrate has a diameter of 50 mm. The arrow indicates the direction of translation for selecting different harmonics.

Harmonic	E (eV)	d_1 (μm)	d (μm)	d_2 (μm)
17	26.35	161.5	18.2	9.1
21	32.55	130.7	14.7	7.4
25	38.75	109.8	12.4	6.2

Table 5.3.: Parameters of individual ZPs. d, d_1, and d_2 are the meridional structure periods in the geometrical center, at the low-density edge, and at the high-density edge of ZP's sections, respectively. Reprinted with permission from ref. [52].

a very high flatness and a very small surface roughness. After etching the zone plate structure, the substrate is coated with gold for enhanced XUV reflectivity (see figure 5.1). The structure exhibits a diffraction efficiency of 28.3 % for the design energy.

5.1.4. Intensity distribution of the XUV light in the slit plane

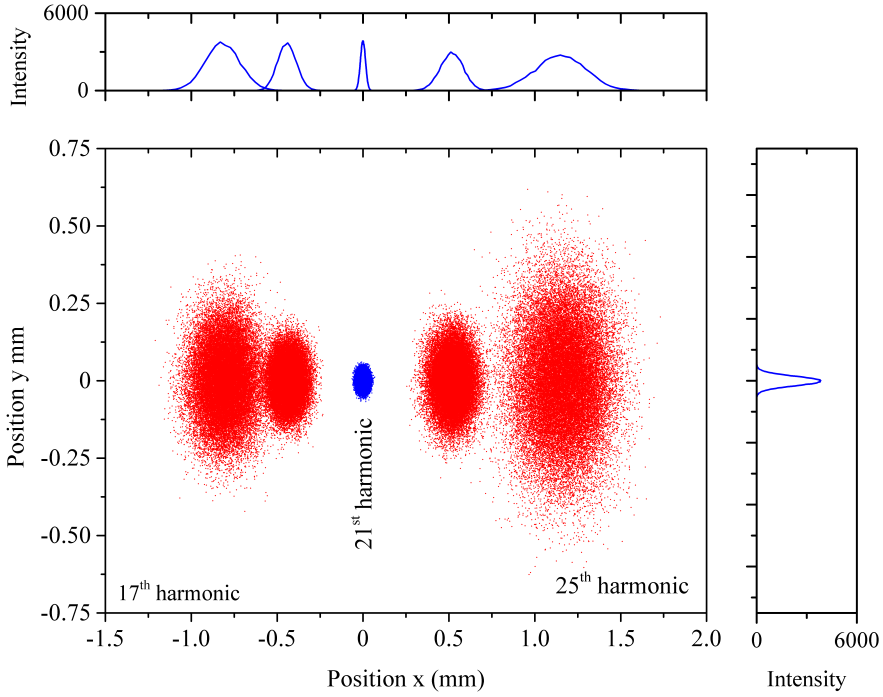

Figure 5.4.: Simulated intensity distribution of the XUV light in the focal plane behind the ORZP. The small focus of the design energy is depicted in blue color. The neighboring harmonics are displayed in red.

The simulated intensity distribution of the XUV light in the first diffraction order at the focal distance of the design energy is displayed in figure 5.4 for the case of the 21^{st} harmonic. It is apparent from the figure that the light of the design energy is focused to a small spot depicted by blue color in the middle of the image. The neighboring harmonics of two uneven higher and two uneven lower orders are also displayed. Since they experience longer and shorter focal lengths, respectively, they appear unfocused but well separated from the focal spot of the 21^{st} harmonic. Note that the oval appearance of the beam spots in the figure is induced by the use of different scales on the axes. The size and the Gaussian intensity distribution of the focus created by the ORZP monochromator is apparent from figure 5.5, which displays the central spot from figure 5.4 in greater detail. A nearly circular spot with a size of 35 µm (FWHM), as it should be according to the chosen demagnification factor $M = 35/100$, is achieved.

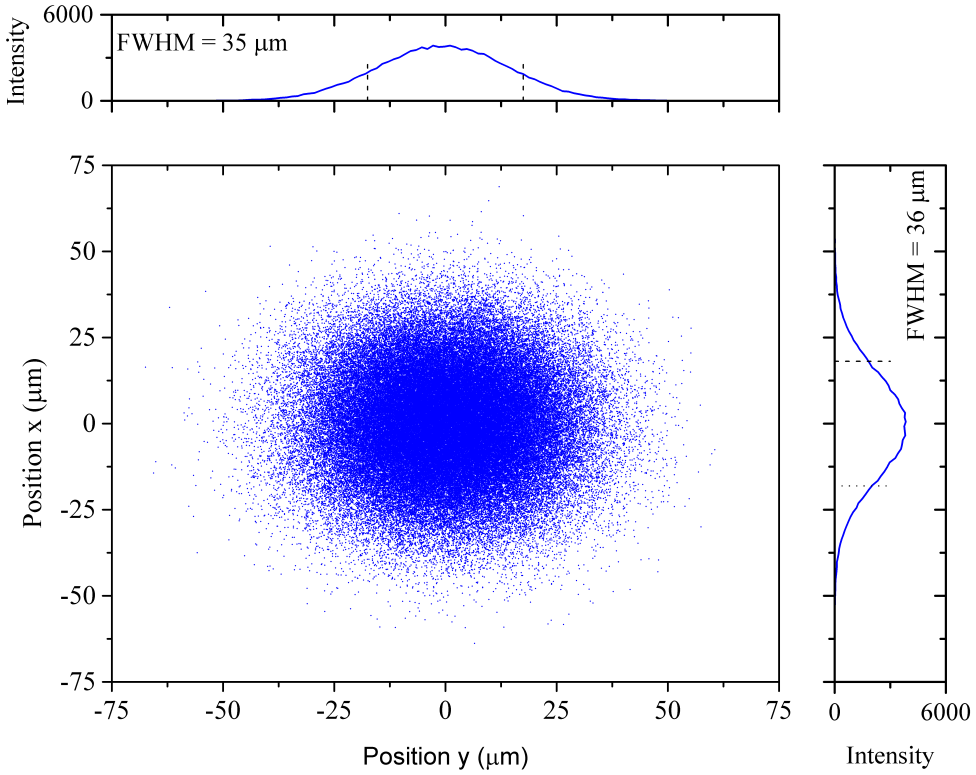

Figure 5.5.: Intensity distribution of a single harmonic of the design energy of the ORZP in the focal spot behind the monochromator.

5.1.5. Refocusing mirror

A toroidal mirror was chosen as optical element for refocusing the XUV light onto the liquid jet. This is a curved mirror whose surface has two different orthogonal

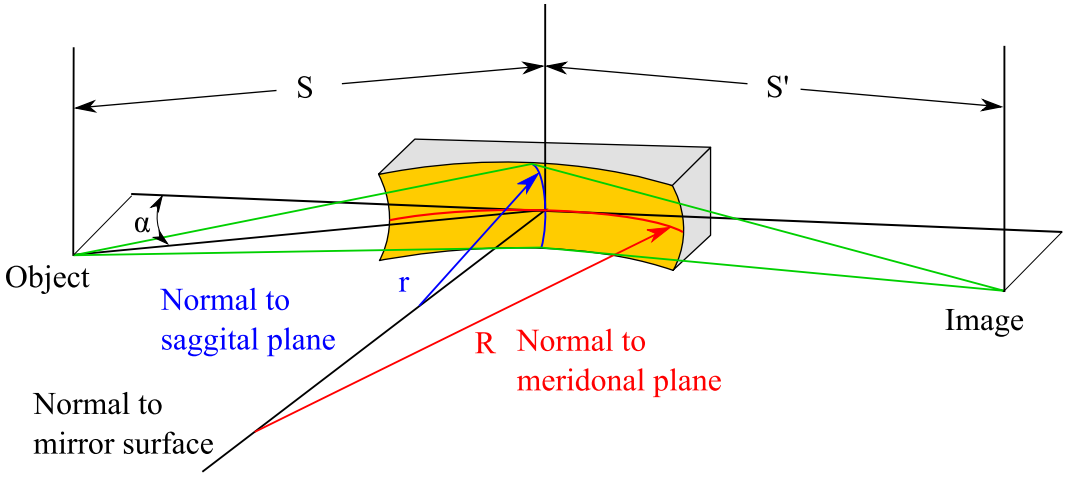

Figure 5.6.: Imaging scheme of a reflecting toroidal surface. The geometrical path of the light from object to image is depicted in green, while the saggital radius r and the meridional radius R of the toroidal surface are drawn in red and blue, respectively.

radii in the saggital and meridional direction, respectively, as it is depicted in figure 5.6. The advantage of the toroidal shape is a reduction of astigmatism when imaging a point source. The particular layout of the mirror, especially the values of the radii, is defined by the geometrical factors in the laboratory. The grazing angle α was chosen to be 10°. Thus, the refocused XUV beam propagates in a direction parallel to the IR pump beam. The minimum distance from the refocusing mirror to the position of the liquid jet is 1173 mm defined by the dimensions of the setup for the PES experiment. To further minimize aberrations, the focal length on the object side and on the image side of the mirror are chosen to be equal. Taking these considerations into account, the surface radii of the mirror can be calculated from the toroidal mirror equations:

$$\begin{aligned} \frac{1}{S} + \frac{1}{S'} &= \frac{2}{R\,cos(\alpha)} \\ \frac{1}{S} + \frac{1}{S'} &= \frac{2\,cos(\alpha)}{r} \end{aligned} \tag{5.1}$$

Here, S denotes the object distance, i.e. the distance between the slit plane and the mirror, while S' denotes the image distance, which is the distance between the mirror and the interaction region of the PES experiment. The results for the ideal surface are summarized in table 5.4 together with the actual radii measured after machining the mirror. For this geometry, equation 5.1 yields a saggital radius of r=203.69 mm and a meridional radius of R=6755.04 mm. The large distance of 1173 mm between the slit and the refocusing mirror and the grazing incident angle of 10° result in a large footprint of the divergent XUV beam on the mirror surface. The size of the footprint acquired from the ray tracing simulation is displayed in

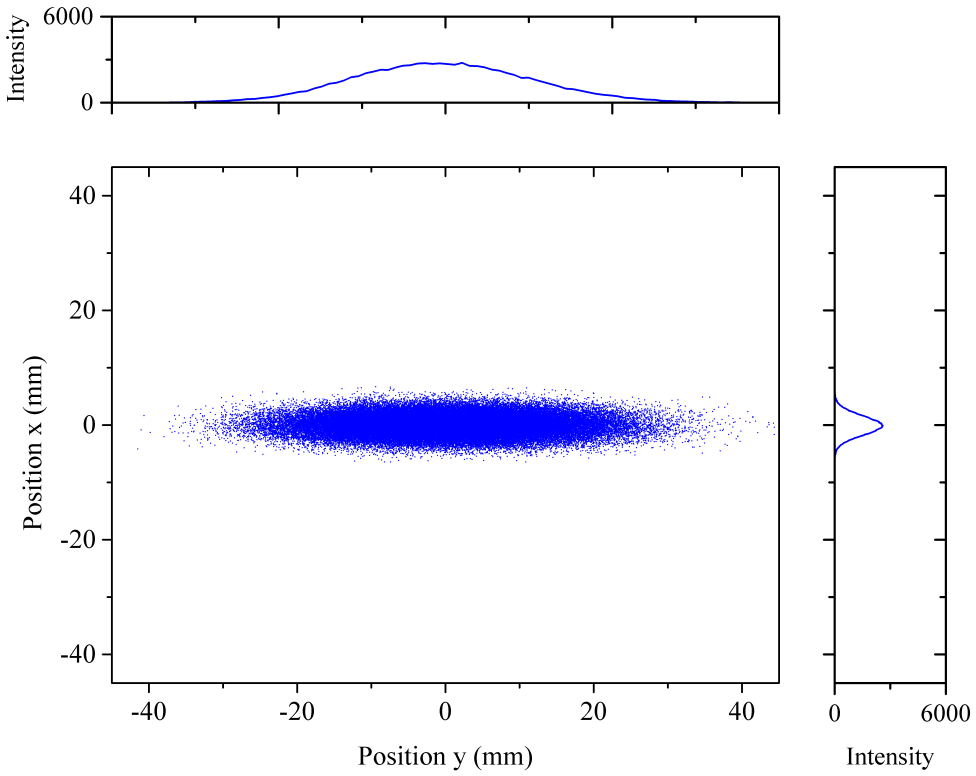

Figure 5.7.: Footprint of the monochromatized XUV light on the surface of the refocusing mirror obtained from the ray tracing simulation.

figure 5.7. The XUV beam is spatially stretched to a size of 80 by 10 mm on the mirror surface. With the reflectivity of 70 % of the gold coating as it is described in section 5.1.1, the combination of ORZP and refocusing mirror achieves an efficiency of 20 %.

Apart from the curvature, the roughness of the mirror surface is an important parameter for a high quality image.

α (°)	S (mm)	S' (mm)	r (mm)		R (mm)	
			designed	measured	designed	measured
10	1173	1173	203.69	203.85	6755.04	6759.55

Table 5.4.: Parameters of the refocusing mirror. The object distance and image distance are denoted S and S' respectively. The saggital radius and meridional radius are denoted by r and R, respectively.

Figure 5.8 shows a contourplot of the residual height error of the manufactured mirror surface. A value of ≈ 0.5 nm for the RMS roughness proves that the manufacturing quality of the mirror surface is sufficiently high.

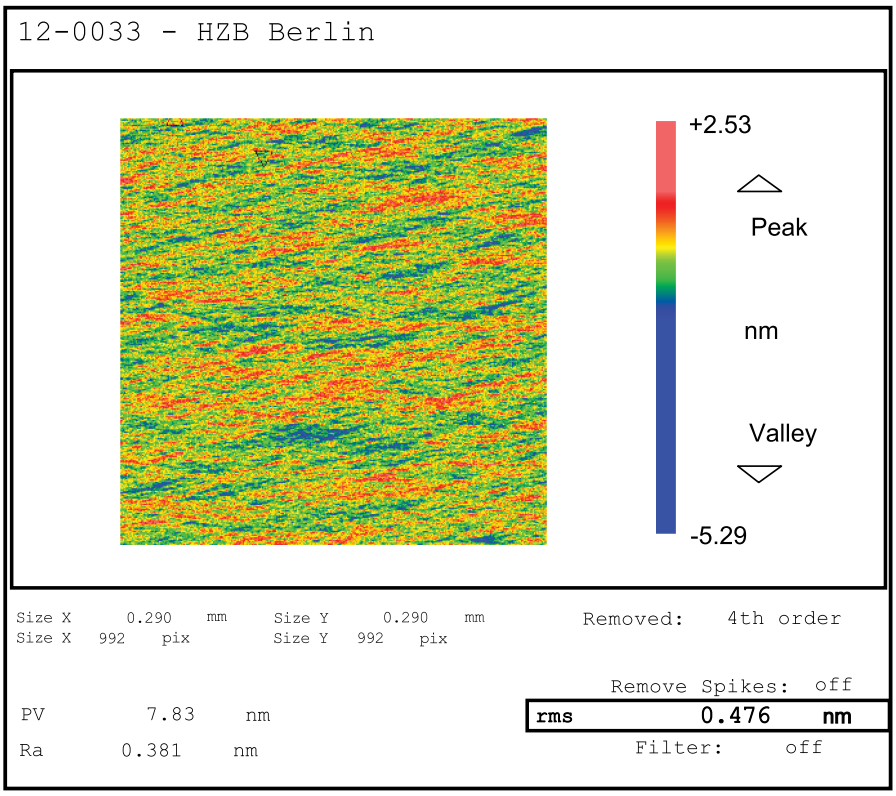

Figure 5.8.: Contourplot of the residual height error of the toroidal mirror. Data taken from the metrology measurements performed by Carl Zeiss Laser Optics GmbH.

5.1.6. Intensity distribution of the XUV light in the interaction region

The simulated intensity distribution of the monochromatized and refocused XUV light in the interaction region for the PES measurement is displayed in figure 5.9. The ray tracing simulation yields a focal spot of 35 µm (FWHM) in front of the

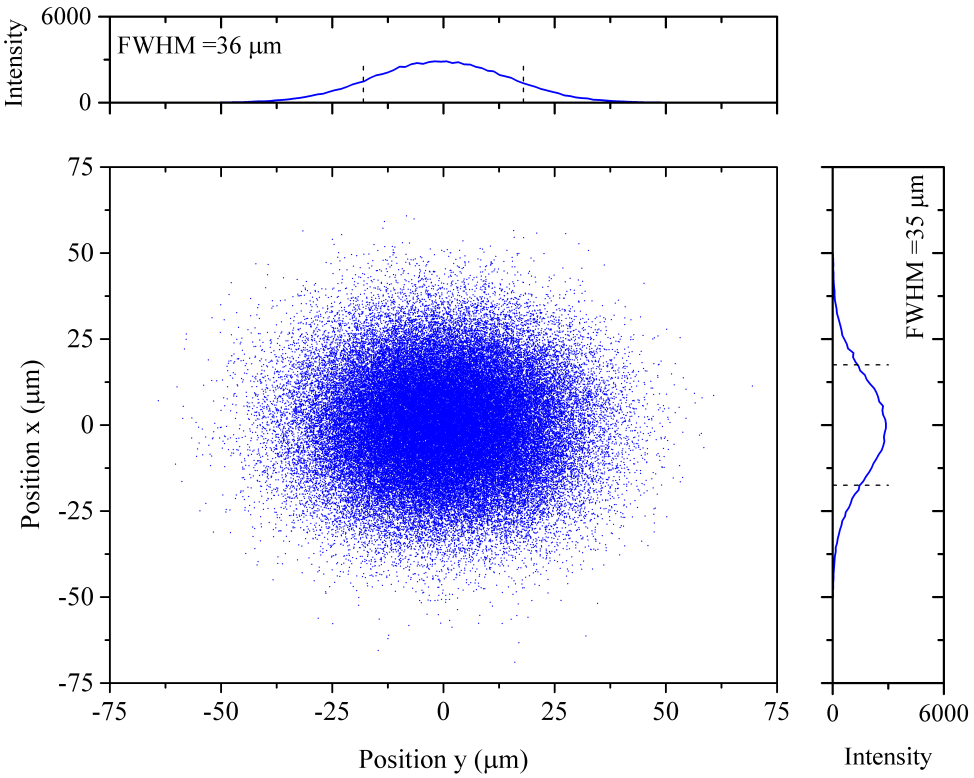

Figure 5.9.: Intensity distribution of the XUV light in the interaction region of the PES experiment obtained from the ray tracing analysis.

TOF spectrometer. This is the same value as for the zone-plate monochromator and only slightly larger than the liquid jet. The spot exhibits a Gaussian intensity distribution without aberrations.

5.2. Size of the monochromatized XUV focus

In a preliminary experiment, the position sensitive detector for XUV diagnostics was placed at a short distance behind the slit plane of the monochromator, without the slit installed in the beam path. Figure 5.10 shows an image, recorded by the CCD camera, of the intensity distribution on the phosphor screen of the position sensitive detector produced by the XUV radiation. The image consists of several

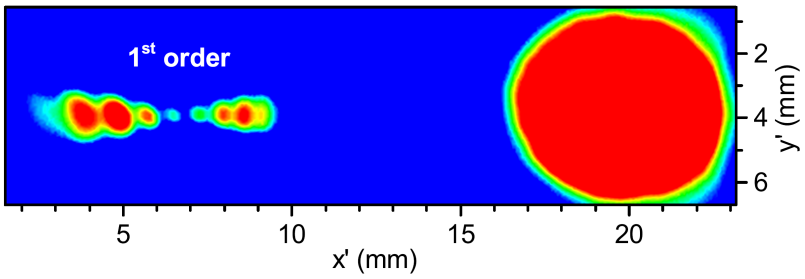

Figure 5.10.: Colourplot of the intensity distribution close to the focal plane of the zone plate. The image of the phosphor screen of the position sensitive detector illuminated by the XUV light was taken with the CCD camera. Reprinted with permission from ref. [52].

bright spots of which the largest spot on the right hand side represents the zero-order reflection from the zone plate. The other spots appear in a group showing a hyperbolic envelope. This group originates from the first-order diffractions of the HHG light. The hyperbolic envelope arises from the fact that some harmonics are focused at different points between the monochromator and the detector, while other harmonics have their focal points behind the detector. The central spot in the first order appears as the smallest and originates from the specific harmonic for which the zone plate was designed. As it is predicted from the ray tracing simulations, it is clearly separated from the others. Figure 5.10 is a demonstrative result, showing the separating and focusing capabilities of the off-center reflection zone plate.

After installation of the slit behind the monochromator and completion of the high harmonic beamline including the refocusing section, the separation of high harmonics and the size of the focal spot were tested behind the refocusing mirror at a distance equal to that of the interaction region. For this purpose, the additional mirror M1 located after the refocusing mirror (see figure 4.1 on page 19) was

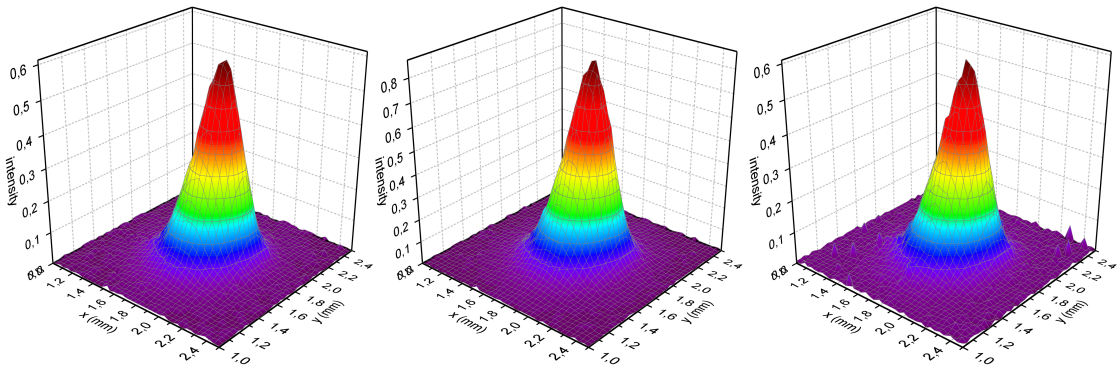

Figure 5.11.: Surface plots of the intensity distribution of the monochromatized 17^{th}, 21^{st} and 25^{th} harmonic in the focus produced by the toroidal mirror and recorded with the XUV detector.

inserted into the beam path to redirect the monochromatized and convergent XUV light to the position sensitive detector for XUV diagnostics. The detector was located at approximately the same distance to the refocusing mirror as the liquid jet would be in a spectroscopic experiment. Each zone plate was tested. The focii of the three zone plates imaged by the refocusing mirror on the XUV detector were captured with the CCD camera and transferred to intensity plots. Figure 5.11 shows the resulting surface plots of the intensity distribution of the XUV focii of the 17^{th}, 21^{st} and 25^{th} harmonic, respectively.

The Rayleigh length and the size of the XUV focus produced by the toroidal mirror were also directly measured in front of the TOF electron spectrometer. For this measurement, a razor blade was scanned transversal across the XUV beam at different longitudinal positions along the beam axis. The position of the razor blade was controlled by the manipulator designed to hold the liquid jet. A photodiode of the same type as the one used in the HHG beamline was used to detect the XUV photon flux behind the razor blade. The photodiode current was recorded with an amperemeter depending on the transversal razor blade position x. For a beam exhibiting a Gaussian intensity profile, the devolution of the diode current $I(x)$ for a specific longitudinal blade position is proportional to the complementary error function:

$$I(x) \propto 1 - \frac{2}{\sqrt{\pi}} \int_x^\infty e^{-\left(\frac{t}{\sigma}\right)^2} dt \quad , \tag{5.2}$$

where σ denotes the Gaussian width of the beam. The beam radius can then be inferred from fits of equation (5.2) to the data. The devolution of the FWHM beam radius w depending on the longitudinal position z is described by the equation:

$$w(z) = w_0 \sqrt{1 + \left(\frac{z - z_0}{z_R}\right)^2} \quad , \tag{5.3}$$

where z_0 denotes the position of the focus and w_0 denotes the beam waist, which is the beam radius at the position of the focus. The Rayleigh length, which is the distance after the beam radius has increased by a factor of $\sqrt{2}$, is indicated by z_R. The Rayleigh length describes the depth of the focus.

An exemplary result from the determination of the beam radius, evaluated for the 21^{st} harmonic, is depicted in figure 5.12. Black circles represent the beam radius depending on position along the beam axis. The graph of a fit function according to equation (5.3) is represented by the red line. For illustration, this graph is mirrored with respect to the abscissa, which represents the center of the beam. From the evaluation of the data, a beam waist of $w_0 = 20.3 \pm 0.6$ µm and a Rayleigh length of $z_R = 6.7 \pm 0.8$ mm are inferred. The resulting value of more than 40 µm of the beam diameter implies that the size of the XUV focus is always larger than the diameter of the liquid jet. Thereby, some photons are passing the jet without taking part in the pump-probe spectroscopy of the liquid sample. Nevertheless, they may interact with the gas surrounding the jet. Photoelectrons from the gas phase are advantageous for estimating the streaming potential of the liquid jet (see section 7.3.1). A Rayleigh length of ≈ 7 mm indicates that the

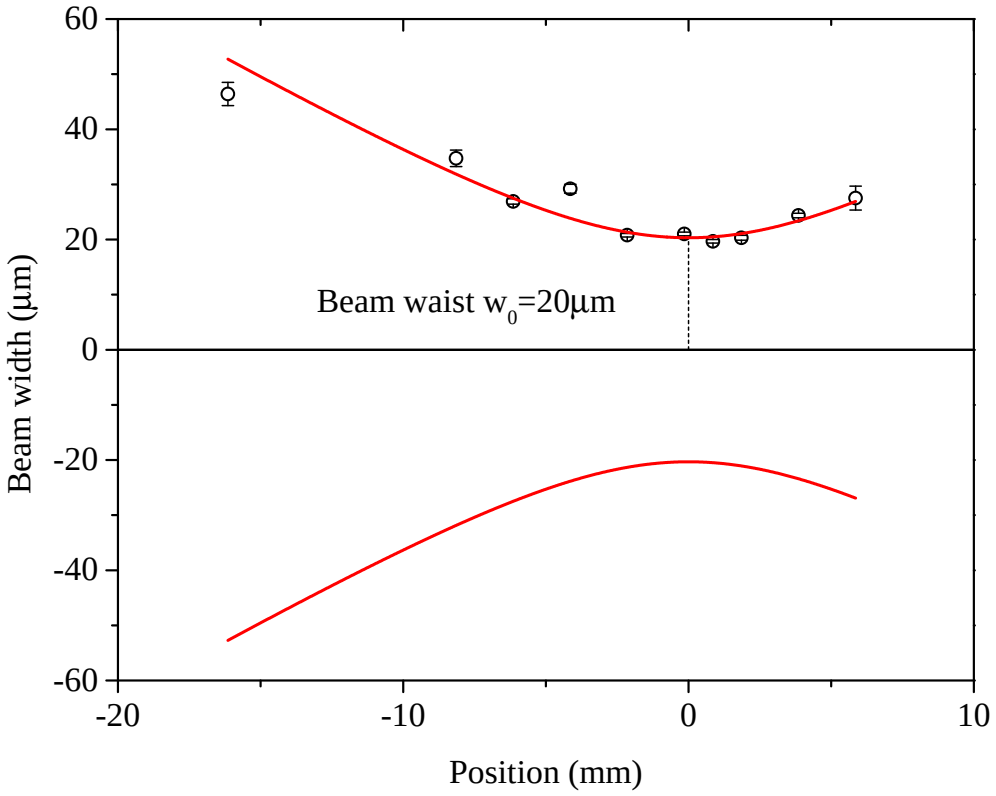

Figure 5.12.: Evolution of the XUV beam width in the interaction region. The circles denote the results from a scanning measurement with a razor blade. The upper red line represents a graph of the fit function according to equation (5.3). The lower red line is a mirror image of the fit function with respect to the abscissa and is displayed for illustration.

interaction region for PES, which is determined by the position of the liquid jet in front of the spectrometer opening, should be positioned with a precision of a few millimeters along the beam axis. This is well established by the setup mechanics.

5.3. Spectral separation of high harmonics

An important characteristic of the zone plate monochromator is its ability to separate adjacent harmonics so that they are blocked by the slit. Especially crucial is the suppression of the next higher harmonic. This is because spectral intensity of the next higher harmonic transferred to the interaction region results in a replica of the electron kinetic energy distribution shifted by 3.1 eV to higher energies in the photoelectron spectrum. For a pump-probe experiment, where the temporal evolution of excited states is examined, such replica is objectionable. The reason for this lies in the fact that the excited states of the solute are usually populated

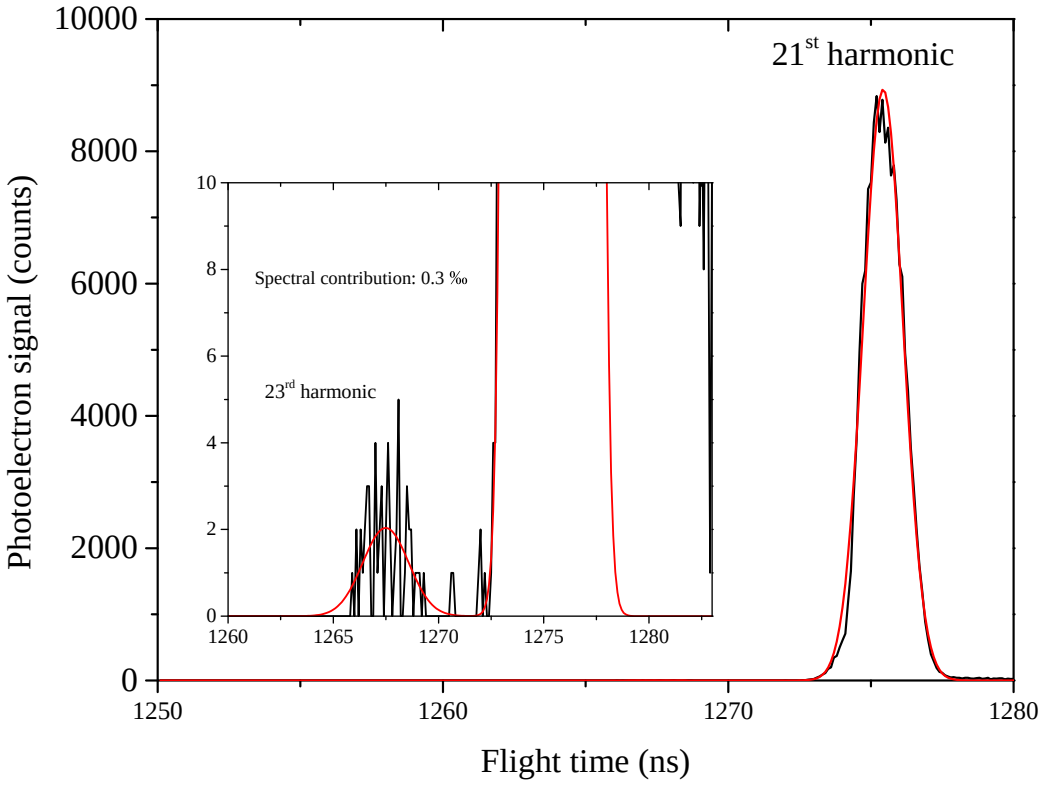

Figure 5.13.: TOF spectrum of argon taken with the THEMIS 600 spectrometer operated in the wide angle mode showing the spectral contribution of the next higher harmonic. The monochromator is tuned to select the 21^{st} harmonic. The red line is a fit of two Gaussian functions to the data.

at a small rate, a few percent of the available molecules at best. In addition, the number density of the solute is typically much smaller than the solvent density. Thus, the weak transient photoelectron signal might be obscured by the replica of the photoelectron signal produced by the XUV light from the large number of solute and solvent molecules in the ground state.

The separation of neighboring harmonics in the focal plane of the first diffraction order produced by the zone plate can be seen from the image shown in figure 5.10 on page 46. This remains a qualitative result though, as a contribution of a few percent from higher harmonics is not apparent on the color scale of the figure, but might be very well pronounced in a photoelectron spectrum. A more accurate measure is achieved by recording the photoelectron yield produced by the desired harmonic and comparing it to the yield produced by the next higher harmonic. For this comparison, photoelectron spectra were taken with the THEMIS 600 TOF spectrometer operated in the WAM. Figure 5.13 shows a time histogram from such a photoelectron spectrum, recorded for argon with the use of the 21^{st}

harmonic. The inset depicts the part of the photoelectron spectrum produced by the 23^{rd} harmonic. From a comparison of the integrated areas of the two spectral components, an intensity contribution of 0.3 ‰ from the 23^{rd} harmonic in the spectrum of the monochromatized 21^{st} harmonic is inferred. Due to scattering of the XUV light at the edges of the grooves of the zone plate structure, a small amount of intensity from higher harmonics is transmitted through the slit. To maintain such a clear separation it is crucial to provide a good focus of the IR driving laser in the generation medium. Any aberration such as spacial chirp of the laser or non-uniform focus will be directly imaged by the zone plate, thus disturbing the spectral separation.

5.4. Spectral bandwidth of the monochromatized XUV light

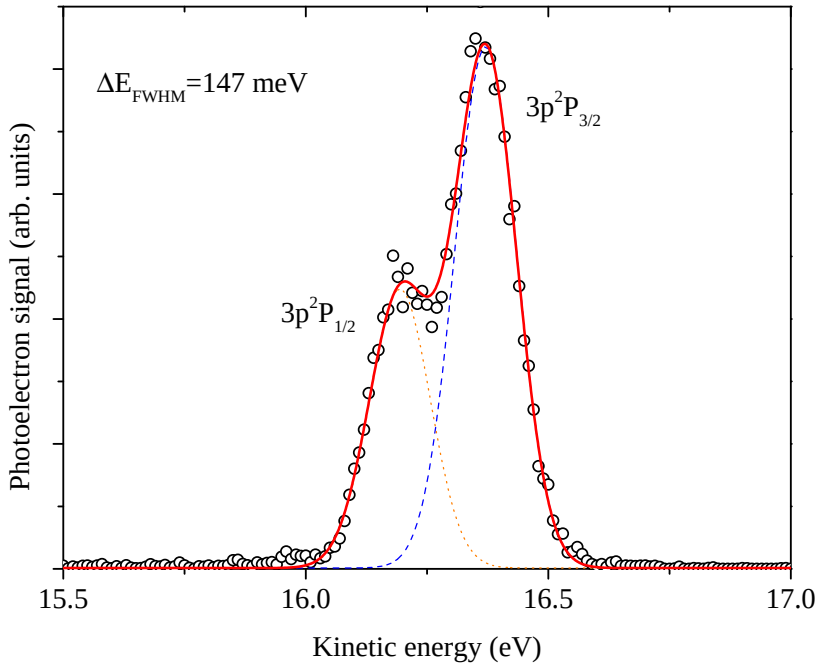

Figure 5.14.: Photoelectron spectrum of argon recorded with the THEMIS 600 spectrometer. A sum of two Gaussian functions with fixed separation of 0.177 eV and equal widths was fitted to the data. The corresponding graph is depicted by the red line. The contributions of the two states originating from the spin-orbit splitting are represented by the dotted orange line and the blue dashed line, respectively. The harmonic radiation is found to have a spectral bandwidth of 147 meV (FWHM).

In order to preserve the short pulse duration of the XUV light, the monochromator should transmit a complete spectral bandwidth of the selected harmonic. The energy resolution of the HHG beamline is thus determined by the spectral bandwidth of the harmonic generated in the HHG cell. The bandwidth of the selected harmonic is inferred from a PES experiment conducted on argon gas. The photoelectrons originate from ionization of the 3p orbital of the argon atom and form a double-peak structure in the spectrum. This doublet appears due to the spin-orbit splitting of the residual Ar^+-ion and has an energy separation of 0.177 eV [65]. In order to resolve the spin-orbit splitting, the TOF spectrometer was operated in the drift mode, which provides a higher energy resolution of approximately 25 meV at an electron kinetic energy of 20 eV.

Figure 5.14 depicts the result of a measurement for the characterization of the HHG bandwidth. The photoelectron signal produced with the 21^{st} harmonic of the driving IR laser is represented by black circles. A fit of a sum of two Gaussian functions with a fixed separation of 0.177 eV and equal widths reproduces the photoelectron signal. The graph of the fit function is represented by the red line, while the individual contributions of ionization channels associated with the formation of the $3p^2P_{1/2}$ and the $3p^2P_{3/2}$ states of the Ar^+-ion are represented by the orange dotted line and blue dashed line, respectively. The high energy resolution of the spectrometer in the lens-less drift mode allows to determine the spectral bandwidth from the fit, which yields a value of 147 meV (FWHM).

5.5. XUV pulse duration

Among the performance characteristics to evaluate the zone plate monochromator, its influence on the temporal envelope of the XUV light pulses upon monochromatization is of great importance. To investigate this issue, the duration of the XUV pulses was measured. Routinely, ultrashort laser pulses are characterized with the use of interferometric techniques such autocorrelation (AC), SPIDER or frequency resolved optical gating (FROG). These measurements employ nonlinear optics in crystals. Due to strong absorption in solid media, they are not applicable for the characterization of pulses in the spectral range of XUV light or even higher photon energies. Nevertheless, an experiment similar to a CC can be conducted employing the effect of laser assisted photoemission (LAPE).

Free electrons may undergo multiple transitions between continuum states through the interaction with a strong laser field. While this was shown by Weingartshofer *et.al.* [66] for free electrons from a scattering experiment, the same effect is observed for electrons generated in a PES experiment [67]. In the particular case of photoelectrons, the effect is called LAPE and has been used to characterize ultrashort light pulses from HHG sources and FELs [38, 43, 44, 67, 68]. In the case of HHG light pulses, a part of the IR pump pulse can be separated and overlapped with the XUV pulse. In this way, the IR dressing pulse and the XUV pulse are automatically synchronized with each other. While the latter generates photoelectrons from a sample, e.g. a noble gas, a part of the free electrons interacts

with the electric field of the IR laser pulse in the LAPE process, giving rise to additional peaks in the photoelectron spectrum. These spectral sidebands arise at higher and lower kinetic energies compared to the undisturbed photoelectron spectrum. The intervals between the sidebands and the undisturbed peak are equal to multiple integer values of the IR photon energy. The kinetic energy E_{kin} of the photoelectrons from the CC measurement can be inferred from the following equation:

$$E_{kin} = \hbar\omega_{XUV} + N\hbar\omega_{IR} - E_{bin} \tag{5.4}$$

Here, $\hbar\omega_{XUV}$ and $\hbar\omega_{IR}$ denote the photon energies of the XUV and IR light, respectively, and E_{bin} accounts for the binding energy of the initial electronic state from which the photoelectrons originate. The integer number N denotes the number of IR photons absorbed or emitted during the process of LAPE.

To observe pronounced but yet undisturbed sidebands in the photoelectron spectrum, the value of the IR intensity of the dressing laser is confined by two boundaries. A lower limit for the intensity is estimated by Delone *et. al.* [69] by evaluating matrix elements of continuum-continuum transitions induced by the IR field. It was shown that efficient LAPE is observed for intensities larger than $(\omega_{IR})^{10/3}$ (in atomic units), resulting in an intensity value of 2.5×10^{12} W/cm^2 for laser radiation with a central wavelength of 800 nm. In practice, the upper limit for the intensity of the dressing laser is often stated to be in the order of 10^{13} W/cm^2 [3, 38]. By restricting the IR intensity to values below this limit, other strong-field effects are avoided. These effects include above threshold ionization (ATI) and depletion of the ground state population due to a high amount of strong-field ionization in the IR laser field.

For a given IR intensity, the intensity of the sidebands generated in the LAPE process is a function of the temporal overlap of XUV and IR pulse. Therefore, the duration of the XUV pulse can be inferred from a series of photoelectron spectra where the time delay between the two pulses is varied, providing that the duration of the IR pulse is known. The ionization yield S_N, which represents the integrated photoelectron signal of the N^{th} sideband, is a function of the delay τ and is proportional to the convolution of the intensity envelope I_{XUV} of the XUV pulse and the $|N|^{th}$ power of the intensity envelope I_{IR} of the IR pulse:

$$S_N(\tau) \propto \int_{-\infty}^{\infty} I_{XUV}(t) I_{IR}^{|N|}(t-\tau) dt \tag{5.5}$$

This relation follows from the description of the $1_{XUV}N_{IR}$-multiphoton ionization process in the framework of perturbation theory.

The temporal envelopes of the XUV and IR light pulses are assumed to exhibit Gaussian shapes. Then, they can be expressed proportional to $\exp(-t^2/\tau_{XUV}^2)$ and $\exp(-t^2/\tau_{IR}^2)$, with the Gaussian widths τ_{XUV} of the XUV pulse and τ_{IR} of the IR pulse, respectively. It follows from equation (5.5) that the envelope of the ionization yield of the sidebands exhibits a Gaussian shape, too:

$$S_N(\tau) \propto exp(\tau^2/\tau_N^2) \quad . \tag{5.6}$$

Here, the width τ_N of the Gaussian function describing the ionization yield of the N^{th} sideband is calculated from the widths of the XUV and IR pulse according to the following equation:

$$\tau_N^2 = \tau_{XUV}^2 + \frac{\tau_{IR}^2}{|N|} \tag{5.7}$$

The relation expressed in equation (5.7) illustrates that the temporal width of the cross-correlation signal decreases with an increase of the order N of the sideband, eventually approaching the value of the XUV pulse duration.

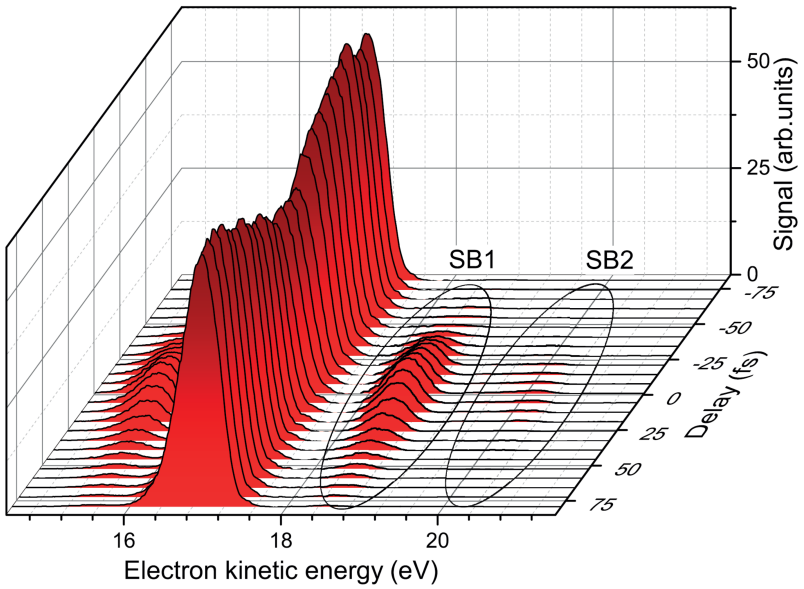

Figure 5.15.: Cross-correlation measurement between the XUV pulse, in this case the 21^{st} harmonic, and the IR pulse (reprinted with permission from ref. [52]). Due to the effect of LAPE, sidebands appear in the photoelectron spectrum, depending on the temporal overlap of the two pulses. The first and second sideband are labeled SB1 and SB2, respectively.

Figure 5.15 shows an exemplary series of photoelectron spectra of argon recorded with the use of the 21^{st} harmonic in the presence of the IR dressing laser. The spectra are displayed on the scale of photoelectron kinetic energy and they are displaced according to the time delay between the XUV and IR pulse. The individual measurements of the series were recorded under the same conditions, i.e. the same argon pressure, acquisition times, laser power and XUV photon flux. The intensity of the IR pump pulse for the harmonic process was reduced to 1.5×10^{14} W/cm^2 to avoid spectral broadening of the XUV light [30]. The intensity of the IR dressing pulse was kept in the order of 1.7×10^{12} W/cm^2. Under this condition, three sidebands appear at each side of the main ionization peak in the photoelectron spectrum. The duration of the IR dressing pulse in the interaction region was measured with the SPIDER technique, and acquired a value of 25 fs.

The photoelectron yield of the individual sidebands present in the CC measurement was integrated and plotted in terms of the time delay between the two pulses. The result is presented in figure 5.16. In the main panel, the normalized integrated signal of the third sideband SB3 is shown by black circles, while the graph of a Gaussian fit to the data is represented by the red curve. The fit yields a CC width of 45 fs. Taking the IR pulse duration of 25 fs into account, from (5.7) results an duration of the XUV pulses of 43 fs. The inset of the figure depicts the normalized

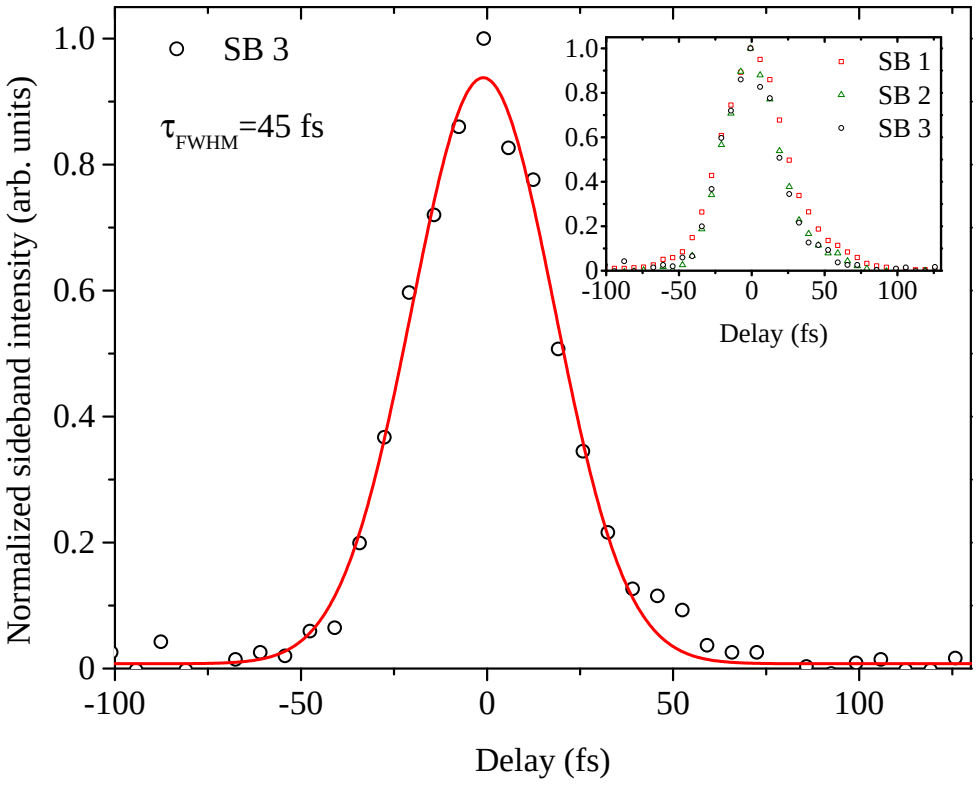

Figure 5.16.: Integrated intensity of the third sideband (black circles) as a function of the time delay between the XUV and IR pulses. The graph of a Gaussian function fitted to the data is represented by the red line. The inset depicts the integrated intensities of the first, second and third sideband, respectively.

integrated photoelectron yield of the three sidebands SB 1, SB 2 and SB 3. The decreasing half width of the sidebands with increasing order is apparent, although the difference between the second and third sideband is already very small. The evaluation of the CC series for the other two zone plates, which select the 17^{th} and 25^{th} harmonic, yielded comparable results.

Apart from the appearance of sidebands, the photoelectron spectrum exhibits additional changes. Due to the presence of the IR laser, the ionization threshold of the atoms undergoes a ponderomotive energy shift to higher values [67]. Accordingly,

the photoelectrons generated by the XUV pulse experience a higher binding energy and the photoelectron kinetic energy distribution is shifted to lower values [67]. This shift is due to an AC stark effect and it is only observable when the two light pulses overlap in space and time. The value of the shift equals the ponderomotive energy of the IR laser (see equation 3.4 in section 3.1). The applied IR intensity can be inferred from the ponderomotive shift of the photoelectron spectrum. Furthermore, the peaks in the photoelectron spectrum are broadened.

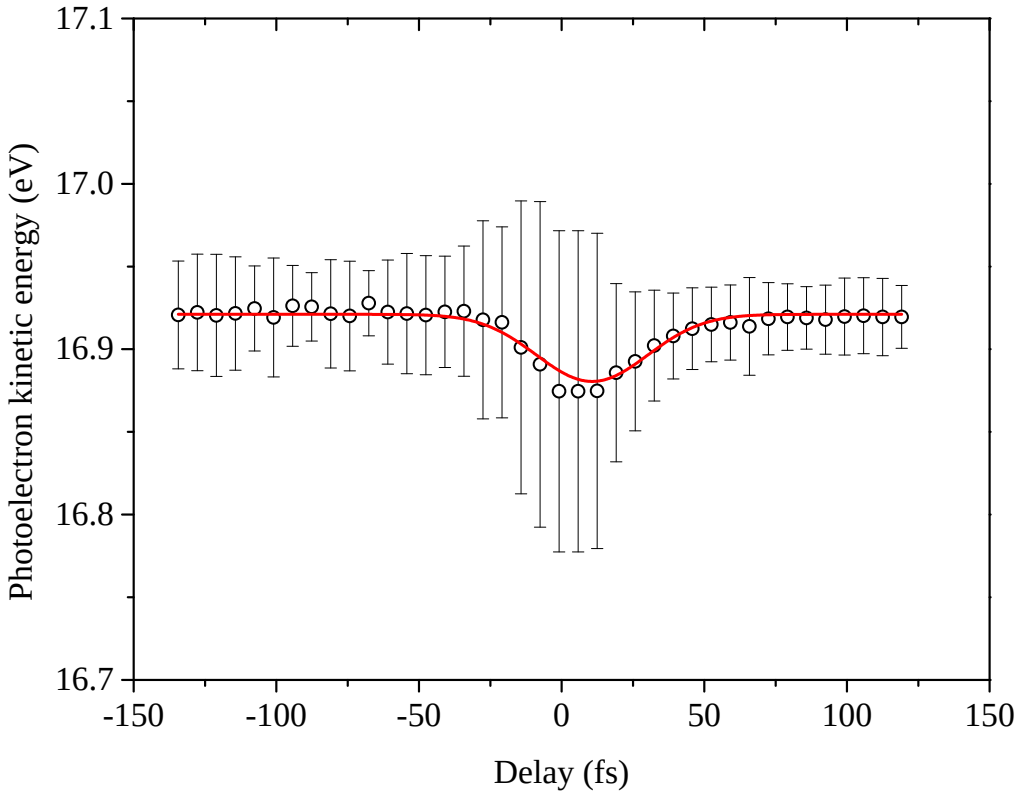

Figure 5.17.: Dependency of the ponderomotive shift (black circles) of the main photoelectron peak of argon on the time delay between the XUV and IR pulses in the CC measurement. The solid red line represents the graph of a Gaussian function fitted to the data.

5.5.1. XUV pulse duration depending on line density

The size of 20 mm of the footprint of the XUV light on the monochromator surface and the length of the zone plate area of 38 mm allows to test the temporal performance of the zone plate at different line densities of the structure. For this purpose, additional CC series were recorded at high and low line density and compared to the result presented in the previous section, which were acquired from CC series recorded at the central line density. These two additional series were

taken at positions 6.5 mm before and behind the central position. Figure 5.18 depicts the integrated photoelectron yield of the third sideband SB3 for the three series. The FWHM pulse duration of the XUV light monochromatized with with the zone plate operated at the three line densities is different. The CC curve of the high line density measurement exhibits the largest value of 109 fs, while the XUV pulse monochromatized at the low line density exhibits a duration of 42 fs. The

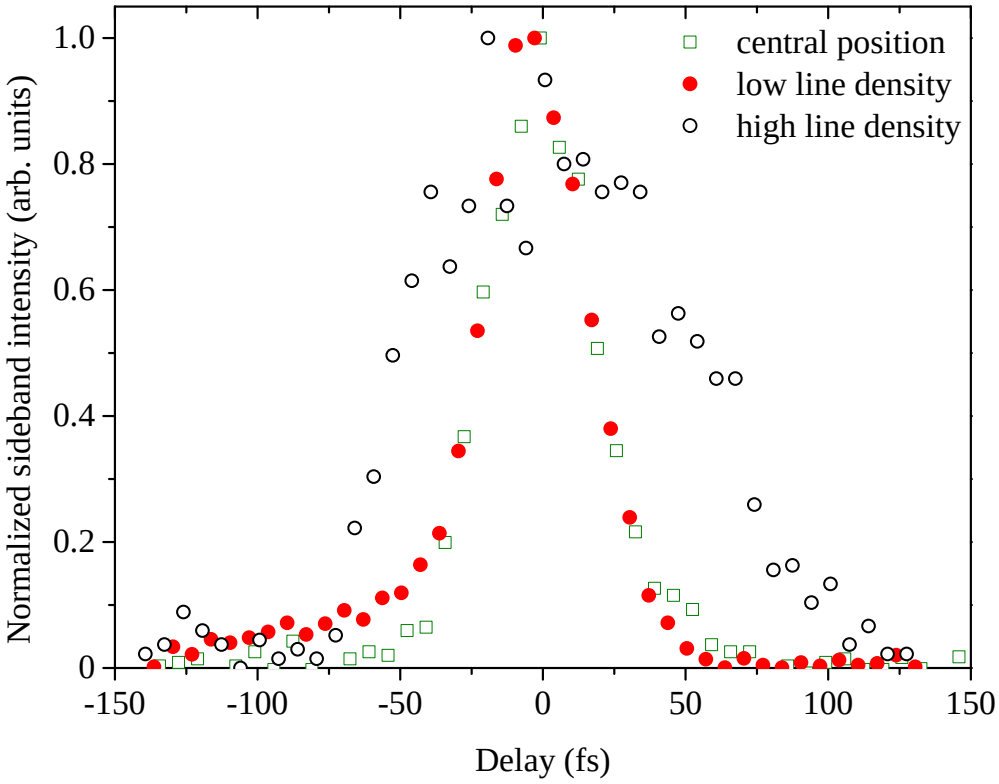

Figure 5.18.: Comparison of CC width at different line densities of the zone plate. The CC curve acquired at a high line density (open circles) exhibits a significantly broader width compared to the CC central position (open squares). The latter is similar to the CC acquired at a low line density (filled circles).

reason for the similar pulse duration of the XUV light monochromatized at low line density and at the central position lies in the fact that the difference in the structural periods of the zone plate at these positions is small. The corresponding difference to the high line density position is much larger, resulting in a larger difference of the CC width compared to the other two configurations.

Since the variation of the line density of the zone-plate monochromator is a opportunity of the device, the results for the high and low line density are presented for completeness, only. During this work, the monochromator is routinely operated at the central line density. Firstly, the spectral separation of neighboring harmonics

is sufficiently large so that the high line density is not needed. Secondly, the gain in pulse duration is not very high upon changing from central illumination of the monochromator to lower line density. Thirdly, a change of the illumination region from the central to an outer area shifts the focal position of the monochromatized XUV beam. Since the other optics in the beamline and the liquid jet as target for the PES experiment can only be moved in a small range, a change of XUV focus position is difficult to compensate.

6. Summary of Part I

Summarizing Part I, an experimental setup for ultrafast time-resolved XUV photoelectron spectroscopy of liquids has been successfully developed and characterized. This work demonstrates for the first time the capability of an ORZP-based monochromator to select a single harmonic of femtosecond pulse duration from a laser driven HHG light source.

The monochromator is designed to choose between the 17^{th}, 21^{st} and 25^{th} harmonic of a Ti:sapphire laser, which corresponds to photon energies of 26.35 eV, 32.55 eV and 38.75 eV, respectively. The novel type of monochromator has been tested according to the list of requirements imposed on monochromators, which was outlined in section 3.2. The rating of the fulfillment of these requirements is summarized in the following table, together with the main performance characteristics of the device. It should be emphasized that the ORZP monochromator combines

requirement	value	rating
spectral purity	0.3 ‰	+
transmission	20 %	++
focusing	40 µm	+
temporal resolution	43 fs	++
pointing stability		++

Table 6.1.: Evaluation of the performance characteristics of the ORZP monochromator according to the requirements listed in section 3.2.

reflection, focusing and dispersion properties in one optical element. Together with a refocusing mirror, it allows for the high transmission efficiency of 20 % through the beamline and stable beam pointing, since the incorporation of less optical elements reduces the effort for alignment mechanics. The spectral purity of the monochromatized XUV light is high. The percentage of spectral intensity of adjacent harmonics transmitted through the beamline amounts to 0.3 ‰ only. Since the design of the ORZP was carried out under the emphasis of an optimal balance between energy and time resolution, the resulting XUV pulse length of 43 fs represents an excellent value for a monochromator employing just one diffractive element.

In order to change between the different harmonics, the flat ORZP substrate is simply translated along its surface. The simplicity of this alignment procedure leads to the high pointing stability of the system.

Possessing the capability to monochromatize ultrashort light pulses with little

temporal distortion, the present monochromator competes against more demanding concepts of monochromators such as TDCMs. A comparison of the ORZP monochromator and grating-based monochromators with respect to their specifications is listed in table 6.2. The zone-plate setup offers the largest transmission efficiency due to a high diffraction efficiency together with the combination of a single refocusing mirror only. Therefore, also the alignment effort is much lower compared to TDCMs with four or even six optical elements. The temporal distortion of a few 10 fs is larger than for the TDCMs, which can provide nearly transform limited pulses. Nevertheless it is an excellent value for a monochromator employing just one diffractive element. The monochromatized XUV radiation is

type	efficiency (%)	elements	pulse stretch	alignment
single grating	10	one/two	up to ps	+
double grating[a]	2.6	two/four	none or few fs	–
off-plane TDCM[b]	18	four/six	none or few fs	– –
ORZP[c]	20	one/two	few 10 fs	+

[a] From ref [43].
[b] From ref [44].
[c] This work.

Table 6.2.: Comparison of the specifications of different monochromators for XUV applications based on diffraction techniques. Values for the efficiency refer to the complete beamline including collimating and focusing mirrors if employed.

shown to exhibit a spectral bandwidth in the order of 150 meV and is focused to a spot of 40 µm in diameter.

The small focal spot, the high spectral purity and the ultrashort duration of the monochromatized XUV pulses represent ideal experimental conditions for time-resolved PES studies of liquids and solid samples.

Part II.

Application of the XUV light source in experiments with liquid micro-jets

7. XUV photoemission spectroscopy of aqueous salt solutions

7.1. Introduction to aqueous salt solutions

In the present chapter, the capability of the HHG light to probe the valence band of liquids and the valence orbitals of dissolved ions is demonstrated for the case of aqueous sodium halide solutions.

Aqueous halide solutions have been the object of extensive research in chemical physics for many years. The interest in halide ions arises from their presence in atmospheric aerosols [70–72] and their role in atmospheric chemistry [73, 74]. Here, the ion location is of special interest, since chemical reactions occur at interfaces and reactants have to reach or even pass the interface. After it had been demonstrated in molecular dynamics (MD) simulations that halide ions exhibit a non-uniform in-depth density distribution at the water surface [75–79], and with the development of surface-sensitive spectroscopic methods, the research activity for this topic grew. Previously, it was generally assumed that ions are repelled from the water surface. However, large and highly polarizable ions, such as iodide and bromide, are shown to exhibit an enhanced number density in the vicinity of the surface [76–81]. Whereas smaller ions, especially fluoride, are repelled from the surface [75, 82]. In MD simulations of solutions containing mixtures of different ions, the smaller ions replace the larger species in the bulk, which are thus transferred to the interfacial region [76, 83]. The ion location with respect to the water-air interface has been studied theoretically [75–78, 84] and experimentally by surface-sensitive nonlinear optical spectroscopy [79, 85–87].

The invention of the liquid micro-jet technique by Faubel *et.al.* [88] enabled to apply surface-sensitive photoelectron spectroscopy to the investigation of the electronic structure of liquid water [89–92], and aqueous salt solutions [93–95]. The liquid micro-jet technique allows to study the free liquid surface in vacuum, which is a prerequisite for PES experiments. PES studies based on the application of XUV light bring along the advantage that the electronic structure of occupied states of the solvent and of dissolved species are characterized via direct one-photon ionization. The binding energy of dissolved ions in aqueous solution is an important value, since it is a measure of their chemical reactivity. The surface sensitivity of the method of PES arises from the small effective electron attenuation length (EAL) for electrons possessing kinetic energies in the range of 10 to 100 eV. This is the case for photoelectrons ionized by XUV light from the valence shell of atoms and molecules. Although precise values for the EAL are under debate for liquids,

typically escape lengths in the order of one nanometer are reported for electron kinetic energies up to 100 eV [96–98].

Results from PES experiments on aqueous sodium iodide and mixed aqueous sodium iodide and sodium chloride solutions with varied concentrations are presented in the course of this chapter. The electronic structure of the valence band of water and the vertical binding energy (VBE) of the halide ions are reported to be independent of the concentration in PES experiments with soft X-ray radiation from synchrotron sources [90, 93]. The VBE of the halide ions may change by ≈ 0.1 eV though, as it was suggested from MD simulations [76]. Changes in the VBE depending on the halide concentration are also reported from a single-pulse pump-probe experiment [99], although in this study it was not possible to distinguish whether the changes are due to a modified ground state or changes in the charge-transfer-to-solvent (CTTS) state. The present results acquired with XUV light enable to address this question since only the ground state of the ions is probed. The chapter starts with a description of the electronic structure of the water molecule, the electronic structure of liquid water and the VBE of halide ions in aqueous solutions. The peculiarities of the liquid micro-jet technique are described. This includes the origin of the streaming potential on the jet surface, and the difficulties of determining the EAL in water. The experimental setup for photoelectron spectroscopy of liquids is presented in the version developed in ref [55]. The sample preparation, experimental procedure and data evaluation are described in detail. Presented results include the dependency of the photoelectron yield of halide ions depending on the ion concentration and the influence of the salt concentration on the electronic structure of the valence band of water.

7.2. Electronic structure of water and aqueous solutions

7.2.1. Electronic structure of the water molecule

The electronic structure of the water molecule arises from the combination of the atomic orbitals of the oxygen atom with the 1s orbitals of the two hydrogen atoms. The resulting energy levels, binding energies and corresponding orbital pictures acquired from MD calculations are depicted in figure 7.1 [90]. The electronic ground state is labeled as $(1a_1)^2(2a_1)^2(1b_2)^2(3a_1)^2(1b_1)^2$ state. The $1a_1$ orbital of water stems from the 1s atomic orbital of oxygen and does not participate in the bonds with the hydrogen atoms. The three next higher molecular orbitals, namely the $2a_1$, $1b_2$ and $3a_1$ orbital, all contribute to the bonds. The unaltered p_z^2-orbital of the sp^2-hybridized oxygen atom stands vertical on the molecular plane. With no contribution from the hydrogen 1s orbitals it forms the $1b_1$ non-bonding orbital which is the highest occupied molecular orbital (HOMO) of the water molecule. The other three orbitals, namely $3a_1$, $1b_2$, and $2a_1$, contribute to the OH-bond.

Figure 7.2 displays a photoelectron spectrum of the outer valence orbitals of gaseous water obtained in the present work with the use of the 21^{st} harmonic

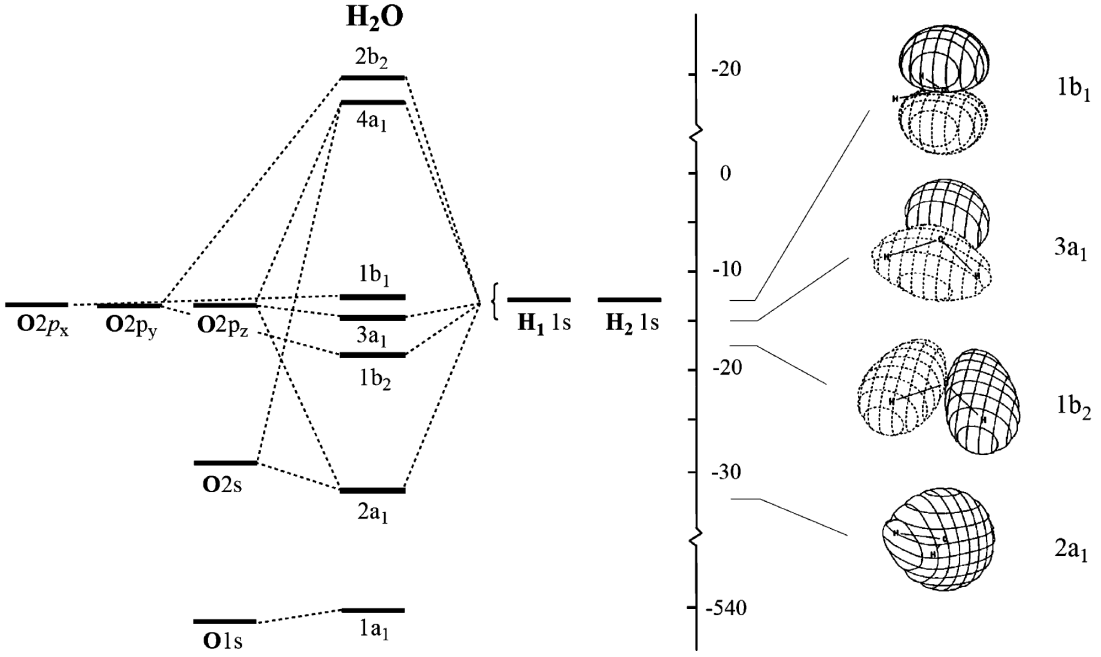

Figure 7.1.: Energy level diagram and orbital pictures of the water molecule (reprinted with permission from ref. [91]). The orbital picture of the lowest molecular orbital, the $1a_1$, is not displayed.

(32.55 eV). The spectrum is displayed in terms of the binding energy. The photoelectron signal consists of three contributions representing the $1b_1$, the $3a_1$ and $1b_2$ orbitals described above. Vibrational subfeatures are resolved for the $1b_1$ and $1b_2$ orbitals, but only the three strongest vibrational states of the $1b_1$ orbital are considered in the fit of Gaussian functions to the data. Table 7.1 lists the binding energies resulting from the fit. Since the spectrum was taken in the vicinity of a liquid jet, and is therefore influenced by a streaming potential (see section 7.3.1), the binding energy scale is calibrated so that the $1b_1$ orbital matches the literature value of 12.62 eV [100]. The five Gaussian functions fitted to reproduce the photoelectron signal of gaseous water will be incorporated in the evaluation of the photoelectron spectra of liquid water, which is described below.

	$1b_1$(eV)	$1b_1(\nu_1)$ (eV)	$1b_1(\nu_2)$ (eV)	$3a_1$(eV)	$1b_2$(eV)
BE	12.62	13	13.37	14.86	18.75

Table 7.1.: Binding energies inferred from a fit of Gaussian functions to the photoelectron signal of the outer valence orbitals of gaseous water.

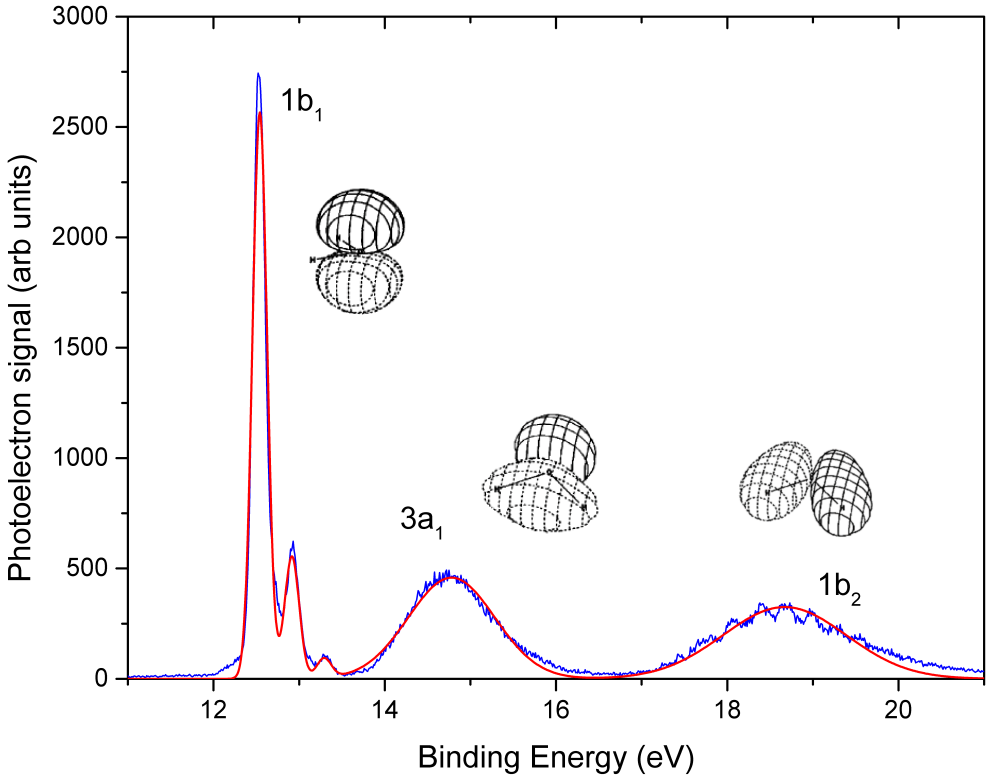

Figure 7.2.: XUV photoelectron spectrum of gaseous water (blue line). Displayed are the three outmost valence orbitals together with orbital pictures reprinted with permission from ref [90]. The red line represents a fit of Gaussian functions to the data.

7.2.2. Electronic structure of liquid water

An exemplary photoelectron spectrum of liquid water acquired with the present setup is shown in figure 7.3. Since the focus of the XUV light is in the order of 40 µm, and therefore larger than the liquid jet, apart from ionization of liquid water some part of the evaporated water molecules surrounding the jet are probed as well. For this reason the displayed spectrum exhibits features from both, the liquid and gaseous phase. Although the presence of photoelectron signals from gaseous water makes the decomposition of the spectra more complex, it also gives a measure of the streaming potential and allows to calibrate the binding energy scale [101].

From the ionization contributions of the gas phase, the sharp $1b_1$ peak is clearly pronounced in the spectrum. The other contributions are more concealed by the photoelectron signal originating from water molecules in the liquid phase. Compared to the molecules in the gas phase, the photoelectron signal of the molecules in the liquid phase is altered. The peaks in the photoelectron spectrum are shifted towards lower binding energies by approximately 1.3 to 1.5 eV [90], and they are

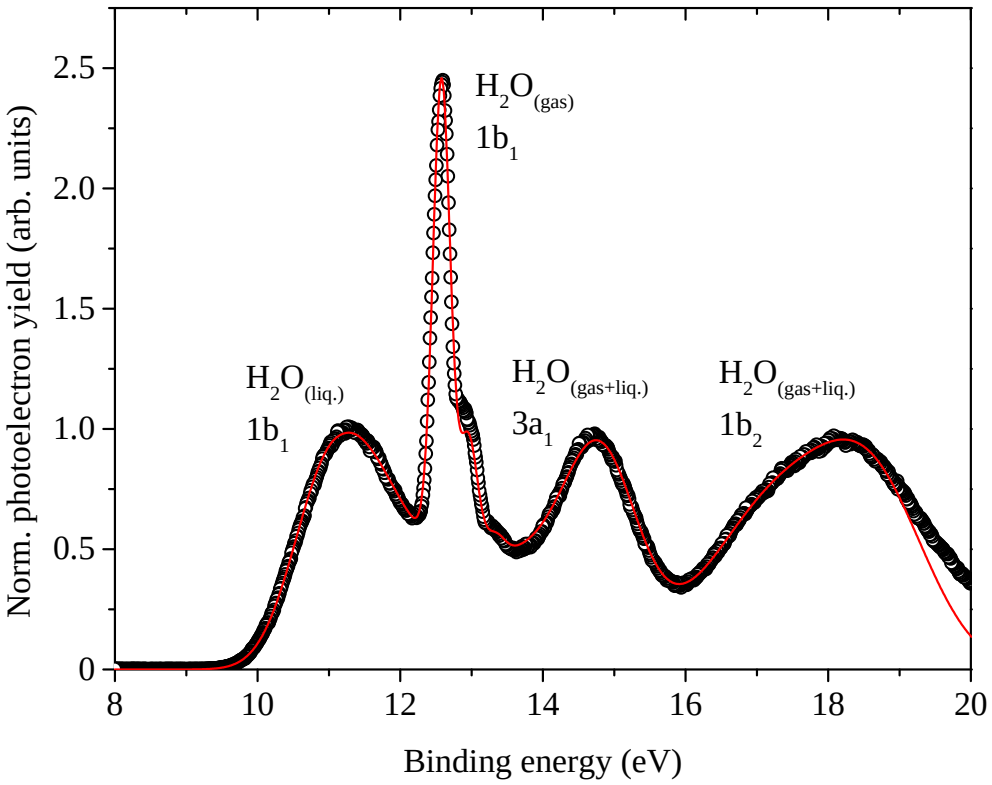

Figure 7.3.: XUV photoelectron spectrum of liquid and gaseous water (circles). Displayed is the photoelectron signal originating from the valence orbitals of water with contributions from gaseous water molecules surrounding the liquid jet. A sum of Gaussian functions taking the photoelectron signal from liquid and gaseous water into account is fitted to the data according to the routine described in section 7.6.2.

considerably broadened. Especially the $3a_1$ peak is broadened to an extend that it exhibits a flat top as if it consists of two contributions. The interaction of the molecules in the hydrogen bond network of the liquid results in a delocalization of the orbitals, which leads to the energetic shift and broadening of the photoelectron peaks. The magnitude of the binging energy shift is explained with the Born-model of solvation, which has been originally invented for ions in solution [102] but then applied to solvent molecules [90, 103, 104]. According to the Born model, the Gibbs free energy of solvation ΔG^{Born} is given by the relation:

$$\Delta G^{Born} = -\frac{(Ze)^2}{8\pi\epsilon_0 R}\left(1 - \frac{1}{\epsilon_{opt}}\right) = E_{aq} - E_g \quad , \tag{7.1}$$

where Ze denotes the charge, R is the radius of the cavity occupied by the relevant species and ϵ_{opt} is the optical permeability. The binding energy shift $\Delta E_{bin} = E_g - E_{aq}$ between the binding energy E_g of the gaseous species and the

binding energy of the liquid species E_{aq} is then given by the change in the solvation energy from the initial state i to the final state f denoted by $\Delta G_f - \Delta G_i$. Since the initial state of the water molecule is neutral, only the final state contributes to the binding energy shift $\Delta E_{bin} = \Delta G_f$. The free energy of solvation equals the energetic shift $E_g - E_{aq}$ between the binding energy E_g of the species in the gas phase and the binding energy E_{aq} of the species in aqueous solution. With an electrical permittivity $\epsilon \approx 1.8$, and a cavity radius of 2.24 Å, equation (7.1) yields an energetic shift of 1.4 eV.

Energy shifts acquired with the Born model have to be treated with care though, and can be used as estimations only. The solvation energies in the model represent adiabatic values, which means that the Gibbs free energy corresponds to the state of the solution in which the solvent has relaxed around the species that was photoionized. Since the process of photoionization is much faster than the nuclear dynamics of the solvent, the photoelectron does not carry information of the relaxed final state [103]. The measured binding energy in the photoelectron experiments are therefore called vertical binding energies (VBEs).

With a binding energy of 11.31 eV, the liquid $1b_1$ orbital is energetically shifted to lower values by 1.31 eV compared to its value in the gas phase. It represents an outstanding feature as it is nearly well separated from the rest of the spectrum. Due to the broadening of features in the photoelectron spectra of liquids, the vibrational structure is not resolved. The broadening is explained by fluctuations in the hydrogen-bond configurations of the molecules [105, 106]. The contributions from the $3a_1$ and $1b_2$ orbitals are partially obscured as they are overlayed by the gas spectrum. Nonetheless they can be retrieved by subtracting a gas phase spectrum as it was done by Winter and coworkers [90] or by including the gas phase contributions in the fit as it is done in the present work. The most remarkable difference between liquid and gaseous water is a very broad $3a_1$ orbital. A similar alteration has been observed in photoelectron spectra of ice [107], where the $3a_1$ feature in the fully established hydrogen network splits into two peaks due to the strong overlap of $3a_1$ orbitals of neighboring water molecules. The two sub-features of the $3a_1$ orbital then correspond to the bonding and anti-bonding orbital.

7.2.3. Electronic structure of halide ions in aqueous solutions

The VBEs of halide ions in aqueous solutions are increased compared to the binding energies of gaseous halide ions. In the case of iodide and chloride, the VBE is increased from 3.06 to 8.03 eV, and from 3.61 to 9.5 eV, respectively [95]. If the Born model (see equation (7.1)) is applied to the case of halide ions, the final state is neutral and the binding energy shift ΔE is equal to the solvation energy of the initial state ΔG_i. Calculations of the binding energy shift for halide ions in aqueous solutions based on the Born model underestimate the shift, though [104]. The Born model remains a qualitative measure, providing only the sign of the shift. The fact that this model relies on adiabatic states plays a larger role for anions than for water molecules. Better agreements for the binding energy shift of anions are achieved in ab initio calculations. The energy shift observed for the anions

proved to be insensitive of the counter ion [104]. The enhancement of the binding energy implies a stabilization of the highest occupied orbitals of the ions.

7.3. Liquids in vacuum: the liquid micro-jet technique

Photoelectron spectroscopy of liquids requires handling of these liquids in a vacuum environment. The high vapor pressure at the liquid surface, e.g. water has a vapor pressure of 23 mbar at 20°, results in a continuous evaporation of sample molecules. This leads to a number of issues that have to be considered in an experiment.

Firstly, the continuous evaporation of sample molecules deteriorates the vacuum conditions which is unfavorable for the lifetime of electron detectors. Secondly, the mean free path of the photoelectrons decreases with the increase of the residual pressure. Thirdly, the evaporation eventually leads to a frozen sample due to evaporative cooling.

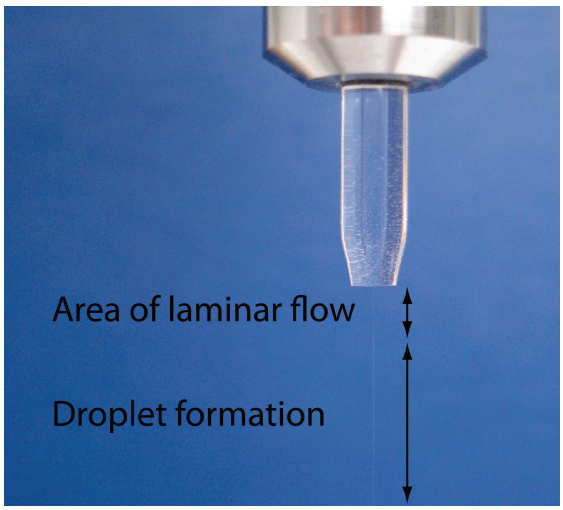

Figure 7.4.: Picture reprinted from ref. [108] depicting a liquid micro-jet formed by the liquid being pressed through the glass nozzle.

The above mentioned obstacles are overcome in the present setup by using the liquid micro-jet technique introduced by Faubel *et.al.* [109]. In this approach, the liquid is introduced into the vacuum chamber through a thin glass capillary. This results in the formation of a liquid jet continuously running at a high velocity as can be seen from figure 7.4. Immediately after the nozzle, the jet has a laminar flow before it turns into a turbulent jet several millimeters downstream of the nozzle. Eventually, the jet sprays into individual droplets that are captured in a cryo pump filled with liquid nitrogen, which is located below the nozzle. The region of laminar flow of the jet can be seen as a liquid rod with a diameter similar to that of the nozzle opening. The photoelectron spectroscopy experiment is conducted in this region of the jet. Evaporative cooling results in a temperature of approximately

280 K in this region of the jet [110]. The present work makes use of capillaries with opening diameters of about 25 µm and a flow rate of 0.4 mL/min, resulting in jet velocities of around 15 m/s.

Although the local pressure in the direct vicinity of the jet is close to the equilibrium vapor pressure of the liquid, the pressure quickly drops with increased distance r from the jet at a rate proportional to the inverse distance $1/r$ [111]:

$$P(r) = \frac{r_0}{r} P_0 \tag{7.2}$$

Here, r_0 represents the radius of the jet and P_0 is the equilibrium vapor pressure. Once the photoelectrons have left the near-surface region of high pressure without being scattered, their mean free path becomes sufficiently long to reach the electron detector, and participate in the experiment.

7.3.1. The streaming potential of liquid micro-jets

Similar to the case of solid samples in photoelectron spectroscopy experiments, the liquid sample has to be conductive and electrically grounded. These requirements prevent undefined bias potentials and the build-up of a positive charge on the sample due to ionization (see section 7.6.1). Bias potentials or charged samples would deteriorate the PES measurement or even impede it completely. Alkali-halide salts are routinely added to polar solvents such as water to establish a conducting sample [91]. This can be omitted if the sample itself contains an ionic solute or is an ionic liquid. The ground contact of the sample is usually established through the contact of the liquid with metal parts in the pipe such as the nozzle holder. Some experimental setups employ nozzles coated with graphite to additionally enhance grounding [95].

Another characteristic feature of the liquid micro-jet technique is the presence of an additional charge on the jet surface resulting from the interaction of the flowing liquid with the nozzle wall. This effect is called electrokinetic charging and the potential created between the sample and the electron detector is often referred to as the streaming potential. The origin of the electrokinetic charging has been described in detail by Preissler *et.al.* [112]. Briefly, the flowing jet exhibits a parabolic velocity profile within the capillary, with a stagnant layer of molecules in the direct vicinity of the capillary wall. In case of water as a sample, the silica surface of the nozzle wall becomes hydrated with -OH groups. Due to electrostatic repulsion and attraction, a diffuse Gouy-Chapman layer containing an excess of positive ions is built within the liquid in the vicinity of the hydrated nozzle wall. The stagnant layer next to the capillary wall contains the highest amount of counterions, but the diffuse layer also extends to some distance into the flowing part of the liquid. Once the liquid exits the nozzle, the charged layer is disrupted from its counterpart, resulting in a charged surface of the liquid jet. The streaming potential is dependent on parameters such as ion concentration in the sample, flow rate of the liquid and on the freshness of the nozzle. A comprehensive study on the possibilities to measure the streaming potential and its dependence on

the concentration of sodium halides up to 3 M has been reported by Kurahashi *et.al.* [95]. Their approach presented in the latter reference allows to extrapolate the streaming potential Φ_{str} from a series of PES measurements of a gas in the vicinity of the liquid jet, while varying the distance between the interaction region and the liquid jet. The latter is treated as an infinite charged rod giving rise to a mirror charge on the entrance electrode (skimmer) of the electron spectrometer. According to this consideration, the streaming potential is described by the relation:

$$\Phi(x) = \Phi_{str} \frac{ln\left(\frac{2Y+x}{x}\right)}{ln\left(\frac{2(Y+x)-r}{r}\right)} \quad . \tag{7.3}$$

Here, $\Phi(x)$ denotes the potential at the interaction region located at a distance x from the liquid jet of radius r, and Y denotes the distance between the interaction region and the spectrometer entrance. The resulting kinetic energy $E_{kin}(x)$ of the photoelectrons, which depends on the distance to the jet, is then calculated according to

$$E_{kin}(x) = E_{ph} - E_{bin} - \Phi(x) - V_0 \quad , \tag{7.4}$$

where E_{ph} denotes the photon energy, E_{bin} is the binding energy and V_0 is an independent bias potential. This model of an infinite charged rod has been refined to include the influence of the nozzle. The supplementary material of ref. [95] presents these two models in detail and discusses their differences. Interestingly, the first model of the infinite rod seems to fit better to the results acquired for an aqueous NaI solution with a concentration of 200 mM while the second model reproduces the results acquired for pure H_2O better.

7.3.2. Probing depth in photoelectron spectroscopy

Photoelectrons generated in a specific region within a sample may be scattered on neighboring atoms or molecules, before they eventually leave the sample. The distance between two consecutive inelastic scattering events is called the inelastic mean free path (IMFP). The IMFP is an ultimate upper value for the probing depth in a PES experiment and represents a material property. However, the actual probing depth might be shorter than the IMFP if elastic scattering is effective. In this case, electrons are redirected out of their way to the detector and lost. Accordingly, the measure that is useful in praxis is the EAL. It represents the length over which the intensity of electrons of a specific kinetic energy has dropped to 1/e of its initial value. The EAL is defined by the electron loss due to both, elastic and inelastic scattering and represents a function of electron kinetic energy. In solid state physics, where the EAL is traditionally measured either by the overlayer technique or from the evaluation of the energy of backscattered electrons, a rich set of experimental data is available for a wide range of materials. Qualitatively, the EAL curve for electrons with kinetic energies between 10 eV and 10 keV for some groups of solids exhibits a very similar trend, which has led to the concept of a universal curve presented by Seah *et.al.* [113]. According to this universal curve,

the EAL shows a minimum between 30 and 100 eV, with a steep rise in the limit of low kinetic energies and a slower rise in the limit of higher kinetic energies.

Such curve has not been established for liquid samples, yet. The reason for this lies partly in the novelty of the method of liquid photoelectron spectroscopy compared to that of solid samples, and partly in the considerably higher difficulties in preparing well defined liquid surfaces. A first approach to extend the concept of the EAL to the liquid phase has been made by Ottoson *et.al.* [96] for the case of liquid water. Here, the photoelectron yield from the 1s orbital of oxygen was measured as a function of photon energy in an experiment using soft X-ray radiation. The evaluation of the EAL was conducted under the assumption of energy independent photoionization cross sections. The length scale obtained from the water O 1s study was then calibrated with the scale acquired from a concentrated NaI solution. In the latter case, the concentration of iodide and sodium ions exhibit a characteristic profile in the vicinity of the liquid surface according to simulations presented by Jungwirth *et.al.* [75].

These findings were later refined by Thürmer *et.al.* [97] taking into account the particular energy-dependent photoelectron emission anisotropy observed for liquid water. This correction represents an important modification, since the resulting EAL values for photoelectrons with kinetic energies smaller than ≈ 70 eV lie well below 1 nm. No minimum is apparent for the EAL as it is in the case of the universal curve for solids, and the EAL values are continuously decreasing for successively smaller kinetic energies.

A different approach to evaluate the EAL of electrons with kinetic energies from 10 to 600 eV in water was presented by Suzuki *et.al.* [98]. In their work, the O 1s signals of liquid water and of gaseous water surrounding the jet were evaluated, and the energy-dependent photoelectron emission anisotropy from ref [97] was included in the analysis as well. Differences in the evaluation arise from considering the particular geometry of the curved surface of the liquid jet, and, most importantly, from incorporating the photoabsorption cross sections. The resulting EAL in water differs for electron kinetic energies below 100 eV. In the latter study, the EAL does not decrease monotonically for energies below 100 eV but settles around a value of ≈ 2 nm. Thus, no solid conclusion on the EAL value in water in the limit of low kinetic energies could be drawn so far.

7.4. Experimental setup for photoelectron spectroscopy on liquids

Figure 7.5 displays a scheme of the vacuum setup for photoelectron spectroscopy on liquids developed in our laboratory [55], which can be applied for both, steady state and time-resolved experiments. The central part of the setup is a cubic chamber housing the interaction region, where the horizontal XUV beam intersects the vertical liquid jet in front of the spectrometer opening. This region marks the interaction region for the PES experiment. A x-y-z manipulator at the top of the

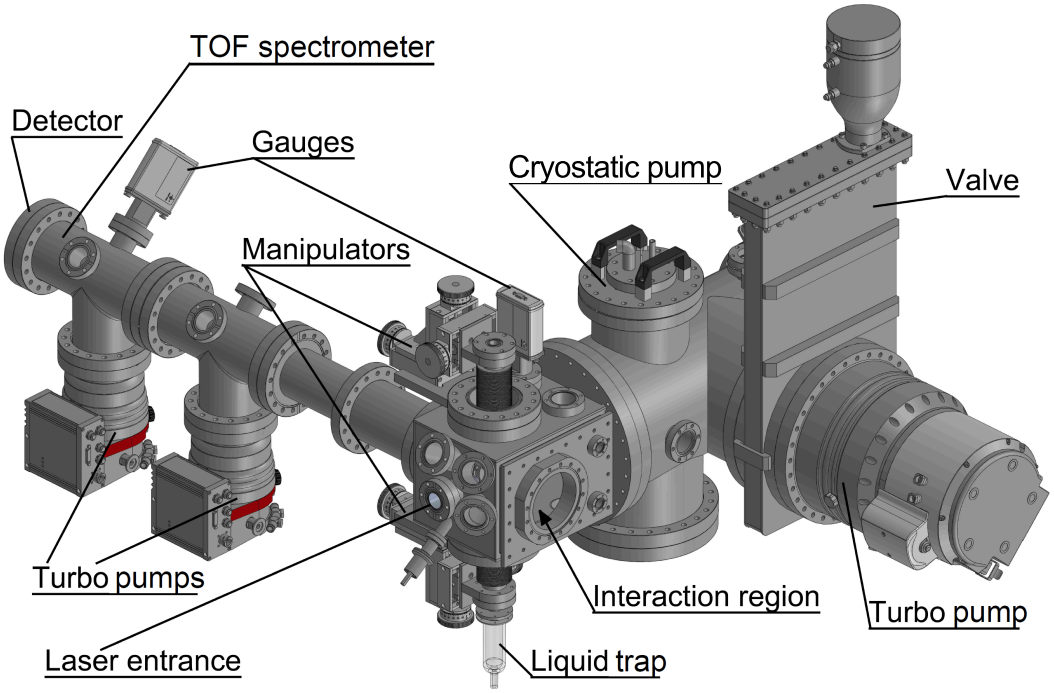

Figure 7.5.: Scheme of the experimental setup for PES of liquids reprinted from ref. [55]. The interaction region of the PES experiment is located in the cubic to which the TOF spectrometer and the manipulator for the liquid jet are attached.

cubic chamber controls the holder for the glass nozzle and allows the positioning of the laminar part of the liquid jet in the XUV focus in front of the electron spectrometer. At the bottom of the cubic chamber, opposite of the liquid jet assembly, a nitrogen filled liquid trap is mounted. This trap catches and retains the majority of the liquid sample that has entered the vacuum chamber.

Attached to the cubic chamber is a pumping section, which enables to maintain a pressure of $\approx 10^{-5}$ mbar during the experiments with the liquid jet. To achieve this, two different pumping techniques are employed. On the one hand, a turbomolecular pump with a pumping speed of 1800 L/s (Pfeiffer, model HiPace 1800) is installed. On the other hand, a cryo-pump filled with liquid nitrogen is inserted in this section of the vacuum chamber. This cryo-pump is especially effective for highly volatile samples such as water. When the cubic chamber has to be vented, either for installing or for deinstalling the liquid jet, the turbomolecular pump, the TOF spectrometer and the XUV beamline can be separated with the use of gate valves. The front plate of the cubic chamber can be dismounted to facilitate the access to the interaction region.

7.5. Experimental procedure

Sodium halide salts were purchased from Sigma Aldrich with a purity higher than 99%, and used without further treatment. Aqueous solutions of sodium iodide were prepared from deionized water (18.2 MΩcm resistivity). In a first step, a parent solution of 6 M concentration of NaI was prepared. Portions of this solution were then diluted in a second step with appropriate amounts of deionized water to prepare NaI sample solutions of concentrations ranging from 100 mM up to 6 M.

Mixed aqueous solutions of sodium iodide and sodium chloride were prepared in a similar manner. Except that in a first step, a sodium iodide solution of 500 mM concentration was prepared. From half of this solution, a mixed solution with a concentration of 500 mM NaI and 4 M NaCl was prepared to serve as parent solution. This parent solution was then diluted with fractions of the remaining half of the NaI solution to form the desired mixtures with varied NaCl concentration but constant NaI concentration of 500 mM.

The samples were injected into the vacuum system by a syringe pump from Teledyne Isco (model 500D) through a thin glass nozzle at a constant flow rate of 0.4 ml/min. After each series of measurements with a given solute concentration, the syringe pump and the feeding tubes were drained and rinsed three times with approximately 50 mL of the following sample. This procedure prevents inaccuracies that would arise from leftover sample of the previous concentration intermixing with the fresh solution.

Static XUV photoelectron spectra were recorded with the THEMIS 600 TOF spectrometer operated in the drift mode to benefit from the high energy resolution of ≈ 25 meV. The zone-plate monochromator was set to select the 21^{st} harmonic. The harmonic process was driven with a low IR pump intensity of $\approx 1.3 \times 10^{14}$ W/cm^2. Under these conditions, the number of photons per pulse in the monochromatized XUV light reaching the sample was approximately 0.4×10^6. This setting was chosen for several reasons. Firstly, a high pump intensity results in spectral broadening of the XUV radiation [30], which is unfavorable in a spectroscopic experiment. Secondly, a high photon flux produces a significant amount of photoelectrons, especially from the large number of water molecules. Restricting the photon flux below 10^6 photons per pulse prevents the electron detector of the spectrometer from saturation. Thirdly, an intense XUV beam results in a highly ionized and hence charged sample. Charging of samples results in distortions of photoelectron spectra. This issue was addressed in recent PES experiments with XUV radiation from FELs and HHG sources [114–116]. Under the present experimental conditions of low photon flux, a charging of the aqueous sodium halide solutions was not observed, as it will be discussed in section 7.6.1.

7.6. Results and discussion

7.6.1. Ionization-induced charging of the liquid jet

Electrostatic charging due to a high degree of ionization has been reported for PES studies conducted with XUV light pulses from HHG and FEL sources [114–116]. Depending on the particular experimental conditions, charging may be caused by the pump light pulse in a time-resolved study or by the XUV probe pulse alone. The present section describes the experiments conducted to investigate whether charging effects occur under the applied conditions due to the ionization of the aqueous solution by the XUV probe light.

Since variation of the XUV intensity is accomplished via changing the intensity of the IR pump laser driving the HHG process, energetic shifts in photoelectron spectra generated with HHG light may occur due to electrostatic charging of the sample, or due to spectral shifts in the XUV spectrum as a result of changes in the harmonic process. To distinguish between these two effects, a series of photoelectron spectra are recorded on argon and on aqueous NaI solution with a concentration of 6 M. The experiments are divided into three steps.

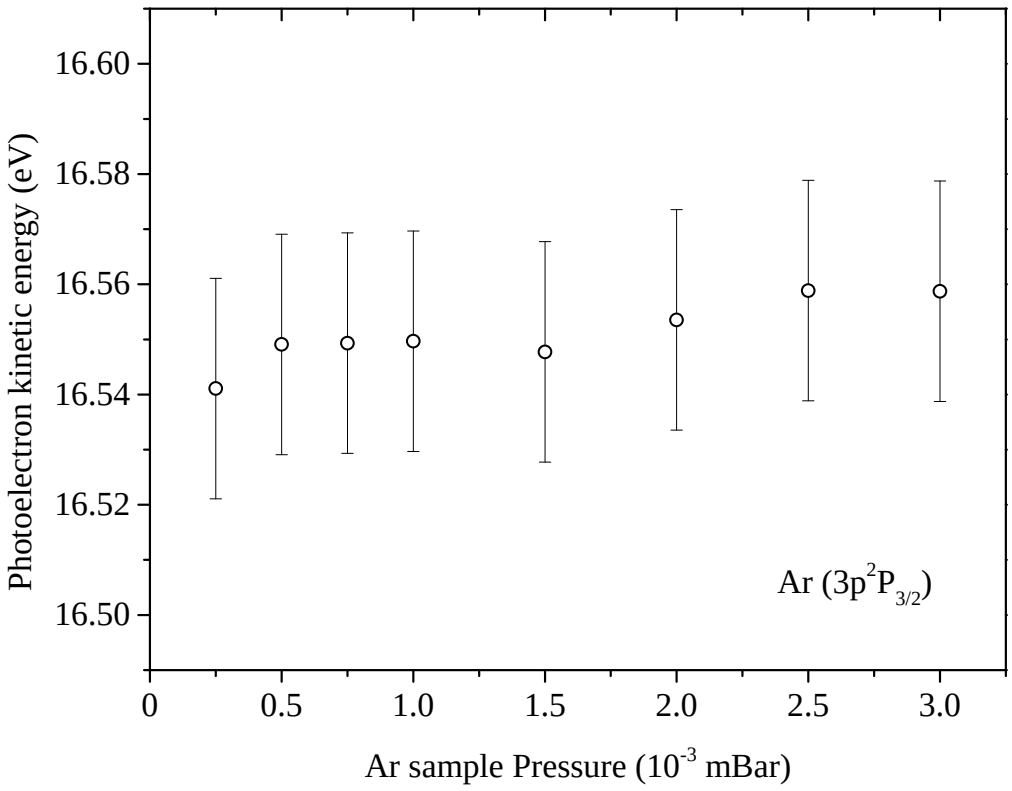

Figure 7.6.: Dependency of the central kinetic energy of photoelectrons ionized from Ar gas on the sample pressure in the interaction region.

Firstly, a series of photoelectron spectra on argon is recorded at a fixed XUV photon flux of 0.6×10^6 photons per pulse and a varied argon pressure. This series allows to judge whether electrostatic charging occurs in argon gas. If this would be the case, the effect should be more prominent in a more dense medium.

In the second step, a series of photoelectron spectra on argon is recorded with varied XUV photon flux and fixed argon pressure. The XUV photon flux is determined by the IR pump intensity used for driving the HHG process. In the absence of the space charge effect in the argon gas, a comparison between the first and the second series allows to determine the spectral shift in the XUV spectrum due to changes in the HHG process.

Finally, a series of photoelectron spectra is recorded on the NaI solution with varied XUV photon flux. The energetic shift of the iodide 5p orbital and the water $1b_1$ orbital are compared to the shift observed in the spectra of the second series. The difference that occurs in this comparison is then accounted to electrostatic charging of the liquid sample.

In the first series, the argon sample pressure in the experimental chamber was varied by an order of magnitude between 2.5×10^{-4} and 3×10^{-3} mbar. The IR pump intensity was fixed at 1.3×10^{14} W/cm^2. The dependency of the kinetic energy of the photoelectrons associated with the ionization channel leading to the formation of the $3p^2P_{3/2}$ state of the residual Ar^+-ion is illustrated in figure 7.6.

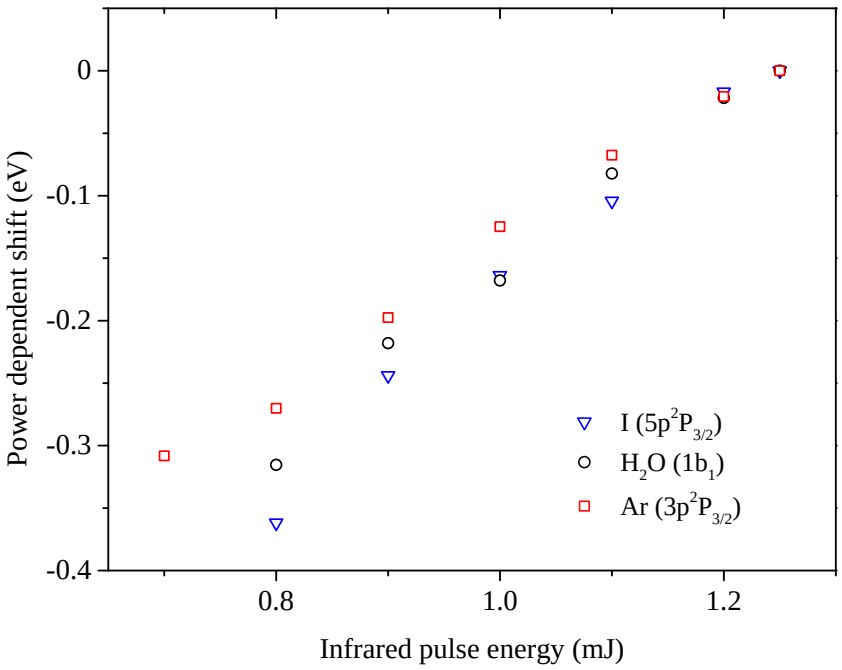

Figure 7.7.: Dependency of the central kinetic energy of photoelectrons ionized from Ar gas, liquid water $1b_1$, and aqueous iodide $5p^2P_{3/2}$ on the XUV flux.

Over the range of applied sample pressures, the kinetic energy of the photoelectrons varies by ±10 meV. Since the HHG energy was found to vary by ±20 meV over a large period of time, it is concluded that the sample density does not have an influence on the photoelectron kinetic energy over the range of applied sample pressures. It is therefore concluded that charging does not occur in argon gas under the present conditions.

In the second series of measurements, the XUV photon flux is changed by varying the pulse energy of the IR pump laser between 0.7 and 1.3 mJ. The argon sample pressure is kept constant at a value of 5×10^{-4} mbar during this series. Since there was no charging observed in the previous measurement, any changes in the kinetic energy distribution of the photoelectrons are entirely accounted to changes in the XUV spectrum due to changes in the conditions of harmonic generation. As can be seen from figure 7.7, the central energy of the XUV spectrum shifts by more than 300 meV to higher energies with the increase of the pump pulse energy. A blue shift of similar magnitude induced by the application of high IR pump intensities has been observed before in HHG experiments [30].

Finally, a series of photoelectron spectra on a sodium iodide solution with a concentration of 6 M is conducted with varied XUV photon flux. To compare the changes in the photoelectron spectra of the solution to the changes observed in the gas, the results are shown together in figure 7.7. The central energies of the water $1b_1$orbital and the iodide $5p^2P_{3/2}$ orbital experience a blue shift that is comparable to the shift observed in the study on argon.

It is therefore concluded that ionization-induced charging is negligible in steady state XUV PES experiments on liquids under the present experimental conditions.

7.6.2. Evaluation routine

For each sample with a certain halide concentration, a series of 50 photoelectron spectra was recorded, with a duration of one minute for each spectrum. The photoelectron signals of individual spectra of a series were then added, a Shirley-type background [117] was subtracted from the sum and the results were normalized to the height of the $1b_1$ liquid peak. Dividing the series into individual measurements allowed to preserve the acquired data in the case of an interruption of the experiment, e.g. due to a frozen jet. The binding energy scale of the normalized spectrum of each halide concentration was calibrated according to the photon energy of the XUV radiation, which was periodically inferred from PES experiments on argon conducted during the study. To account for the streaming potential of the liquid jet, the binding energy scale was further adjusted in order to match the binding energy of the $1b_1$ gaseous peak with its literature value of 12.62 eV [100].

The photoelectron spectra for each concentration were then evaluated in two steps. First, a sum of Gaussian functions was fitted to the data in order to determine the contributions of the water orbitals to the photoelectron signal. These contributions include photoelectrons originating from molecules in the gas phase, and from molecules in the liquid phase. For the gas phase molecules, the photoelectron signals of the $1b_1$ orbital and its two vibrational states, of the $3a_1$ orbital, and

of the $2a_1$ orbital, were taken into account. The signal from molecules in the liquid phase arises from photoelectrons originating from the $1b_1$ orbital, the two $3a_1$ orbitals, and the $1b_2$ orbital. The fit function employs a modified Gaussian function to reproduce the photoelectron signal of the $1b_1$ orbital of liquid water. This is necessary because a Gaussian function, which describes well the shape of the liquid $1b_1$ photoelectron peak regarding the central energy, amplitude, and width of the peak, carries too much spectral weight in the adjacent spectral regions. This would disturb the evaluation of the much weaker photoelectron signal of the halide ions, especially in the case of low concentrations. Therefore, a Gaussian-like function of the form:

$$f(E) = A\ e^{-\frac{1}{2}\left(\frac{E-E_0}{\sigma}\right)^p} \tag{7.5}$$

is used to model the $1b_1$ orbital of liquid water instead. Here, A represents the amplitude, E_0 is the central energy and σ is the width of the Gaussian-like peak. The parameter p allows to adjust the shape of the peak. For values of p lager than two, the function carries less spectral weight in the adjacent spectral regions, thus allowing to determine the halide contribution. In the course of the evaluation, a value of $p \approx 2.3$ is used.

In the second step of the evaluation, the result of the multi-Gaussian fit of the water spectrum was subtracted from the data, producing a photoelectron spectrum of the halide ions which is free from the water contribution. This is especially useful in the case of low halide concentrations and for the study of mixed solutions, where the photoelectron peak of the chloride 3p orbital overlaps with the peak originating from the liquid water $1b_1$ orbital.

7.6.3. Photoemission from aqueous NaI solutions

Figure 7.8 depicts an exemplary photoelectron spectrum acquired for the case of a NaI solution with a concentration of 6 M. The photoelectron signal up to a binding energy of ≈ 19 eV, represented by the black circles, consists of contributions from the dissolved iodide ions, from the water molecules in the liquid phase and from gaseous water molecules. The aqueous sodium ions exhibit a binding energy of 38 eV [104], and therefore are not included in the probed spectral range. The graph of the multi-Gaussian fit function, accounting for the water contributions, is fitted to the data, and is represented by the solid red line in panel (a).

Panel (b) illustrates the photoelectron signal of the iodide ions in the water-background-subtracted spectrum, shown by the black circles. In the spectra of samples with a high NaI concentration, a prominent double-peak structure of the photoelectron signal of the iodide ions is apparent. This structure arises from the two spin-orbit states of the residual iodine atom, namely the $5p^2P_{3/2}$, and the $5p^2P_{3/2}$ state. The double peak is well reproduced by a sum of two Gaussian functions. The graph of this fit is depicted by the solid red line. The individual contributions associated with the spin-orbit states of the iodine atom are indicated by the dashed green line and the dotted orange line, respectively.

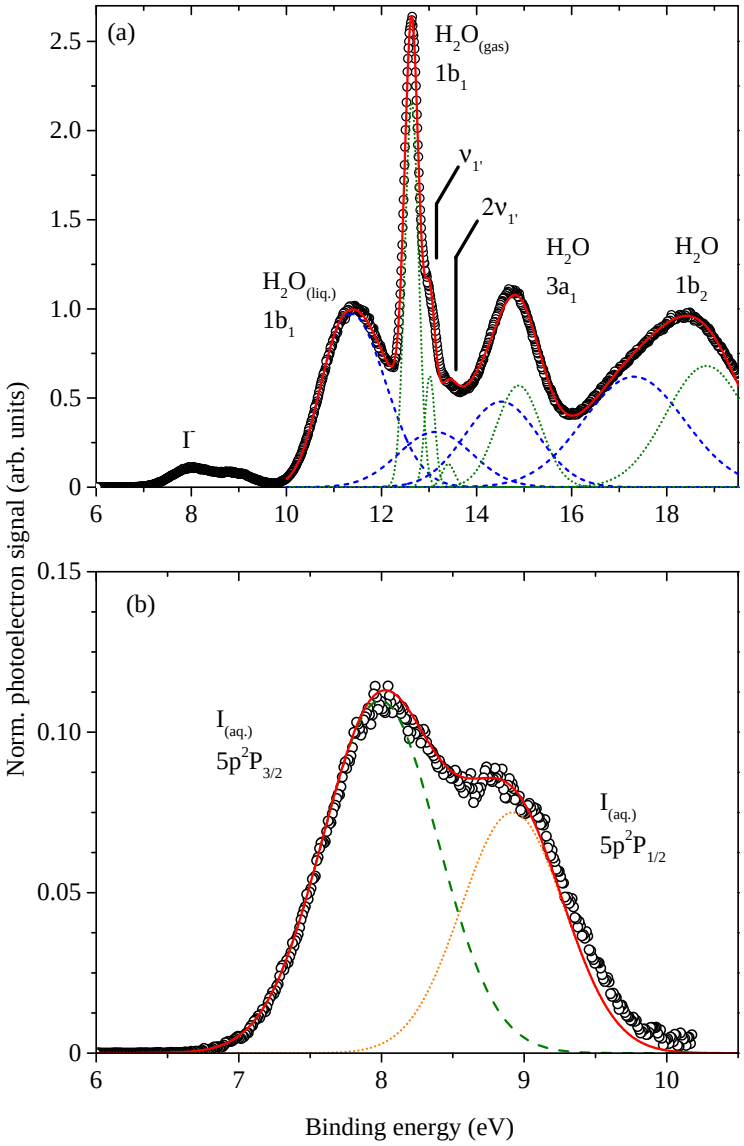

Figure 7.8.: XUV photoelectron spectrum of an aqueous NaI solution. Panel (a) depicts the normalized photoelectron signal of a solution of 6 M concentration (circles). The graph of a fit function taking the liquid and gaseous contributions of water into account is depicted by the solid red line. The fit function is a sum of Gaussian functions. The individual contributions of the gaseous molecules are indicated by the dotted green lines, while the contributions of the liquid phase are represented by the dashed blue lines. Panel (b) depicts the contributions of iodide (dashed green and dotted orange) to the photoelectron signal.

Ionization yield of iodide in aqueous NaI solutions

In the water-background-subtracted photoelectron spectrum (see panel (b) of figure 7.8), the photoelectron signal of the two spin-obit states of the residual iodine atom are fitted by a sum of two Gaussian functions. The area under these functions is then used as the ionization yield from the iodide ion. Figure 7.9 depicts this ionization yield as a function of the iodide concentration by the blue triangles. In the full range of concentrations between 100 mM and 6 M of NaI applied in this study, the ionization yield from the iodide ions is proportional to the sodium iodide concentration. No enhancement of the ionization yield of iodide is apparent from the data. The non-uniform distribution of the iodide ions in the interfacial region of water along the direction perpendicular to the surface, with a high ion density just below the interface, has been reported from MD simulations in numerous articles [75, 78, 83, 118–120]. The linear dependency of the ionization

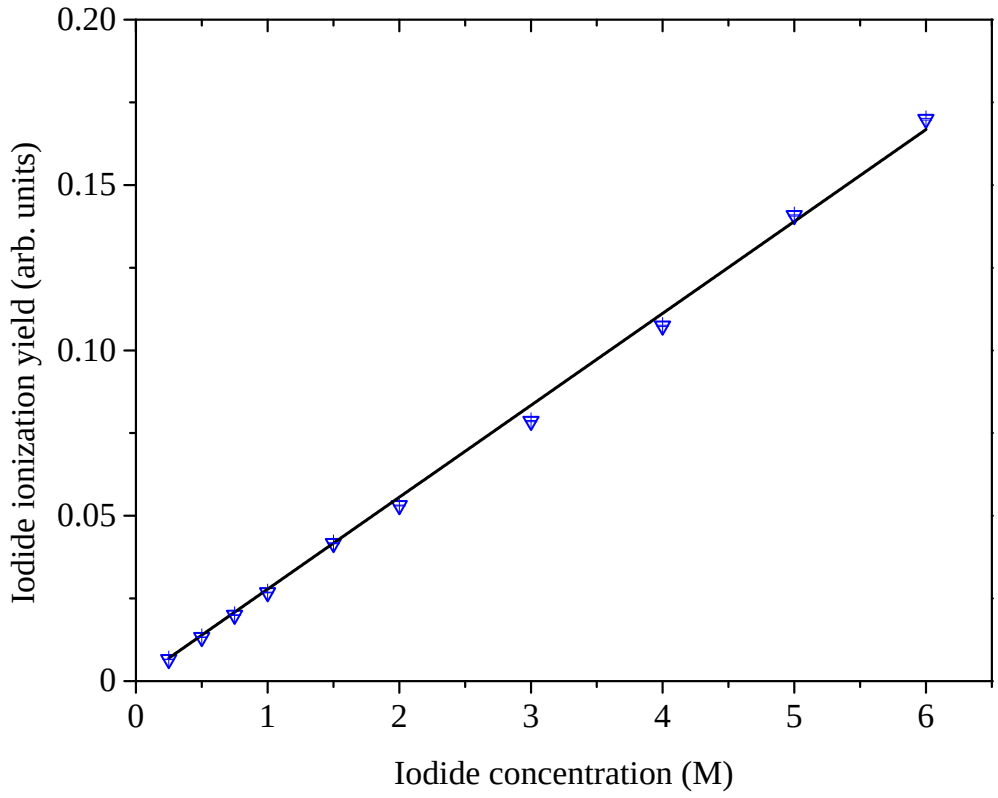

Figure 7.9.: Ionization yield (integrated photoelectron signal) of iodide as a function of NaI concentration (blue triangles). The solid black line represents a linear fit to the data.

yield observed in the present experiment might as well indicate that, although the water surface incorporates an enhanced number of iodide ions, the ratio of surface and bulk ions remains constant upon a change of salt concentration. However,

this explanation is not supported by MD simulations of aqueous NaI solutions of different concentrations. In contrast, it is reported that an aqueous NaI solution with a concentration of 2.1 M exhibits a smaller surface-to-bulk ratio of iodide ions than a solution with a concentration of 1.1 M [119]. The decreasing surface-to-bulk ration of iodide ions with an increase of the ion concentration has been previously observed in a photoelectron spectroscopic study conducted with the use of synchrotron radiation [93]. There, the ionization yield of iodide clearly deviates from a linear dependency to smaller increments in the limit of high sodium iodide concentrations.

The difference between the concentration dependencies of the ionization yield in the present study and in ref. [93] arises from the different experimental conditions applied. In the latter study, soft X-ray radiation with a photon energy of 100 eV from a synchrotron facility was used to produce photoelectrons from the water valence shell, and from a number of iodide states. Eventually, the photoelectron yield of the iodide 4d orbital was evaluated, in contrast to the investigation of the iodide 5p orbital in the present work. Additionally, the probe light polarization was different with the direction of polarization parallel to the liquid jet in ref. [93], and perpendicular in the present work. The choice of iodide orbital and direction of polarization may result in different angular photoemission characteristics. The relevant photoelectrons exhibited a kinetic energy of ≈ 45 eV in the synchrotron study, in contrast to a kinetic energy of ≈ 23 eV in the present case.

Both results can also be brought into agreement with each other, and with the MD simulations, if different EALs are assumed for the two experiments. As it is discussed in section 7.3.2, the escape depth of photoelectrons of low kinetic energies in PES experiments with liquid samples is under debate. The EAL might be successively decreasing below one nanometer for electrons with a kinetic energy of less than 70 eV, as reported by Thürmer *et.al.* [97] or it remains approximately constant at a value in the order of one nanometer, as reported by Suzuki *et.al.* [98]. At this point, from the linear dependency of the ionization yield in figure 7.9, it is concluded that the EAL, and therefore the probing depth in the present experiment, is sufficiently large to cover the interfacial region of non-uniform iodide ion density, together with a part of the bulk region exhibiting uniform ion density. Whereas in ref. [93], the EAL appears to be sufficiently small to restrict the probing depth to the surface region of enhanced iodide density only, which saturates for high salt concentrations.

The conclusion that the EAL is sufficiently large to probe also the bulk region of constant ion concentration allows a comparison between the length scale reported in the MD simulations in refs [75, 119], and the probing depth in the present experiment. Typically, the region of non-uniform ion density extends to more than 1 nm into the bulk of water in the simulations [76, 83, 119]. Since the probing depth under the present conditions is larger than the thickness of the non-uniform interfacial region, it is also larger than one nanometer. This agrees well with the result and error margin reported in ref [98].

Interestingly, also the ionization yield of Na^+ ions deviates from a linear depen-

dency for high concentrations in the study from ref [93]. This is also consistent with the results from MD simulations and indicates that the probing depth extends to the subsurface region of enhanced Na^+ density. Comparing this to the length scale reported in the MD simulations, the EAL of electrons exhibiting a kinetic energy of 45 eV has to be at least 0.5 nm, but not much larger than 1 nm.

VBE of the water $1b_1$ orbital and of the aqueous iodide 5p orbital depending on NaI concentration

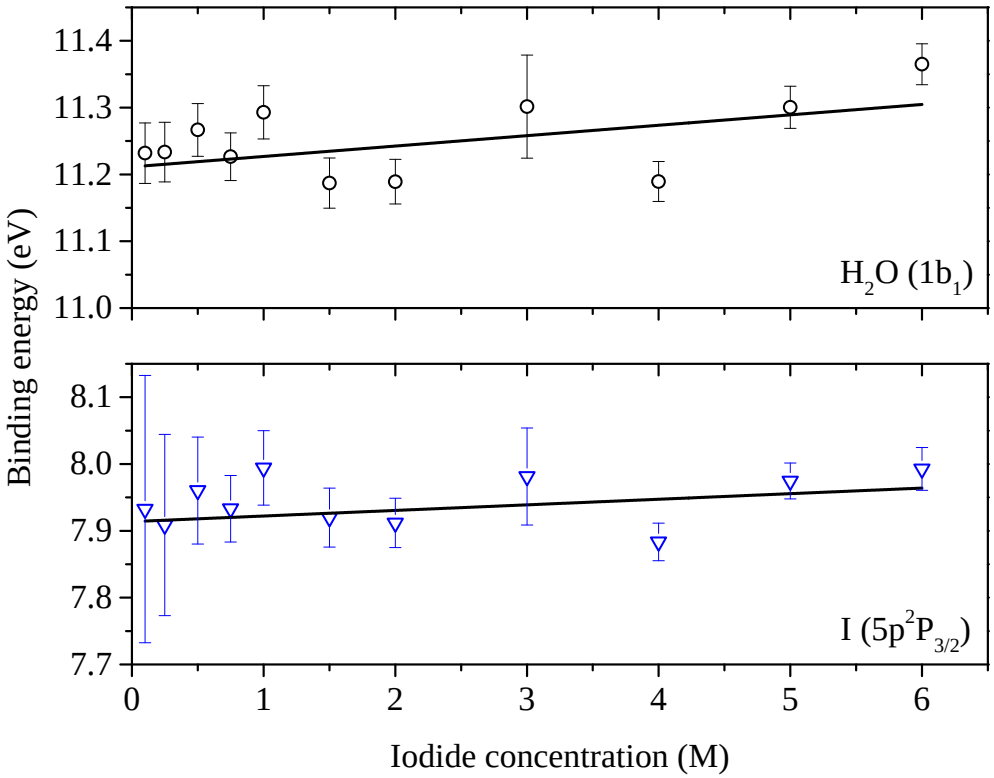

Figure 7.10.: VBE of the liquid water $1b_1$ orbital, and of the aqueous iodide 5p orbital depending on NaI concentration. Both binding energies show a small increase with the increase of the salt content.

The dependency of the VBE of the liquid water $1b_1$ orbital and the valence orbital of iodide on the NaI concentration is extracted from the fits. The result is shown in figure 7.10. The upper panel of the figure displays the dependency of the liquid $1b_1$ orbital on the salt concentration, while the lower panel displays the dependency of the $I(5p^2P_{3/2})$ iodide peak on the salt concentration. Linear fits to the data indicate the tendency of a slight increase of the VBE of both spectral contributions with an increase of the salt concentration. In both cases the linear increment is small, 15.6 ± 8 and 8.4 ± 7 meV/M, respectively, with larger error

bars because of the scatter of the data points. Over the range of investigated NaI concentrations, the increment of 8.4 meV/M leads to a binding energy increase of ≈ 50 meV for the photoelectron peak associated with the I($5p^2P_{3/2}$) ionization channel. An increase of the halide binding energy by 100 meV for ions in the vicinity of the surface has been predicted from MD simulations [76]. The present result is in the order of the theoretical prediction. In this interpretation, it has to be kept in mind that the method of photoelectron spectroscopy is an integrating technique that averages the electronic properties over the range of the EAL of the photoelectrons of a specific kinetic energy. Since the results presented in the previous section indicate that at least some part of the bulk solution is probed under the present conditions, it is not possible to distinguish between ionic species located in the bulk and surface regions.

At this point, it is possible to compare the presented results to those reported by Hiranuma *et.al.* in their single pulse pump-probe experiment [99]. There, the appearance of a second spectral band associated to changes in the electronic structure of iodide in the interfacial region was reported with increased NaI concentration. This second band is shifted to lower binding energies by ≈ 550 meV compared to the photoelectron yield at low NaI concentrations. The present results on the ground-state ionization of the iodide ion reveal that this second band is caused to a large extend by a change in the energy of the CTTS band with an increased iodide concentration.

Spectral width of the water $1b_1$ orbital depending on NaI concentration

In the present experiments, the spectral width of the liquid water $1b_1$ orbital was found to decrease with an increase of the NaI concentration. The result is displayed in figure 7.11. With an extrapolated value of ≈ 1.52 eV, the spectral width of pure water is slightly larger than reported in other studies [90, 95]. At the largest concentration of 6 M, the spectral width decreases to a value of 1.45 eV. This difference of 70 meV over the range of applied concentrations cannot be explained by changes in the spectral width of the HHG light. The XUV spectrum was routinely tested on argon gas and the FWHM of the spectrum was always in the order of 150 meV. A change of the FWHM of the XUV spectrum by nearly 50 % would also affect the appearance of the $1b_1$ peak of water gas in the photoelectron spectrum, which is not the case in the present study. Furthermore, a similar change of the FWHM of the iodide ionization peaks was not observed. Therefore, the narrowing of the $1b_1$ peak of liquid water has to be associated with changes in the electronic structure of the salt solutions. Since the FWHM of the $1b_1$ peak of liquid water, with a value of 1.45 eV, remains large compared to that of gaseous water, the changes induced by the increase of the iodide concentration are minor. Generally, the broadening of photoionization peaks in liquids compared to the gaseous species is explained by a variety in structural environments leading to more or less pronounced changes in the molecular orbitals. The superposition of the photoelectron signals from the stronger and from the less affected molecules leads to the broadening of features in photoelectron spectra [90, 91, 107]. The

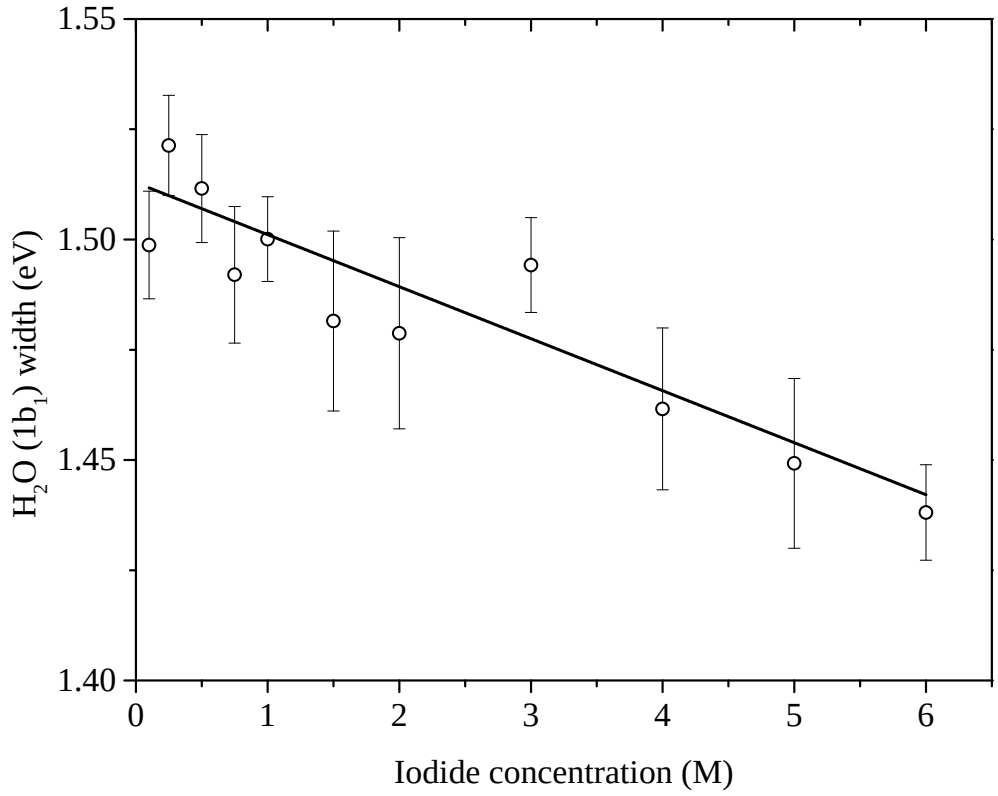

Figure 7.11.: Spectral width of the liquid water $1b_1$ orbital depending on the NaI concentration. A decrease of about 70 meV is apparent upon an increase of the salt concentration to a value of 6 M.

narrowing of the liquid $1b_1$ peak can be explained by a reduction of the number of possible structural environments for the water molecule in aqueous salt solutions with increased concentration compared to the pure solvent. At this point it remains open why the non-bonding $1b_1$ orbital, which stands vertical on the molecular plane, is affected so strongly by possible changes in the H-bonding network.

7.6.4. Photoemission from mixtures of aqueous NaI and NaCl solutions

Figure 7.12 depicts the photoelectron signal acquired for a mixed aqueous solution with a concentration of 4 M NaCl and 0.5 M NaI. The data are indicated by black circles, and the fit of the water-dominated part of the spectrum is indicated by the red line. The individual contributions from liquid and gaseous water are depicted by blue dashed, and green dotted lines, respectively. In general, the shape of the signal from photoelectrons with binding energies between 6 and 19 eV is very similar to the study of NaI solutions. The difference consists in the additional contribution of photoelectrons ionized from the 3p orbital of the chloride ion, which

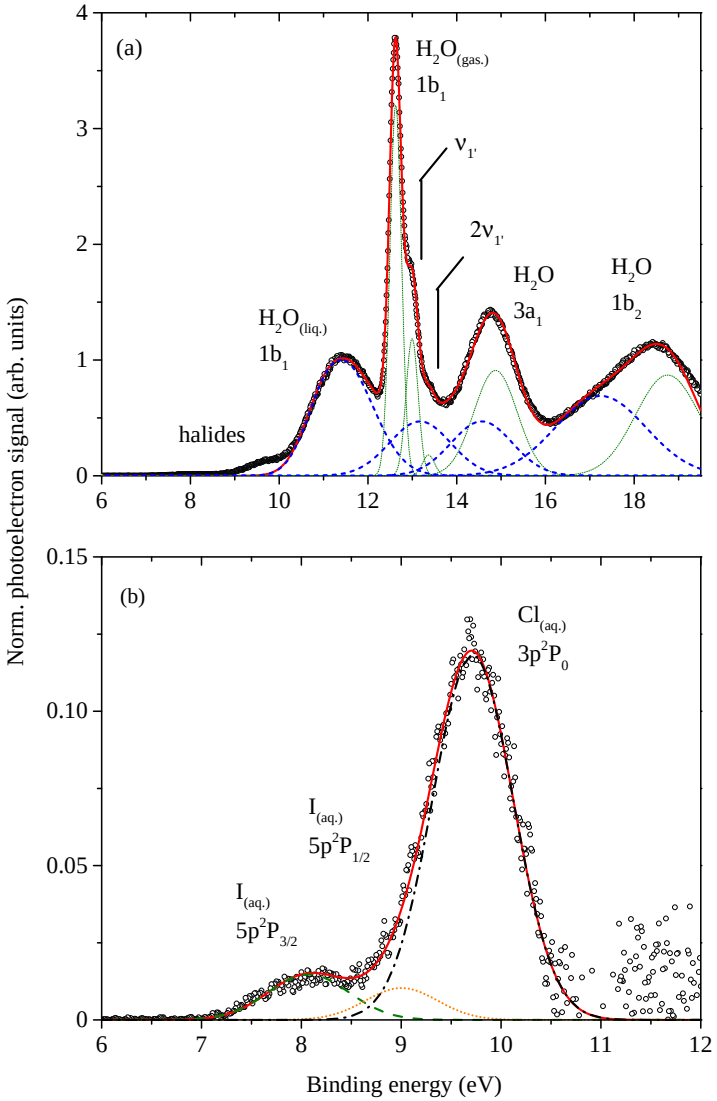

Figure 7.12.: XUV photoelectron spectrum of a mixed aqueous solution. Panel (a) depicts the normalized photoelectron signal of a mixed solution containing 0.5 M NaI and 4 M NaCl (circles). The graph of a fit function taking the liquid and gaseous contributions of water into account is depicted by the solid red line. The fit function is a sum of Gaussian functions. The individual contributions of the gaseous molecules are indicated by the dotted green lines, while the contributions of the liquid phase are represented by the dashed blue lines. Panel (b) displays the contributions from iodide (dashed green and dotted orange) and chloride (black dash-dotted) to the photoelectron signal.

gives rise to a prominent shoulder at the low energy side of the peak originating from the liquid water $1b_1$ orbital.

The inset in figure 7.12 illustrates the photoelectron signal of the halide ions in the background-subtracted spectrum (black circles). Due to the strong overlap of the signals of chloride and water, it is even more important to follow the procedure of evaluating the spectra in consecutive steps, i.e. first fitting of the water contribution, and then subtracting it from the spectra before evaluating the halide contributions. The graph of the sum of three Gaussian functions, shown in the inset, reproduces the halide-dominated part of the spectrum, and is depicted by the red line. The three Gaussian contributions are represented by the green dashed and orange dotted lines associated to the two iodine spin-orbit splitting states, and the black dash-dotted line represents photoelectron signal of the chloride ion. As it is the case in ref. [95], a spin-orbit splitting of the 3p orbital of the residual chlorine atom is not observed.

Ionization yield of the halide ions in mixed aqueous solutions

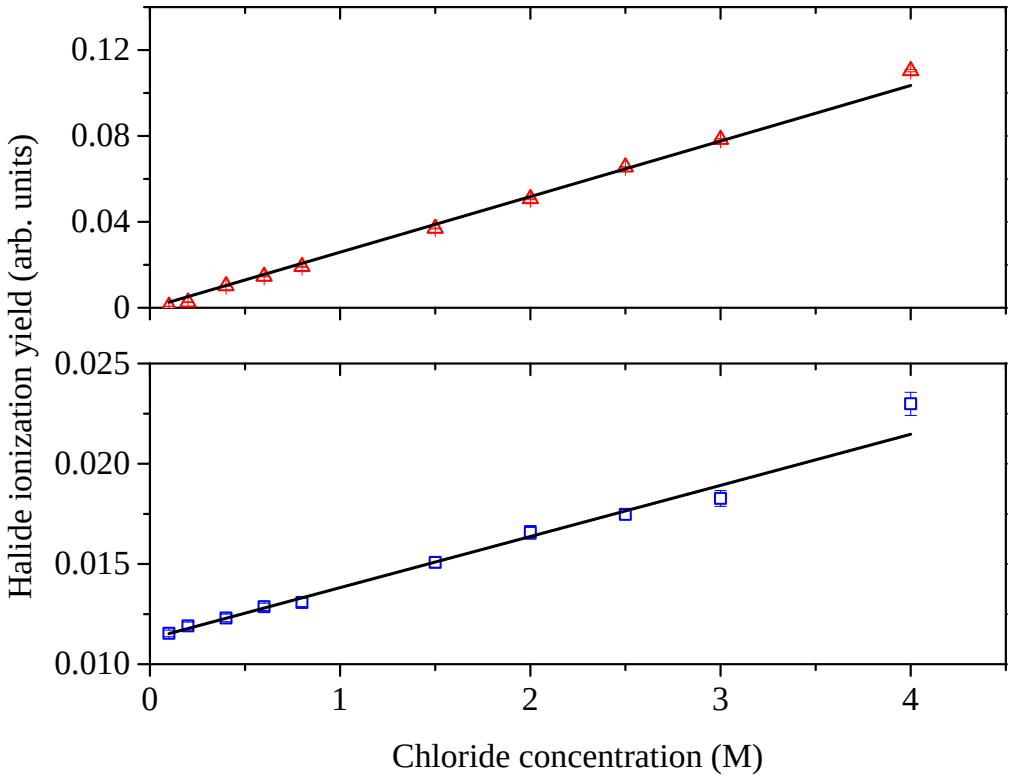

Figure 7.13.: Ionization yield of iodide and chloride as a function of NaCl concentration. The concentration of NaI is kept constant at 0.5 M.

Similar to the study on aqueous NaI solutions, the integral of the Gaussian fit functions is evaluated as the ionization yield of iodide and chloride ions in the study of mixed aqueous halide solutions. The result is depicted in figure 7.13. The upper panel illustrates a linear relation between the chloride concentration and the ionization yield from the 3p orbital of the Cl^- ion. The same argumentation that was used in the case of the iodide yield in the study of aqueous NaI solutions is applicable here. From MD simulations, chloride is predicted to be enhanced at the surfaces, albeit to a lower degree than iodide, and at a slightly larger distance from the surface into the bulk. Also the surface-to-bulk ratio of chloride ions is reduced with increased chloride concentration [119]. The linear trend in the data is well explained with the argument of a large enough EAL, that enables to probe the surface region together with parts of the bulk region.

Interestingly, as can be seen from the lower panel of figure 7.13, the ionization yield of iodide is not constant with an increased chloride concentration, although the iodide concentration is kept constant. The conclusion that arises from this observation is an increase of the iodide content in the surface region. This appears to contradict the statement of an EAL that is large enough to probe parts of the bulk solution. Even though the EAL might be larger than 1 nm, the increase of the ionization yield of iodide with increased chloride concentration is explained by a modification of the surface region due to the presence of an increased number of chloride ions. If the increased number density of chloride ions in the solution leads to a broadening of the non-uniform iodide density distribution towards the bulk of the solution, then the EAL is not large enough anymore to probe bulk solution.

The explanation is further supported by MD simulations of aqueous solutions containing ions of different size [83]. These simulations reveal that large ions are displaced from the bulk to the surface by the presence of smaller ions. In the case of a mixed solution containing iodide and chloride, the increased number of smaller chloride ions (R=0.181 nm) displaces the larger iodide ions (R=0.22 nm) [121] from the bulk to the interfacial region. Eventually, this leads to an elongation of the non-uniform iodide density distribution towards the bulk of the solution.

VBE of the water $1b_1$ orbital and of aqueous halide ions depending on NaCl concentration

The binding energies of the $1b_1$ orbital of liquid water, of the aqueous chloride 3p orbital, and of the aqueous iodide 5p orbital in mixed solutions are displayed in figure 7.14 as a function of the NaCl concentration. Similar to the case of pure aqueous NaI solutions, the VBE of the anions and the $1b_1$ orbital of water increase with an increased halide concentration. For mixed aqueous NaCl/NaI solutions the effect is less pronounced than for pure NaI solutions, though. Linear fits to the three data sets reveal increments of 6 ± 5 meV/M for the case of water, 9 ± 5 meV/M for the case of chloride and nearly no increase for the case of iodide. The large scatter in the data makes an interpretation of the changes in the VBE difficult, but the general trend of larger binding energies is reproduced in the two different series of measurements. Structural changes in the aqueous sodium halide solutions may

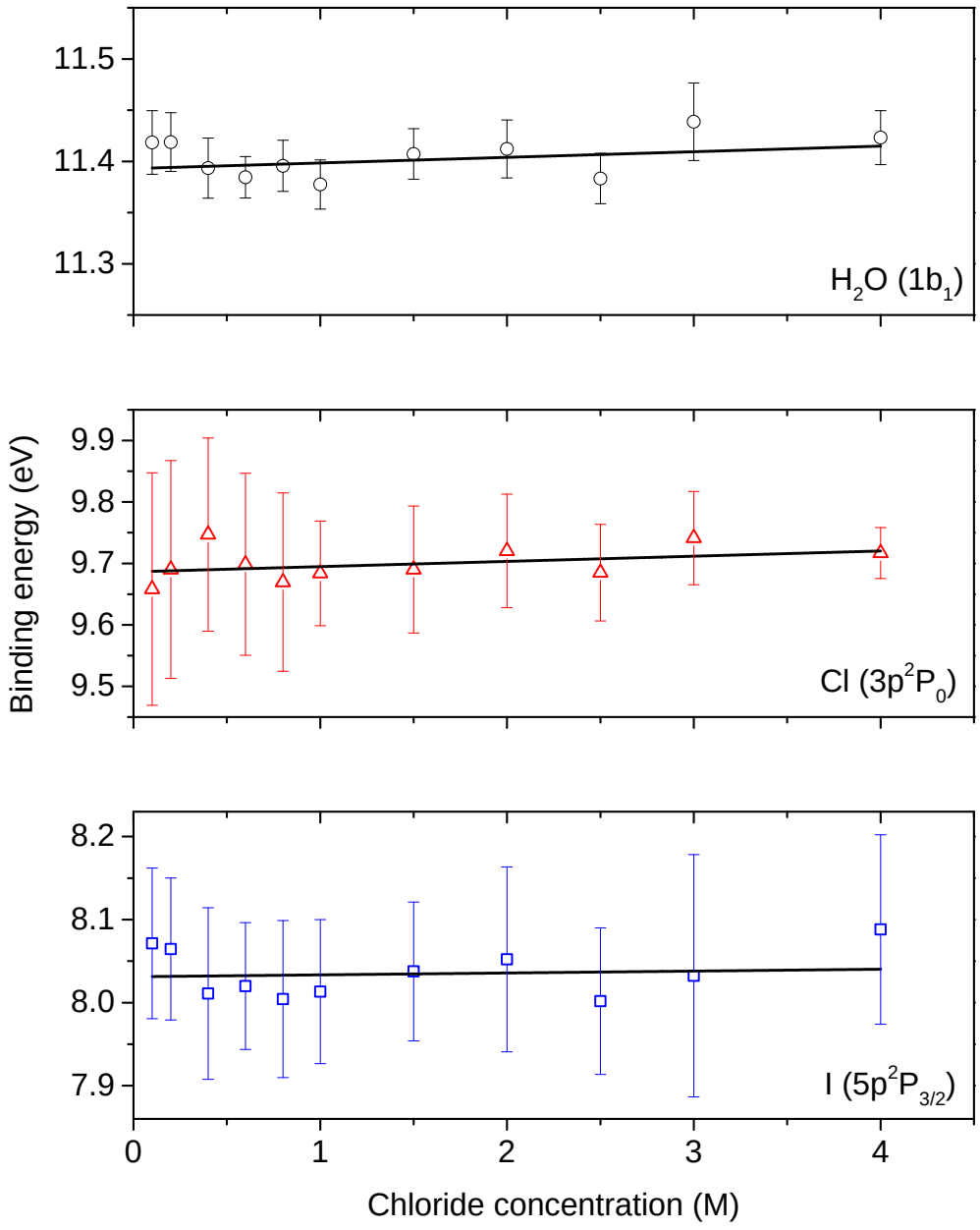

Figure 7.14.: VBE of the water $1b_1$ orbital, of chloride and of iodide ions in mixed aqueous solutions.

well be the origin to the changes in the electronic structure, but results from the present PES experiments with the use of a single wavelength have to be supported by other techniques to establish a solid picture.

Spectral width of the water $1b_1$ orbital depending on NaCl concentration

The spectral width of the photoelectron peak of the water $1b_1$ orbital in mixed NaCl/NaI solutions was investigated in the same manner as that of aqueous NaI solutions. The result is depicted in figure 7.15. Contrary to the case of aqueous NaI solutions, the FWHM of the $1b_1$ orbital remains approximately constant upon an increase of the NaCl concentration to 4 M. The constant spectral width indicates

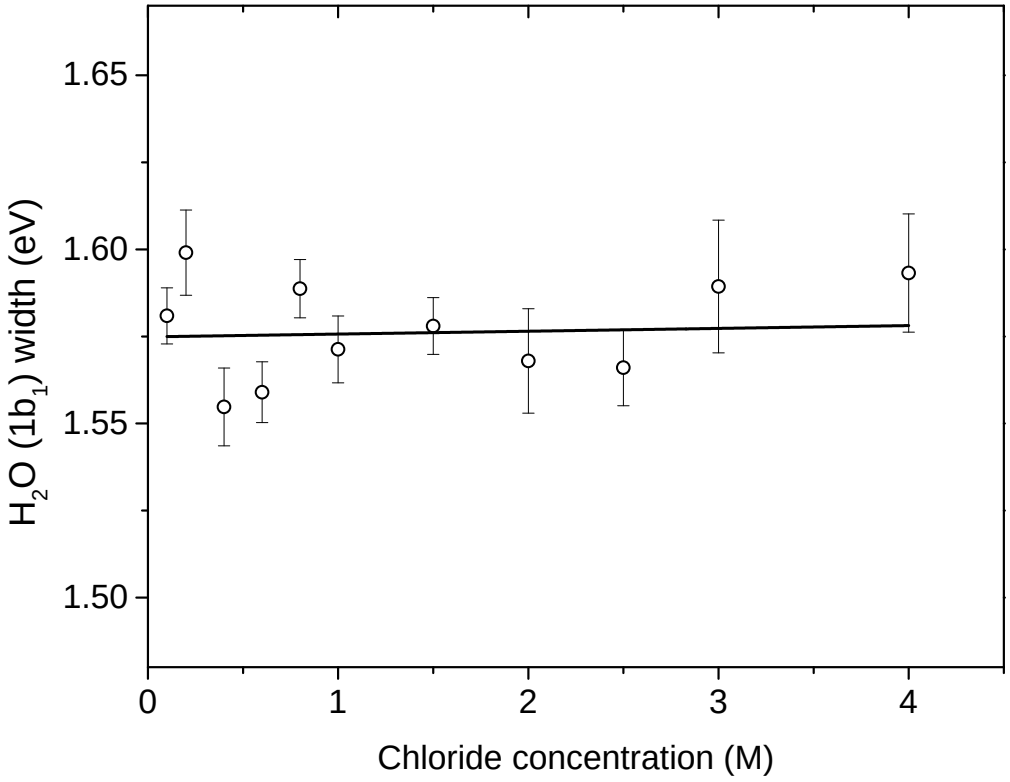

Figure 7.15.: Spectral width of the liquid water $1b_1$ orbital depending on the NaCl concentration.

that the increase of chloride ions in the aqueous halide solutions does not have the same effect as the increase of iodide ions, showed in the results presented in section 7.6.3. Since the spectral broadening is not affected by the presence of the chloride ions, the local geometrical structure of the aqueous solutions has to remain similar to that of pure water. The spectral width of the ionization contributions from the chloride and iodide ions is also not affected.

7.7. Conclusion

In this section, the setup for XUV photoelectron spectroscopy of liquids described in Part I of this work was used to investigate aqueous sodium halide solutions over a broad range of concentrations.

Results for pure NaI solutions and mixed solutions with a concentration of 500 mM of NaI and concentrations of NaCl between 100 mM and 4 M are divided into three observations. These include:

1. the linear dependency of the photoionization yield on the concentration of the halide ions,

2. the light increase of the VBE of the liquid water $1b_1$ orbital and of the aqueous the halide ions with increased halide content,

3. and the decrease of the spectral width of the photoionization peak of the liquid water $1b_1$ orbital for the case of an increased iodide content, only.

In the case of sodium iodide solutions, the photoionization yield of iodide exhibits a linear dependency on the salt concentration. This result is in contrast to a previous synchrotron study, where the iodide ionization yield grows less than linear with the increased NaI content [93]. The different experimental conditions in the present work compared to those applied in ref. [93] may explain the different results. The present findings indicate a probing depth in the PES measurements that is large enough to reach a part of the bulk solution. If this conclusion is combined with the density profiles reported from MD simulations, an EAL larger than 1 nm has to be concluded for the photoelectrons in the present experiment. This is further supported by the observed linear dependency of the chloride ionization yield in the mixed halide solutions, which is also linear dependent on the NaCl concentration. Although the iodide concentration is kept constant in this experiment, the iodide ionization yield is also increasing linearly with the NaCl concentration, indicating a displacement of iodide ions from the bulk to the surface of the solution.

In both studies, the VBE of the water $1b_1$ orbital and of the halide ions increases slightly with increased ion concentration in the solutions. The effect is smaller for the case of mixed aqueous NaI/NaCl solutions, though. Together with the observation that the spectral width of the photoionization peak of the liquid water $1b_1$ orbital decreases with increased NaI concentrations, it is concluded that the addition of sodium halide ions has a small but albeit measurable effect on the structure of the aqueous solutions. Further experiments with photon energies between that applied in the present study and that applied in ref. [93] have to be carefully carried out to evaluate these effects, together with comparisons to results from other techniques such as neutron scattering and MD simulations.

If the present setup is used for PES experiments that address the structural properties of solutions, a few improvements have to be made to the system. First of all, the scatter in the data of the binding energies has to be reduced. Most probably, fluctuations in the central wavelength of the XUV spectrum are the

origin of this error. Since the XUV spectrum is very sensitive to the conditions of the HHG process, intensity fluctuations in the driving laser and changes in the pressure of the generating gas have to be minimized. Regarding the latter issue, the setup can be improved by installing an automatic gas valve to control the gas pressure in the HHG cell instead of a manual dosing valve.

The study presented in this chapter can be developed further by installing a monochromator with an additional zone plate designed for a much larger photon energy, e.g. 100 eV. If the generation medium is exchanged to neon, then it is possible to generate HHG light with a photon energy of 100 eV. If the XUV polarization is also rotated to be parallel to the jet, results could be more easily compared to those obtained from PES experiments conducted with synchrotron radiation [93].

8. XUV photoemission spectroscopy of hemin solutions

8.1. Introduction to porphyrin solutions

In the present chapter, the capability of the HHG light source to probe the dynamics of photoexcited molecules in solution with the method of time-resolved PES is investigated for the case of hemin in DMSO.

Time-resolved PES employs the so-called pump-probe scheme, where one light pulse excites electrons in the sample, while a second light pulse probes the partially occupied electronic sates of the excited sample. The two pulses are synchronized in the time domain, and the variation of their time delay allows to study the temporal evolution of the electronic excitation. In the case of a purely laser based setup, the two light pulses are intrinsically synchronized, as it is realized in the present study. Compared to other methods for time-dependent studies, such as transient absorption spectroscopy or photoluminescence spectroscopy, time-resolved PES allows not only the measurement of the time constants of electronic excitations, but also the determination of their absolute binding energies. Additionally, it also allows to trace radiationless decay paths, which is not possible in experiments employing photoluminescence spectroscopy.

Hemin, or Fe (III) protoporphyrin IX chloride, is an aromatic molecule which belongs to a large family of molecules named porphyrins. These organic molecules share the same aromatic ring structure, and play a key role as active sites in a variety of natural complexes such as proteins, vitamins, and chlorophylls. In addition to the natural molecules, artificial porphyrins act as functional sites in a multitude of applications. These include photosensitizers for dye-sensitized solar cells (DSSCs) [122–124], artificial photosynthesis [125], photodynamic therapy [126, 127] and optical sensors [128, 129].

Porphyrins exhibit strong absorption in the UV, and visible (VIS) region of the electromagnetic spectrum, which is often the key to their application, and which makes them ideal case studies for time-resolved PES. Additionally, many biological processes occur in solutions, so that the study of molecular properties in liquid environments is of great importance. The hemin molecule chosen in the present study is synthesized from the heme porphyrin, which is the active site of a number of biomolecules such as hemoglobin, myoglobin, peroxidase [130] and enzymes in cytochrome.

8.2. Properties of porphyrin molecule

8.2.1. Molecular structure of porphyrins

Porphyrins represent a large group of molecules that share the same aromatic ring structure formed from carbon and nitrogen atoms. This ring structure consists of four pyrrole rings interconnected by four methin bridges. Therefore, these molecules are sometimes called tetrapyrroles. The simplest tetrapyrrole, which consists only of the aromatic ring, is the 21H,23H-porphin molecule depicted in figure 8.1. If

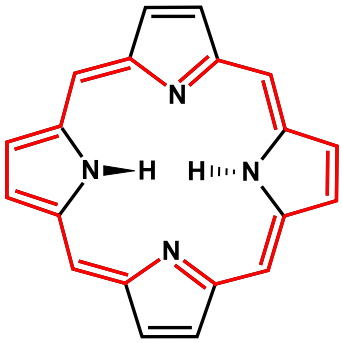

Figure 8.1.: Structural formula of the 21H,23H-porphin molecule. The conjugated π-electron system, representing the chromophore of the molecule, is indicated in red.

further organic or ionic side chains are linked to the porphin ring, the molecule is called porphyrin. The pi-electron system of the porphin ring is depicted in red. It is this pi-electron system that determines the optical absorption of porphin and porphyrins and therefore gives rise their deep red-brown color (see section 8.5.1). The particular choice of side chains connected to the ring determine the physical behavior of the molecule, e.g. water soluble porphyrins carry ionic side chains, while those porphyrins with purely organic side chains are barely soluble in water. Furthermore, side chains are used to embed porphyrins in proteins or to link them to other molecules in supermolecular assemblies They are also used to attach porphyrins to surfaces in DSSCs or sensor applications. If the side chains are aromatic themselves and change the conjugated ring system, then the molecule is called a "porphyrinoid".

The center of the porphyrin molecule can be occupied by two hydrogen atoms or by a metal ion. In the former case, the molecule is called the free base, while in the latter case it is called metalloporphyrin. Natural porphyrins are metalloporphyrins, and often incorporate transition metal ions, e.g. hemoglobin and myoglobin carry a Fe(II)-ion, while the molecular center in vitamin B_{12} is occupied by a Co^{+}-ion. In the case of small metal ions (ionic radius < 75 pm), the porphin ring of metalloporphyrins is a flat structure, while larger ions stand out of the molecular plane and distort the ring [131].

Metalloporphyrins may bind one or two axial ligands to the metal ion. This ability is a very important property of natural porphyrins, e.g. the heme group

binds oxygen as axial ligand which is the key function for oxygen transport in humans and animals.

Molecular structure of Fe(III) protoporphyrin IX chloride (hemin)

The molecule investigated in the present work is the Fe(III) protoporphyrin IX chloride, commonly called hemin. Protoporphyrin IX is a naturally abundant porphyrin, that occurs in the proteins hemoglobin, myoglobin, and in the enzymes catalase and cytochrome c. In the case of hemin, the protoporphyrin IX incorporates a ferric iron ion (Fe^{3+}), to which an axial chloride ligand is attached. Its 3D model, and its structural formula are depicted in the figures below.

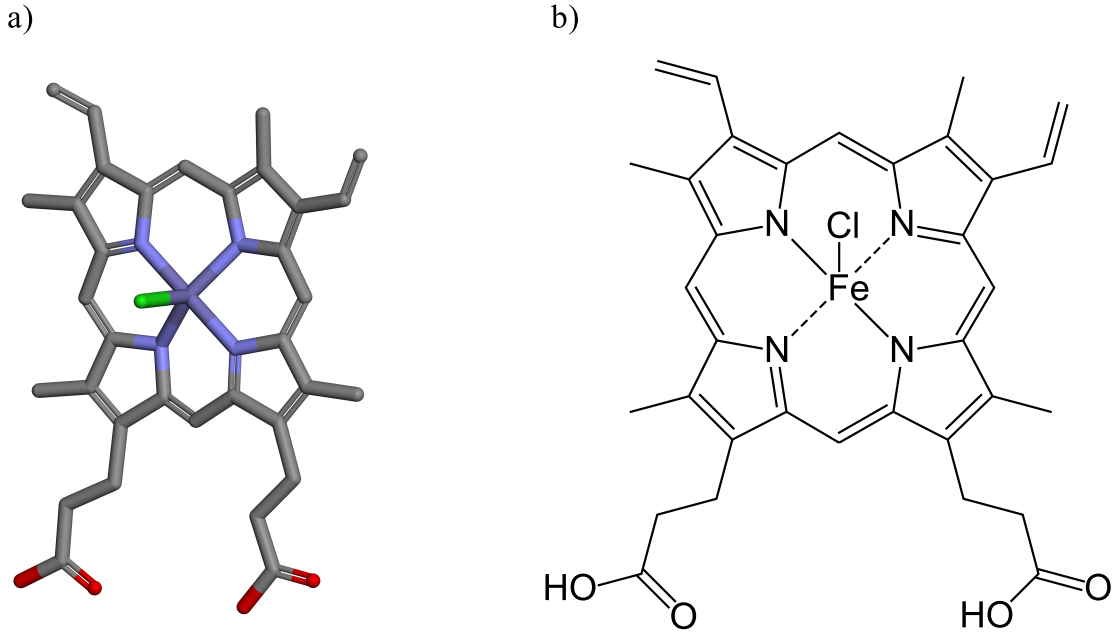

Figure 8.2.: Molecular structure of hemin. Panel a) displays a 3D model of the molecular structure of hemin while panel b) displays the corresponding structural formula.

Protoporphyrin IX has two vinyl side chains, four methyl side chains and two proprionic acid side chains. Hemin resembles the natural heme molecule, which incorporates a Fe(II) ion instead, and which is the active center of the oxygen-transporting proteins hemoglobin and myoglobin in humans and animals. In hemin, the Fe(III) ion has a radius of 65 pm, and the porphyrin macrocycle is nearly flat, as can be seen from the 3D model displayed in the left panel of the previous figure. Only the axial chloride ligand pulls the Fe(III) ion slightly out of the molecular plane. In the case of heme, the Fe(II) ion is larger, in the high spin state as large as 92 pm, and thus stands further out from the porphyrin ring, which results in a ruffled structure [131]. Hemin is more stable than heme, and is therefore used in the present study as a model system for the natural molecule. Because of its organic side chains, hemin has a small solubility in water, and readily forms aggregates such

as dimers or higher order oligomers at high concentrations in aqueous environments. Since the molecular orbitals of the individual molecules in an aggregate influence each other, the existence of aggregates is visible in the UV-VIS absorption spectra of hemin solutions (see section 8.5.1).

8.2.2. Electronic structure of the porphyrin valence orbitals

The electronic structure of the porphyrin valence orbitals is largely determined by the π-electron system of the porphin ring. Deviations from this principle arise if the π-electron system is altered by aromatic side chains or by mixing of orbitals with those central metal atom. The latter case will be discussed in the present section.

Due to the similarity in their molecular structure, porphin, porphyrins an other tetrapyrroles exhibit similar structures in their UV-VIS absorption spectra. These spectra, which arise from electronic transitions from the HOMOs to the lowest unoccupied molecular orbitals (LUMOs) of the molecule, are routinely explained by the four orbital model introduced by Gouterman [132, 133]. The four orbitals involved in this model are the HOMO, and HOMO-1 π-orbitals, and the LUMO, and LUMO+1 π^*-orbitals. A scheme explaining the basic idea of this model is depicted in figure 8.3.

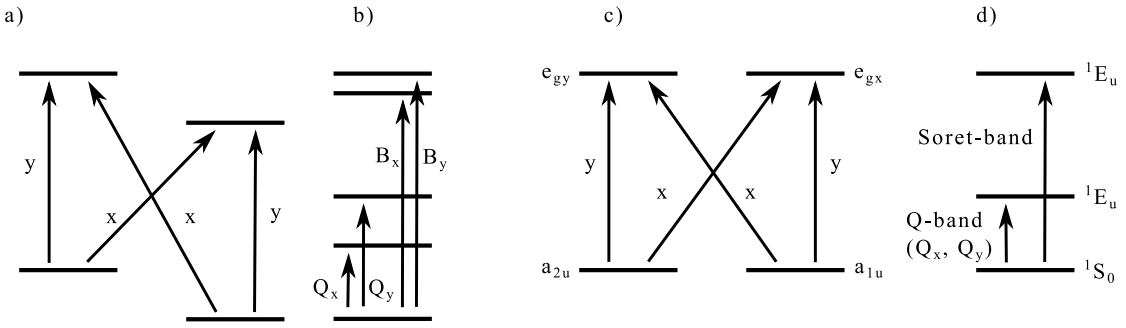

Figure 8.3.: Scheme of the four orbital model developed by Gouterman [132, 133] explaining the UV-VIS absorption spectra of tetrapyrroles. Panel a and b depict the case of a free-base molecule while the panels c and d apply for the case of a metal chelate. See text for further notations.

In the case of a metalloporphyrin, the high molecular symmetry (D_{4h} point group) leads to a near degeneration of the HOMO (a_{2u}) and HOMO-1 (a_{1u}) orbitals and a degeneration of the LUMO (e_{gx}) and LUMO+1 (e_{gy}) orbitals. The four molecular orbitals allow four electronic transitions: these are the transitions from a_{1u} to e_{gy} and from a_{2u} to e_{gx}, which are x-polarized, and the transitions from a_{1u} to e_{gx} and from a_{2u} to e_{gy}, which are y-polarized. The four transitions further mix due to configuration interaction, which results in two low energy, low intensity transitions (Q-bands Q(0,0) and Q(0,1)) and a high energy, high intensity transition (Soret-band). In the UV-VIS absorption spectra of porphyrins, the Q-bands appear

in the spectral range between $500 - 600$ nm ($2.48 - 2.07$ eV) and the Soret-band is located in the spectral range around 400 nm (3.1 eV).

The electronic structure of the metalloporphyrin valence orbitals is further influenced by the type of metal incorporated in the molecular center. In the case of metal ions which exhibit an empty d-shell, e.g. such as Mg(II), the π-orbitals forming the HOMO-1, the HOMO, the LUMO and the LUMO+1 orbitals of the conjugated ring are mostly undisturbed [134]. The same applies for metal ions which have a filled d-shell, such as Zn [135]. Metalloporphyrins that incorporate ions from one of these groups are called regular porphyrins, and show only slight shifts of absorption bands upon exchange of the metal ion [136]. They also exhibit slight changes in the intensity ratio between the Q(0,0) and Q(0,1) bands.

Porphyrins that contain transition metal ions with a partially filled d-shell, such as Fe(II) or Fe(III), experience mixing of metal d-states with porphyrin π-orbitals. As a result, the HOMO of the molecule is strongly influenced by the metal d-orbitals, while the LUMO remains determined by the π-electron system of the conjugated ring [137]. The porphyrins housing a transition metal ion are called irregular porphyrins.

In the case of free-base porphyrins, where the inner ring exhibits lower D_{2h} symmetry, the LUMO and LUMO+1 orbitals are not degenerated. The resulting UV-VIS absorption spectra of these molecules exhibits four transitions in the Q-bands.

Electronic structure of hemin

In the case of hemin, the orbitals around the HOMO-LUMO-gap of the molecule are further changed. The 3d states of the Fe(III) ion in the five-ligated state (additional axial Cl^- ligand), mix differently with the π- and π^*-orbitals of the porphyrin ring than the 3d states of the Fe(III) ion which is only ligated with the four N-atoms of the porphin ring. In contrast to the latter case, theoretical calculations performed for the model porphyrin tetraphenylporphyrin (TPP), Fe(TPP)Cl, show that the HOMO-1 orbital is a mostly ring centered A_{1u} orbital and the HOMO is an A_{2u} orbital with a small contribution of the d_z-p_{z^2} contribution from the Fe-Cl-bond [138]. Instead, the LUMO and LUMO+1 of Fe(TPP)Cl exhibit strong admixture of the Fe $3d_{xy}$ orbital and of a number of 3d-p orbitals forming the Fe-Cl-bond.

8.2.3. Deexcitation of photoexcited porphyrins

While the optical excitation of porphyrins is largely dominated by the organic macrocycle with only some modifications due to the particular central metal ion and outer substituents, the deexcitation mechanism is strongly influenced by the metal ion. Metalloporphyrins deexcite by:

- fluorescence, which occurs for metal ions such as Mg, Zn or Al,
- phosphorescence in the case of metal ions such as Pd, Pt, Ru,

- luminescence in the case of paramagnetic metals and
- radiationless decay pathways for rings housing Co, Ni, Fe(II) and Fe(III) or Ag ions [139].

Regular porphyrins show only fluorescence, while all deexcitation pathways occur for irregular porphyrins.

The ground state of the regular porphyrins is a singlet state, denoted by S_0. Absorption in the spectral region of the Q-bands leads to excitation to S_1 while the Soret-band region corresponds to a transition to the second excited state, S_2. From S_2, deexcitation occurs by rapid internal conversion, usually in the range of several 10 fs. From S_1, regular porphyrins deexcite via fluorescence with time constants in the range of picoseconds to nanoseconds with little contribution of intersystem crossing to triplet states [140].

Irregular porphyrins exhibit more deexcitation pathways, since the metal ion gives rise to higher spin states such as triplet states. The metal ion facilitates intersystem crossing to these phosphorescent states (see figure 8.4). Another deexcitation

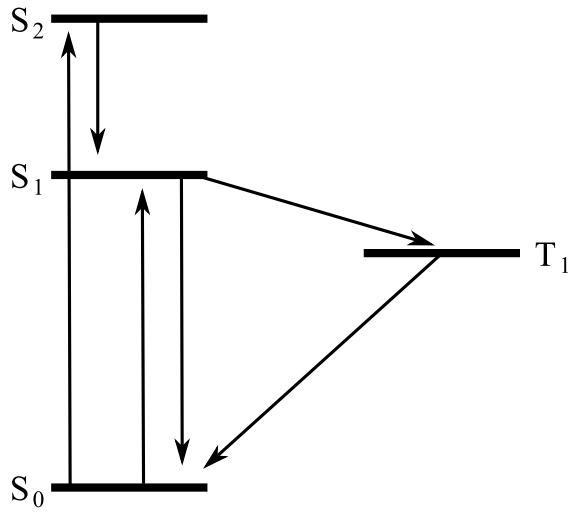

Figure 8.4.: Jablonski diagram showing the simplified energy terms of the porphyrin HOMO-LUMO transitions.

pathway in metalloporphyrins housing metal ions with partially filled d-orbitals involves ring-to-metal charge-transfer states between the porphyrin and the metal ion. The S_2 excitation centered on the porphyrin ring deexcites rapidly (< 100 fs) via such a charge-transfer state, where the excited electron is transferred to a vacant metal d-orbital [140]. In a consecutive step, the molecule further relaxes via a back donation of an electron from the metal to the ring, resulting in a localized (d,d*) state of the metal. This (d,d*) state then returns to the ground state of the molecule on a time scale of some hundred femtoseconds or picoseconds.

In the case of hemin, the relaxation steps are ultrafast processes. The lifetime of the S_2 state is only 65 fs and the back donation of an electron from the metal to the ring happens on a timescale of 250 fs[140].

8.3. Properties of porphyrins in solution

Natural porphyrins are usually poorly water soluble due to their organic side chains. To study them in liquid environments with spectroscopical methods such as PES, or nuclear magnetic resonance (NMR) spectroscopy, high molar concentrations are needed. High concentrations lead to porphyrin aggregation in aqueous environments. For these experiments, natural porphyrins are therefore either dissolved in organic solvents, or artificial, water-soluble porphyrins housing the same central metal ion as the natural molecule are used as model system.

Porphyrins exhibit a weak solvatochroism, as the transitions in absorption spectra shift by some nanometers with the change of solvent. Stronger modifications to the absorption spectra are encountered when porphyrins aggregate. In this case, the Soret-band splits, and shifts by several ten nanometers [141].

Axial ligands may detach from the metal center of the porphyrin in solution. In the case of hemin dissolved in DMSO, conductivity measurements [142] and UV-VIS spectroscopy [143, 144] support the conclusion that the chloride ligand is detached from the iron ion and replaced by one or two DMSO ligands. However, X-ray absorption measurements by Aziz *et.al.* [145] and a combined theoretical and experimental study by Atak *et.al.* [146] support the picture of a hemin molecule with the chloride ligand still being attached.

8.4. Experimental procedure

Fe(III) protoporphyrin IX chloride from bovine (purity > 90 %), DMSO (purity > 99%), and NaCl were purchased from Sigma Aldrich. All chemicals were used without further treatment. First, a 1 mM solution of NaCl in DMSO was prepared to establish a sufficiently conductive solvent for the PES experiment. It is this solution that will be referred to as "DMSO" or "the solvent" in the course of this chapter. Second, a hemin-DMSO solution with a concentration of 10 mM was prepared by dissolving the porphyrin crystals in DMSO.

Steady state absorption spectra were recorded from the hemin-DMSO solution by means of a Jenway spectrophotometer model 7315. The absorption of the Soret-band region around 400 nm was recorded with the solution contained in a fused silica cuvette with a path length of 0.01 mm, while the spectral region between 450 and 1000 nm was recorded using a cuvette with a path length of 0.1 mm. Absorption spectra of different batches exhibited the same features.

As in the case of the XUV PES study of aqueous halide solutions, the hemin-DMSO solution was injected into the vacuum system by a syringe pump supplied by Teledyne Isco (model 500D). The glass nozzle for inserting the liquid into the vacuum exhibited an orifice of 25 µm and a constant flow rate of 0.4 ml/min was used.

Photoelectrons were produced with the use of XUV light from the 21^{st} harmonic (32.55 eV) and recorded with the SPECS THEMIS 600 TOF photoelectron spectrometer. Steady state photoelectron spectra were recorded in the drift mode of the

device, which corresponds to the configuration of a traditional TOF spectrometer. The drift mode allows the highest spectral resolution of 25 meV at a photoelectron kinetic energy of 20 eV. In contrast, pump-probe measurements were recorded in the WAM of the spectrometer, in which the system of electrostatic lenses allows a higher sensitivity due to a larger collection angle of 15°.

To conduct pump-probe experiments, the part of the IR laser which is not used to drive the HHG process (see section 4.1.1) is converted to the second harmonic generation (SHG). The resulting UV light with a photon energy of 3.1 eV (400 nm) is suitable to excite the porphyrins to the S_2 excited state via the Soret-transition. The delay between the UV pump and XUV probe light is controlled by a translation stage from Newport (model FMS300CC). The stage allows a precision of 1.5 µm which results in a temporal resolution of 10 fs. Pump-probe photoelectron spectra are recorded with the THEMIS 600 spectrometer operated in the WAM, offering a higher collection angle, and therefore, a higher sensitivity to photoelectrons originating from possible transient states. To prevent the electron detector from saturation due to a high electron signal from ionization of the solvent, the detector front is kept at a bias potential of ≈ 24 V.

Pump-probe photoelectron spectra are evaluated through a routine that involves a sequence of steps. First, individual pump-probe spectra of a measurement series are shifted, and normalized to with respect to an unpumped reference spectrum. The spectral interval of the reference spectrum is chosen in a way that it is not involved in the pump-probe process. Second, the reference spectrum is subtracted from the pump-probe spectra taken at each delay stage position. The integrals of the resulting transient spectra are plotted against the time delay between the laser pulses.

8.5. Preliminary results and discussion

8.5.1. Absorption spectra of hemin in DMSO

As a prerequisite to the pump-probe PES experiments of hemin dissolved in DMSO, the steady state absorption spectrum of the hemin-DMSO solution is recorded. This allows the identification of transition energies and to determine whether molecular aggregates are present in the solution.

Figure 8.5 shows the absorption spectrum of hemin dissolved in DMSO with a concentration of 10 mM. The spectrum is dominated by a strong Soret-band at 404 nm. The two Q-bands of hemin are located at 503 nm and 628 nm. Although highly concentrated porphyrin solutions are known to result in molecular aggregates, the shown part of the spectrum corresponds to that of a typical porphyrin monomer. The Soret-band is neither red-shifted nor does it exhibit a second component, as it is observed for porphyrin oligomers in solutions near the concentration limit [147]. While large concentrations of salt also facilitate the formation of porphyrin aggregates [147], the addition of the small amount of NaCl (1 mM) does not result in obvious changes of the absorption spectrum. As can be seen from the inset in

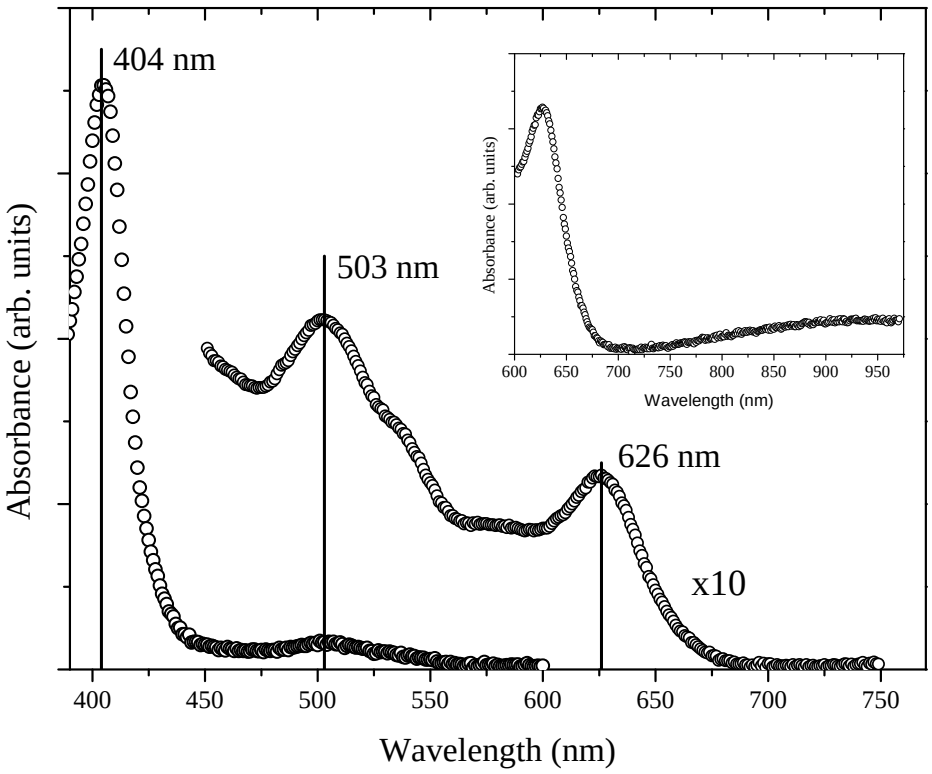

Figure 8.5.: Absorption spectrum of hemin in DMSO. The solution has a concentration of 10 mM. The measured spectrum indicates a solution free of porphyrin aggregates.

figure 8.5, the spectral region above 750 nm exhibits a weak but spectrally broad absorption band which stretches beyond 1000 nm. This feature has been observed in hemin solutions of high concentration [148] and associated to (d,d)-states similar to the case of Ni(II)-tetraphenylporphyrin. The shown absorption spectrum of a solution of hemin in DMSO with a concentration of 10 mM leads to the conclusion that the molecule is present in an undisturbed state.

8.5.2. XUV photoelectron spectrum of DMSO

Figure 8.6 shows a photoelectron spectrum of liquid DMSO, recorded from a micro-jet together with a spectrum of gaseous DMSO recorded in the vicinity of the jet. Photoelectrons are produced with use of XUV light from the 21^{st} harmonic. To acquire the spectrum of the gaseous species, the micro-jet was moved out of the XUV focus. The spectra are displayed in terms of the binding energy and the scale is corrected for the streaming potential so that the binding energy of the HOMO of the free molecule matches the literature value of 9.1 eV reported in ref. [149]. Since DMSO has a low equilibrium vapor pressure of 0.556 mbar (at 20°) [150],

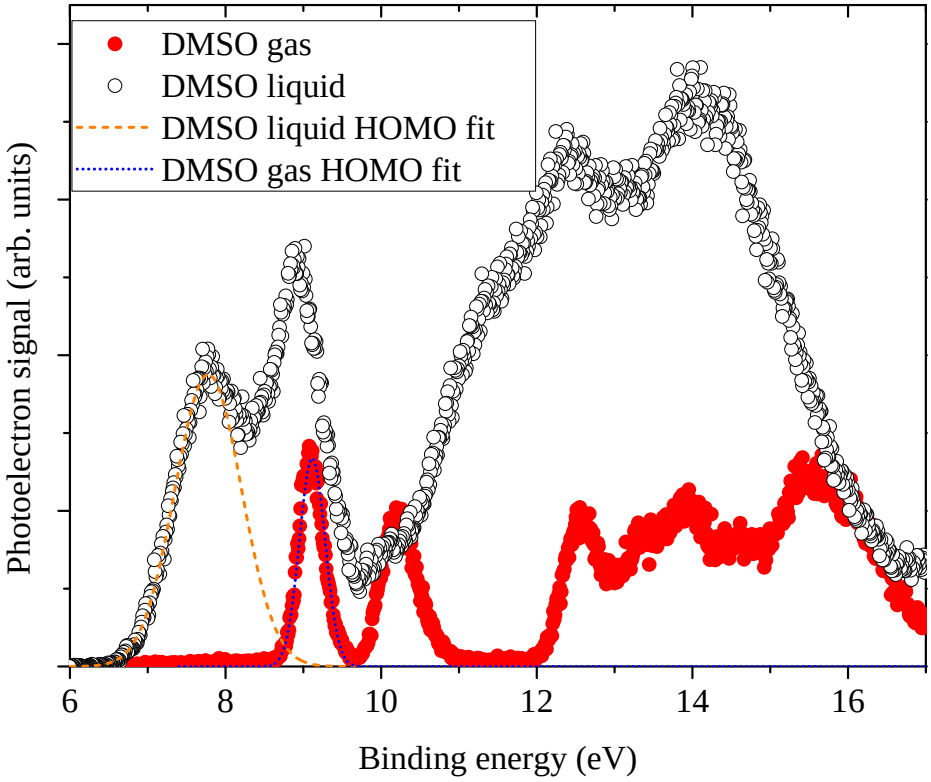

Figure 8.6.: XUV photoelectron spectrum of the valence orbitals of gaseous (red circles) and liquid (black open circles) DMSO. Graphs from Gaussian functions fitted to the data are displayed by the blue dotted and orange dashed line, respectively.

the spectrum of the liquid-jet does not show significant contributions from the gas phase. The ground state of the DMSO molecule is a X^1 A' state. The HOMO of the molecule is the 14a' orbital and the HOMO-1 is the 7a". In the spectrum of the free molecule, the photoelectron signals of both orbitals are clearly visible.

The photoelectron spectrum of liquid DMSO exhibits deviations from the spectrum of gaseous DMSO similar to those observed for liquid water described in section 7.2. Individual photoelectron peaks in the spectra recorded from the liquid-jet are shifted by ≈ 1.3 eV to lower binding energies, and are spectrally broadened.

8.5.3. XUV photoelectron spectrum of hemin-DMSO solutions

A photoelectron spectrum of hemin dissolved in DMSO with a concentration of 10 mM is displayed in figure 8.7 by the red line. For comparison, a spectrum of liquid DMSO is represented by the black line. The two spectra turn out to be similar, except that the spectrum of the hemin-DMSO solution exhibits an

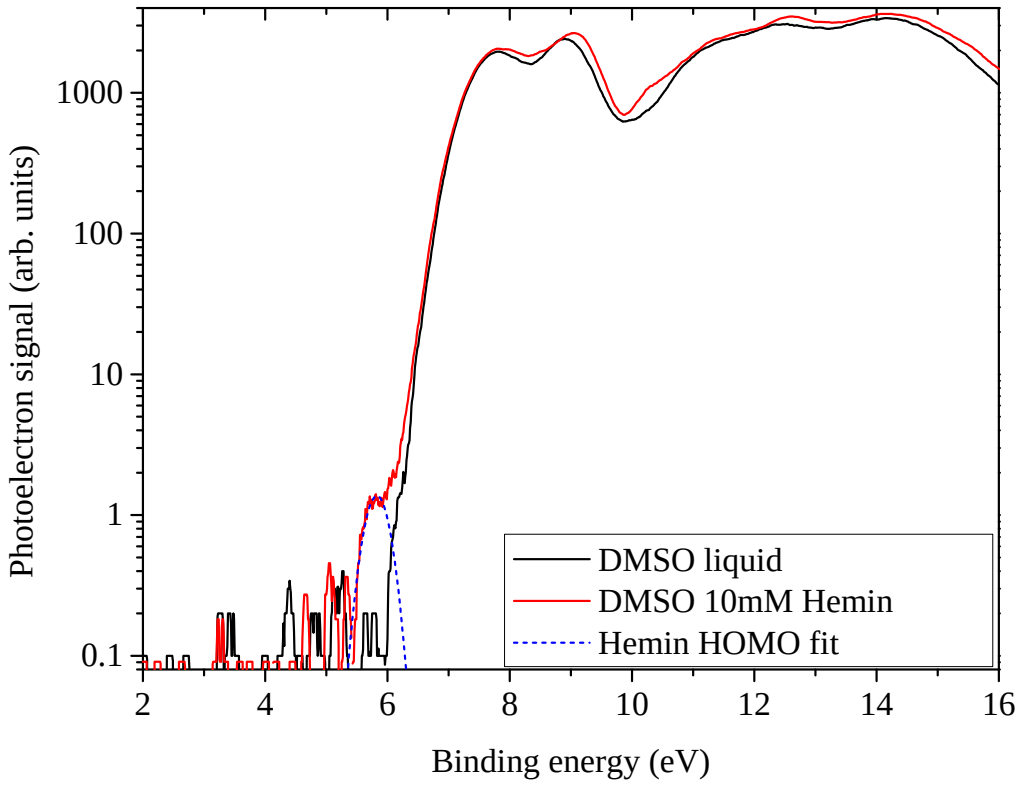

Figure 8.7.: XUV photoelectron spectrum of a hemin-DMSO solution of 10 mM concentration (red line). For comparison, a pure DMSO photoelectron spectrum is displayed (black line). The photoelectron peak from the HOMO of hemin appears as a shoulder on the DMSO signal. The graph of a fit of a Gaussian function to the hemin signal is represented by the blue dashed line.

additional feature appearing as a shoulder of lower binding energy at the flank of the photoelectron signal from the HOMO of DMSO. This additional feature in the photoelectron spectrum of the hemin-DMSO solution is formed by photoelectrons ionized from the HOMO of the porphyrin. A fit of a Gaussian function to this shoulder yields a binding energy of 5.8 eV of the dissolved hemin molecule. For a similar porphyrin, Fe(III) tetraphenylporphyrin chloride (Fe(III)TPPCl), a binding energy of 6.09 eV is reported by Nakato *et.al.* for the gaseous molecule [151]. A similar binding energy can be assumed for gaseous hemin. Therefore, a shift of ≈ 0.3 eV to lower values of the binding energy is concluded for hemin dissolved in DMSO.

The first ionization energies of porphyrins in gas phase lie around 5.9 to 6.5 eV [151–153], with the HOMO and HOMO-1 being energetically separated only by ≈ 0.5 eV. Usually, the photoelectron spectrum of the valence orbitals of gaseous porphyrin molecules is structured into three regions. Region I, which lies approx-

imately between 6 and 7 eV, incorporates photoelectron peaks from the HOMO and HOMO-1 orbitals. These two orbitals are only slightly affected by the central metal ion. The regions II and III are more affected by the metal ion and may also include photoelectrons from side groups of the molecule, e.g. the phenyl groups in tetraphenylporphyrin.

Results for the ionization potential of porphyrins and related compounds in solution are scarce. Nakato et. al. [151] report a shift to lower binding energies from measurements of the photocurrent of tetraphenylporphyrins with various metal centers dissolved in isooctane. Theoretical calculations of binding energies of chlorophyll-c2 dissolved in methanol also predict a shift of 0.2 to 0.5 eV to lower binding energies [154]. This agrees well with the finding of the present experimental study. In ref. [154], Jaramillo *et.al*, explain the shift to lower binding energies by hydrogen bonding between the chlorophyll and the solvent molecules.

8.5.4. Ionization-induced charging in pump-probe photoelectron spectra

Steady state photoelectron spectra of liquid samples acquired with the present setup have been tested for ionization-induced charging of the sample and the results are described in section 7.6.1. Space charge effects due to the ionization by the XUV probe light has been found to be negligible with the applied XUV photon flux.

Pump-probe photoelectron spectra are known to suffer from space charge effects caused by charged samples, and electron clouds in the flight region due to a high degree of ionization produced by intense pump radiation, especially if short-pulsed UV laser light is applied [114–116]. Such space charge effects have also been reported and characterized for the present setup by Al-Obaidi *et.al* [155].

To illustrate the space charge effect in pump-probe experiments of hemin-DMSO solutions, figure 8.8 displays the photoelectron yield of two measurement series acquired with different SHG pump intensities. In the following, the photoelectron yield integrated over the entire range of kinetic energies available in the WAM of the spectrometer will be called total electron yield (TEY). Figure 8.8 demonstrates that the series acquired with a higher pump intensity exhibits a large variation of the TEY, whereas the series recorded under the condition of low pump intensity shows only little variation of the yield. The sign of the variation depends on the sequence of pump and probe light pulse and their relative time delay. If the intense UV pump pulse arrives first, and strongly ionizes the sample, the resulting positively charged sample and the negatively charged cloud of electrons produced by the UV light reduce the kinetic energy of electrons ionized by the XUV probe light pulse. Thus, the amount of the fastest photoelectrons produced by XUV light appear reduced. If the two light pulses arrive at the sample coincidentally, or the XUV light pulse arrives even slightly before the UV pump pulse, the cloud of electrons produced from the intense UV light screens the effect of the positive sample and accelerates the electrons produced by the XUV light. Thus, the amount of the

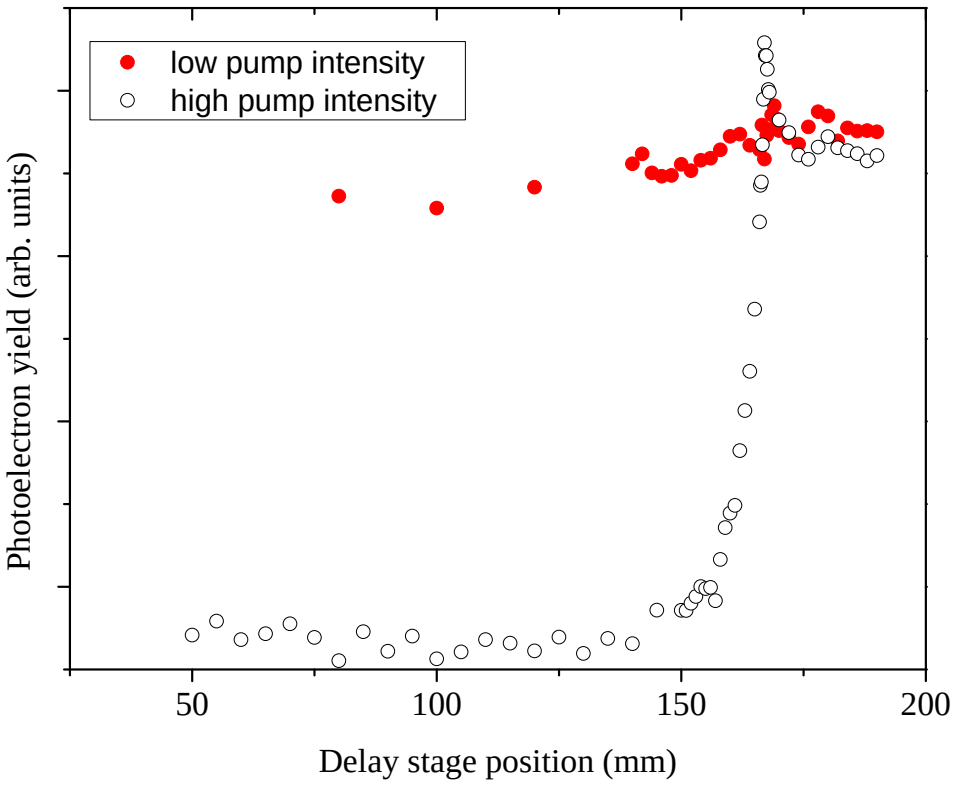

Figure 8.8.: Photoelectron yield from a pump-probe experiment of a hemin-DMSO solution. The space charge effect leads to a reduction of fast electrons due to sample ionization from the pump pulse.

fastest photoelectrons appear enhanced. If the UV pump pulse arrives much after the XUV probe pulse, the XUV photoelectron spectrum is undisturbed and the electron yield is constant.

While a space charge effect is undesirable in a pump-probe experiment, it is convenient to use it as a measure of spatial and temporal overlap between pump and probe light pulses. In the particular case displayed in figure 8.8, t_0 is close to a delay stage position of 167 mm. The fine tuning of the temporal overlap of the two light pulses can then be accomplished through a CC measurement based on the LAPE process. The particular procedure developed in our laboratory to evaluate the CC of liquid samples are described in the following section.

8.5.5. Cross-correlation on liquid samples

The setting of time zero (t_0), which marks the delay stage position at which the two light pulses overlap in time at the interaction region of the PES experiment, is an important parameter for the calibration of the time-delay scale in pump-probe experiments. This point is difficult to determine in the case of ultrashort light

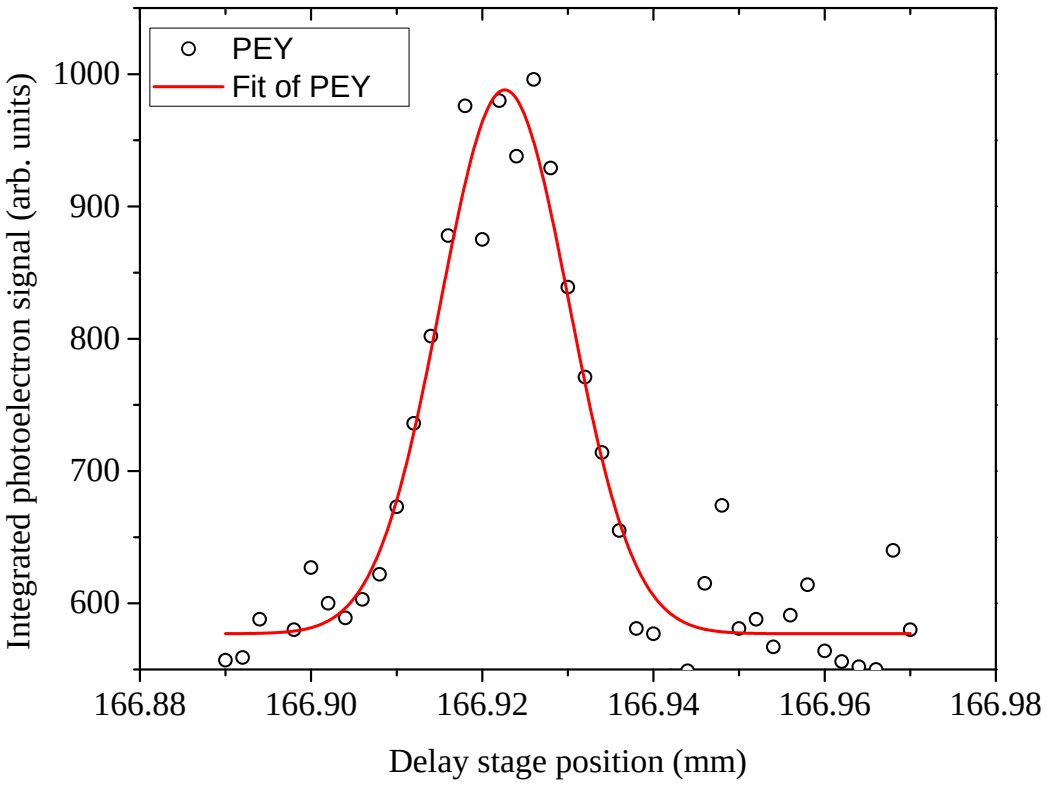

Figure 8.9.: Cross correlation between UV pump and XUV probe light performed on a hemin-DMSO solution. The CC is evaluated from the PEY of the photoelectron signal.

pulses. Biased semiconductor diodes are routinely used as a tool to measure the delay between two light pulses. Due to their limitations in the response time, they allow for a precision of 50 ps at best, which is too coarse for light pulses with a duration of ≈ 100 fs. An approach employing diodes also results in additional experimental effort, since it includes the installation of a diode at the interaction region. Later, the diode has to be replaced by the liquid-jet to conduct the pump-probe experiment. More convenient is an approach that makes use of the liquid-jet as the sample for a CC measurement, similar to the study presented in section 5.5. There, the LAPE process in a gas was employed for the characterization of the pulse duration of monochromatized HHG light.

As it is described in the previous section, the space charge effect that influences the TEY is used to establish spatial and rough temporal overlap of pump and probe light pulses. The variation in the TEY indicates the approximate delay stage position of t_0. If the photoelectron signal is not integrated over the entire range of kinetic energies, but only over a range of higher kinetic energies, a partial electron yield (PEY) is determined instead. Figure 8.9 displays such a PEY depending on delay stage position. The PEY was determined on the same data set as the

TEY shown in 8.8. The PEY is represented by black circles while the graph of a Gaussian function fitted to the data is represented by the red line. As can be seen from the figure, t_0, indicated by the maximum of the CC curve, lies at a delay stage position of 166.92 mm. This is ≈ 80 µm before the rough delay stage position found from the TEY curve shown in figure 8.8.

Cross-correlation measurements on hemin-DMSO solutions exhibited temporal widths of $100 - 110$ fs due to the large dispersion of the UV beam in air and in optical components of the UV pump beam path.

8.5.6. Pump-probe photoelectron spectra of Soret-excited hemin-DMSO solutions

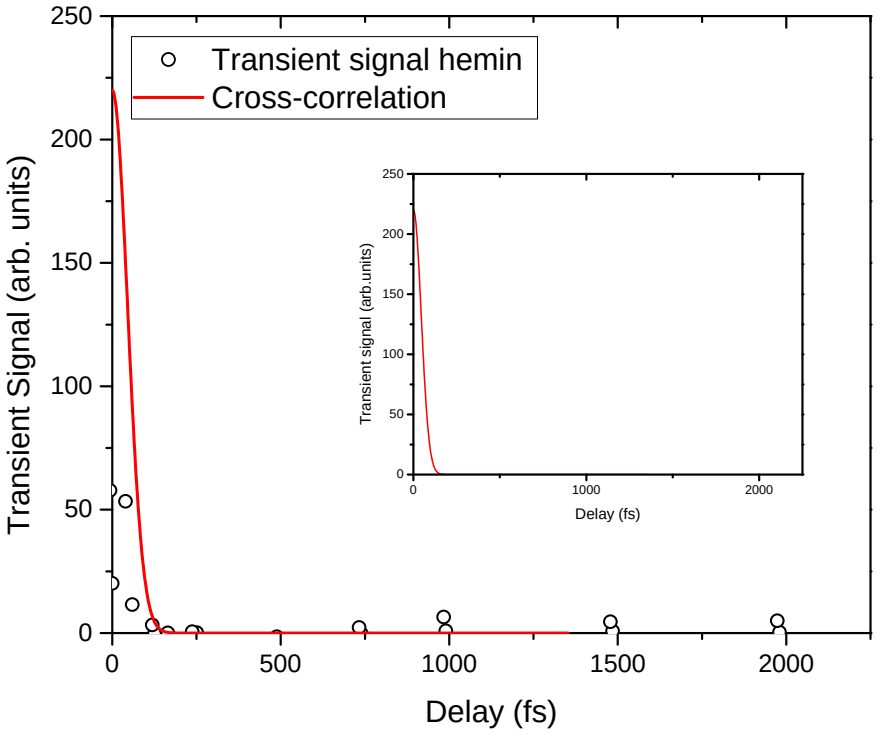

Figure 8.10.: Pump-probe photoelectron spectrum of a hemin-DMSO solution. For comparison, the inset shows the result of a similar measurement of a DMSO solution.

Pump-probe photoelectron spectra of hemin-DMSO solutions have been acquired, and evaluated according to the procedure described in section 8.4. The resulting transient signal is displayed in figure 8.10 as a function of time delay between pump and probe pulse. The experimental data are represented by black circles, while the red line is an exemplary cross correlation between the SHG pump and

XUV probe pulses. The result of a similar pump probe experiment conducted on DMSO is displayed in the inset. From the comparison of the pump-probe data with the cross-correlation curve, no decay of an additional state is apparent. This is the case for the pure DMSO solution as well as for hemin dissolved in DMSO. The predicted relaxation of the Soret-excited porphyrin from the S_2 state via a ring-to-metal charge-transfer state to a vacant metal d-orbital is ultrafast, and with a cross-correlation width of 100 fs not observable. The back-donation of an electron to the ring of hemin is still a fast process, but with a lifetime of 250 fs it should be visible in the transient spectrum.

The back-donation from the metal to the ring could be more easy to track in a different evaluation routine, where changes of the photoelectron yield of the ring centered HOMO (see section 8.2.2) of the molecule is analyzed. This is not possible in the present combination of sample system, and spectrometer settings, though. As it was shown in section 8.5.3, the photoelectron peak of the HOMO of hemin is partially hidden under the intense photoelectron signal of the solvent. In the WAM the detector of the spectrometer would be saturated if this part of the spectrum would be recorded. A different solvent with a larger ionization potential would allow to analyze the yield of the porphyrin HOMO during the pump-probe process.

8.6. Conclusion

The setup for XUV photoelectron spectroscopy of liquids described in Part I was used to investigate the transient photoelectron signal of hemin-DMSO solutions. Hemin, or protoporphyrin IX chloride, was chosen as a model porphyrin due to its similarity to natural porphyrins such as heme. Furthermore, hemin can be dissolved in DMSO at high concentrations necessary for PES studies. Although porphyrins are known to form aggregates at high concentrations, the molecule is still in its monomeric state in the present case of a hemin-DMSO solution of 10 mM concentration, as it was verified by an undisturbed absorption spectrum.

The XUV photoelectron spectrum of liquid DMSO was recorded and compared to the spectrum of the gaseous molecule. Similar to the case of water presented in chapter 7, photoelectron peaks originating from the valence orbitals of DMSO are broadened and shifted to lower binding energies. In the particular case of the HOMO of DMSO, the binding energy of the liquid molecules is shifted by ≈ 1.3 eV, which is similar to the case of water.

The binding energy of the HOMO of hemin dissolved in DMSO was determined to be 5.8 eV. This is lower by ≈ 0.3 eV compared to the binding energy of the free Fe(III)TTPCl molecule in the gas phase [151]. Due to the large shift of the HOMO of the DMSO molecule to lower binding energies, the outer valence orbitals of hemin are partially concealed by the photoelectron signal of the solvent. This imposes difficulties on the evaluation of the pump-probe photoelectron spectra of the hemin solution, since it is not possible to calibrate the spectra to the porphyrin HOMO. However, this would be very useful to compare different series of spectra, estimate if space charge effects are present and correct the spectra for their influence. Most of all, it would allow to follow the photoelectron yield of the HOMO during the pump-probe process. For further experiments, it would be useful to change the sample system to a solvent which has a higher binding energy in its liquid state.

To the best knowledge, the results presented in this chapter represent the first static and transient PES studies of liquid DMSO and hemin-DMSO solutions acquired with a HHG light source.

9. Summary

This work presents a newly build setup for time-resolved photoelectron spectroscopy of liquids with the use of XUV light generated from ultrashort laser pulses in the process of high harmonic generation. The first part of the thesis describes the design and the results from the characterization of the setup [52], while the second part shows its application in static XUV photoelectron spectra of aqueous sodium halide solutions and UV-pump-XUV-probe photoelectron spectra of hemin-DMSO solutions.

The setup is designed to offer monochromatized XUV light with photon energies of 26.35 eV, 32.55 eV and 38.75 eV. Special attention has been given to preserve the ultrashort duration of the laser-light pulses upon monochromatization of the XUV light, while at the same time achieve a high efficiency of the beamline. Therefore, a novel type of monochromator has been chosen, which employs off-center reflective zone plates (ORZPs) as dispersive elements. By engraving the outer part of a traditional Fresnel zone plate onto a reflecting surface, a diffractive structure is created, that focuses a specific photon energy to a specific position. The installation of a slit at this position allows the selection of this photon energy [28]. The thus monochromatized XUV light, which is divergent behind the slit, is refocused to the interaction region of the PES experiment by a toroidal mirror. The high efficiency of 28 % of the ORZP and the use of just one additional mirror results in a very good overall efficiency of 20 % of the beamline. Furthermore, the simplicity of a beamline that incorporates only two optical elements results in a high pointing stability of the focused XUV light, which is important if small targets such as liquid jets are used. By fabricating three ORZP structures on one substrate, the three photon energies of 26.35 eV, 32.55 eV and 38.75 eV are available for the PES experiment, and can be easily chosen by translating the zone plate substrate. The demagnification factor of $M = \frac{35}{100}$ of the zone plates results in a focal spot of 40 µm at the interaction region, which is close to the size of the liquid jet. The monochromatized XUV light has a spectral width of ≈ 150 eV. Most important, the duration of the XUV light pulses, which were generated from 25 fs IR laser pulses, was determined in a cross-correlation measurement to be only 45 fs, which is outstanding for a setup that employs only one dispersive element. The described setup is the first facility, that was specifically designed to combine a HHG light source with reflection zone plates.

The XUV light source was employed to record static photoelectron spectra of aqueous sodium iodide solutions and mixed aqueous solutions with fixed sodium iodide concentration, and varied sodium chloride concentration. The observed changes in the photoelectron yield of the halide ions indicate a probing depth in the PES experiment that is large enough to probe the surface region and parts of

the bulk of the liquid jet. The spectral features of the VBE of the halide ions, and of the HOMO of liquid water show changes with the increase of salt concentration. For all three species, I^-, Cl^- and water, a slight shift to larger binding energies is apparent upon an increase of the salt concentration. With the present noise in the data, it is difficult to evaluate the absolute value of the shift, though. Furthermore, the spectral width of the $1b_1$ peak of liquid water decreases with an increase of NaI concentration, but stays constant with the increase of NaCl concentration. These findings indicate a small, but measurable effect of the halide ions on the structure of the aqueous solutions. This effect is stronger for iodide than for chloride.

In the last part of the thesis, the XUV light source was employed to record pump-probe photoelectron spectra of Soret-excited hemin dissolved in DMSO. The HOMOs of both, hemin and DMSO, exhibit shifts to lower binding energies for the molecules in solution than compared to the VBE of the gaseous molecules. Since this shift is larger for DMSO, the photoelectron peak of the HOMO of liquid DMSO partly overlays the photoelectron peak of the HOMO of the dissolved hemin molecules. Nevertheless, the binding energy of the HOMO of hemin dissolved in DMSO was determined to be 5.8 eV. In the evaluation of the pump-probe measurements of the Soret-excited hemin-DMSO solution, no decay additional to the cross correlation between UV-pump and XUV-probe pulse is apparent. To the present knowledge of the author this work represents the first application of a femtosecond HHG light source to experiments with transient PES of porphyrins in solution.

Bibliography

[1] R. Jiang, D. Mou, Y. Wu, L. Huang, C. D. McMillen, J. Kolis, H. G. Giesber, J. J. Egan, and A. Kaminski, *Rev. Sci. Instrum.*, 2014, **85**, 033902. doi:10.1063/1.4867517.

[2] S.-B. Dai, N. Zong, F. Yang, S.-J. Zhang, Z.-M. Wang, F.-F. Zhang, W. Tu, L.-Q. Shang, L.-J. Liu, X.-Y. Wang, J.-Y. Zhang, D.-F. Cui, Q.-J. Peng, R.-K. Li, C.-T. Chen, and Z.-Y. Xu, *Opt. Lett.*, 2015, **40**, 3268–3271. doi:10.1364/OL.40.003268.

[3] P. Radcliffe, S. Düsterer, A. Azima, H. Redlin, J. Feldhaus, J. Dardis, K. Kavanagh, H. Luna, J. Pedregosa Gutierrez, P. Yeates, E. T. Kennedy, J. T. Costello, A. Delserieys, and C. L. S. Lewis, *Appl. Phys. Lett.*, 2007, **90**, 131108. doi:10.1063/1.2716360.

[4] J. Reintjes, Chiao-Yao She, and R. Eckardt, *IEEE J. Quant. Electron.*, Aug 1978, **14**, 581–596. doi:10.1109/JQE.1978.1069853.

[5] A. McPherson, G. Gibson, H. Jara, U. Johann, T. S. Luk, I. A. McIntyre, K. Boyer, and C. K. Rhodes, *J. Opt. Soc. Am. B*, Apr 1987, **4**, 595–601. doi:10.1364/JOSAB.4.000595.

[6] P. B. Corkum, *Phys. Rev. Lett.*, Sep 1993, **71**, 1994–1997. doi:10.1103/PhysRevLett.71.1994.

[7] M. Ferray, A. L'Huillier, X. F. Li, L. A. Lompre, G. Mainfray, and C. Manus, *J. Phys. B: At., Mol. Opt. Phys.*, 1988, **21**, L31. doi:10.1088/0953-4075/21/3/001.

[8] P. Siffalovic, M. Drescher, M. Spiewec, T. Wiesenthal, Y. C. Lim, R. Weidner, A. Elizarov, and U. Heinzmann, *Rev. Sci. Instrum.*, 2001, **72**, 30–35. doi:10.1063/1.1329904.

[9] L. Nugent-Glandorf, M. Scheer, D. A. Samuels, V. Bierbaum, and S. R. Leone, *Rev. Sci. Instrum.*, 2002, **73**, 1875–1886. doi:10.1063/1.1459094.

[10] S. Mathias, L. Miaja-Avila, M. M. Murnane, H. Kapteyn, M. Aeschlimann, and M. Bauer, *Rev. Sci. Instrum.*, 2007, **78**, 083105. doi:10.1063/1.2773783.

[11] G. L. Dakovski, Y. Li, T. Durakiewicz, and G. Rodriguez, *Rev. Sci. Instrum.*, 2010, **81**, 073108. doi:10.1063/1.3460267.

[12] M.-C. Chen, C. Mancuso, C. Hernandez-Garcia, F. Dollar, B. Galloway, D. Popmintchev, P.-C. Huang, B. Walker, L. Plaja, A. A. Jaron-Becker, A. Becker, M. M. Murnane, H. C. Kapteyn, and T. Popmintchev, *Proc. Natl. Acad. Sci. U. S. A.*, 2014, **111**, E2361–E2367. doi:10.1073/pnas.1407421111.

[13] Ph. Zeitoun, G. Faivre, S. Sebban, T. Mocek, A. Hallou, M. Fajardo, D. Aubert, Ph. Balcou, F. Burgy, D. Douillet, S. Kazamias, G. de Lachèze-Murel, T. Lefrou, S. le Pape, P. Mercere, H. Merdji, A. S. Morlens, J. P. Rousseau, and C. Valentin, *Nature*, Sep 2004, **431**, 426–429. doi:10.1038/nature02883.

[14] G. Lambert, T. Hara, D. Garzella, T. Tanikawa, M. Labat, B. Carre, H. Kitamura, T. Shintake, M. Bougeard, S. Inoue, Y. Tanaka, P. Salieres, H. Merdji, O. Chubar, O. Gobert, K. Tahara, and M.-E. Couprie, *Nature Phys.*, Apr 2008, **4**, 296–300. doi:10.1038/nphys889.

[15] D. J. Dunning, N. R. Thompson, and B. W. J. McNeil, *J. Mod. Opt.*, 2011, **58**, 1362–1373. doi:10.1080/09500340.2011.586475.

[16] H. Tomizawa, T. Sato, K. Ogawa, K. Togawa, T. Tanaka, T. Hara, M. Yabashi, H. Tanaka, T. Ishikawa, T. Togashi, S. Matsubara, Y. Okayasu, T. Watanabe, E. J. Takahashi, K. Midorikawa, M. Aoyama, K. Yamakawa, S. Owada, A. Iwasaki, and K. Yamanouchi, *High Power Laser Sci. Eng.*, 2015, **3**, e14. doi:10.1017/hpl.2015.9.

[17] M. Nakasuji, A. Tokimasa, T. Harada, Y. Nagata, T. Watanabe, K. Midorikawa, and H. Kinoshita, *Jpn. J. Appl. Phys.*, 2012, **51**, 06FB09. doi:10.1143/JJAP.51.06FB09.

[18] H. Kinoshita, T. Harada, Y. Nagata, T. Watanabe, and K. Midorikawa, *Jpn. J. Appl. Phys.*, 2014, **53**, 086701. doi:10.7567/JJAP.53.086701.

[19] J. Miao, R. L. Sandberg, and C. Song, *IEEE J. Sel. Topics Quantum Electron.*, JAN-FEB 2012, **18**, 399–410. doi:10.1109/JSTQE.2011.2157306.

[20] Y. Meng, C. Zhang, C. Marceau, A. Yu. Naumov, P. B. Corkum, and D. M. Villeneuve, *Opt. Express*, NOV 2 2015, **23**, 28960–28969. doi:10.1364/OE.23.028960.

[21] J. Hüve, T. Haarlammert, T. Steinbrück, J. Kutzner, G. Tsilimis, and Zacharias H., *Opt. Commun.*, 2006, **266**, 261–265. doi:10.1016/j.optcom.2006.04.063.

[22] T. Popmintchev, M.-C. Chen, D. Popmintchev, P. Arpin, S. Brown, S. Ališauskas, G. Andriukaitis, T. Balčiunas, O. D. Mücke, A. Pugzlys, A. Baltuška, B. Shim, S. E. Schrauth, A. Gaeta, C. Hernández-García, L. Plaja, A. Becker, A. Jaron-Becker, M. M. Murnane, and H. C. Kapteyn, *Science*, 2012, **336**, 1287–1291. doi:10.1126/science.1218497.

[23] R. W. Schoenlein, S. Chattopadhyay, H. H. W. Chong, T. E. Glover, P. A. Heimann, C. V. Shank, A. A. Zholents, and M. S. Zolotorev, *Science*, 2000, **287**, 2237–2240. doi:10.1126/science.287.5461.2237.

[24] B. Niemann, D. Rudolph, and G. Schmahl, *Opt. Comm.*, 1974, **12**, 160 – 163. doi:10.1016/0030-4018(74)90381-2.

[25] C. Jacobsen, S. Williams, E. Anderson, M.T. Browne, C.J. Buckley, D. Kern, J. Kirz, M. Rivers, and X. Zhang, *Opt. Commun.*, 1991, **86**, 351 – 364. doi:10.1016/0030-4018(91)90016-7.

[26] P. Vettiger, U. Staufer, D.P. Kern, G. Schmahl, D. Rudolph, G. Schneider, J. Thieme, T. Schliebe, B. Kaulich, and M. Hettwer, *Microelectron. Eng.*, 1996, **32**, 351 – 367. doi:10.1016/0167-9317(95)00177-8.

[27] M. Ibek, T. Leitner, A. Erko, A. Firsov, and P. Wernet, *Rev. Sci. Instrum.*, 2013, **84**, 103102. doi:10.1063/1.4822114.

[28] M. Brzhezinskaya, A. Firsov, K. Holldack, T. Kachel, R. Mitzner, N. Pontius, J.-S. Schmidt, M. Sperling, C. Stamm, A. Föhlisch, and A. Erko, *J. Synchrotron Radiat.*, Jul 2013, **20**, 522–530. doi:10.1107/S0909049513008613.

[29] M. Lewenstein, Ph. Balcou, M. Yu. Ivanov, Anne L'Huillier, and P. B. Corkum, *Phys. Rev. A*, Mar 1994, **49**, 2117–2132. doi:10.1103/PhysRevA.49.2117.

[30] X. He, M. Miranda, J. Schwenke, O. Guilbaud, T. Ruchon, C. Heyl, E. Georgadiou, R. Rakowski, A. Persson, M. B. Gaarde, and A. L'Huillier, *Phys. Rev. A*, Jun 2009, **79**, 063829. doi:10.1103/PhysRevA.79.063829.

[31] S. C. Rae, K. Burnett, and J. Cooper, *Phys. Rev. A*, Oct 1994, **50**, 3438–3446. doi:10.1103/PhysRevA.50.3438.

[32] M. B. Gaarde, J. L. Tate, and K. J. Schafer, *J. Phys. B: At., Mol. Opt. Phys.*, 2008, **41**, 132001. doi:10.1088/0953-4075/41/13/132001.

[33] E. Constant, D. Garzella, P. Breger, E. Mével, Ch. Dorrer, C. Le Blanc, F. Salin, and P. Agostini, *Phys. Rev. Lett.*, Feb 1999, **82**, 1668–1671. doi:10.1103/PhysRevLett.82.1668.

[34] A. Pirri, C. Corsi, and M. Bellini, *Phys. Rev. A*, Jul 2008, **78**, 011801. doi:10.1103/PhysRevA.78.011801.

[35] M. Nisoli, S. De Silvestri, O. Svelto, R. Szipöcs, K. Ferencz, Ch. Spielmann, S. Sartania, and F. Krausz, *Opt. Lett.*, Apr 1997, **22**, 522–524. doi:10.1364/OL.22.000522.

[36] D. Attwood. *Soft X-Rays and Extreme Ultraviolet Radiation, Principles and Applications*. Cambridge University Press, 1999.

[37] D. M. Paganin. *Coherent X-Ray Optics*. Oxford Science Publications, Oxford University Press, 2006.

[38] P. Wernet, J. Gaudin, K. Godehusen, O. Schwarzkopf, and W. Eberhardt, *Rev. Sci. Instrum.*, 2011, **82**, 063114. doi:10.1063/1.3600901.

[39] K. R. Siefermann, Y. Liu, E. Lugovoy, O. Link, M. Faubel, U. Buck, B. Winter, and B. Abel, *Nature Chem.*, April 2010, **2**, 274–279. doi:10.1038/nchem.580.

[40] Website, 2016. URL http://www.horiba.com/scientific/products/vacuum-uv-spectroscopy/vacuum-monochromators-and-systems/vuv-monochromators-and-spectrographs/.

[41] Y.-Y. Yang, F. Süßmann, S. Zherebtsov, I. Pupeza, J. Kaster, D. Lehr, H.-J. Fuchs, E.-B. Kley, E. Fill, X.-M. Duan, Z.-S. Zhao, F. Krausz, S. L. Stebbings, and M. F. Kling, *Opt. Express*, Jan 2011, **19**, 1954–1962. doi:10.1364/OE.19.001954.

[42] P. Villoresi, *Appl. Opt.*, 1999, **38**, 6040–6049. doi:10.1364/AO.38.006040.

[43] M. Ito, Y. Kataoka, T. Okamoto, M. Yamashita, and T. Sekikawa, *Opt. Express*, 2010, **18**, 6071–6078. doi:10.1364/OE.18.006071.

[44] L. Poletto, P. Villoresi, F. Frasetto, F. Calegari, F. Ferrari, M. Lucchini, G. Sansone, and M. Nisoli, *Rev. Sci. Instrum.*, 2009, **80**, 123109. doi:10.1063/1.3273964.

[45] L. Poletto and G. Tondello, *Laser Part. Beams*, March 2001, **19**, 141–145. 2nd ULIA Conference, PISA, ITALY, SEP 29-OCT 03, 2000.

[46] A. J. Corso, P. Zuppella, E. Principi, E. Giangrisostomi, F. Bencivenga, A. Gessini, S. Zuccon, C. Masciovecchio, A. Giglia, S. Nannarone, and M. G. Pelizzo, *J. Opt.*, 2015, **17**, 025505. doi:10.1088/2040-8978/17/2/025505.

[47] O. E. Myers, *Am. J. Phys*, 1951, **19**, 359–365. doi:10.1119/1.1932827.

[48] U. Vogt, M. Wieland, T. Wilhein, M. Beck, and H. Stiel, *Rev. Sci. Instrum.*, 2001, **72**, 53–57. doi:10.1063/1.1329901.

[49] V. V. Aristov, S. V. Gaponov, V. M. Genkin, Yu. A. Goratov, A. I. Erko, V. V. Martynov, L. A. Matveev, N. N. Salashchenko, and A. A. Fraerman, *J. Exp. Theor. Phys.*, 1986, **44**, 265–267. URL http://www.jetpletters.ac.ru/ps/1378/article_21023.pdf.

[50] Yu. A. Basov, D. V. Roshchupkin, and A. E. Yakshin, *Opt. Comm.*, 1994, **109**, 324 – 327. doi:10.1016/0030-4018(94)90700-5.

[51] T. Wilhein, D. Hambach, B. Niemann, M. Berglund, L. Rymell, and H. M. Hertz, *Appl. Phys. Lett.*, 1997, **71**, 190–192. doi:10.1063/1.119497.

[52] J. Metje, M. Borgwardt, A. Moguilevski, A. Kothe, N. Engel, M. Wilke, R. Al-Obaidi, D. Tolksdorf, A. Firsov, M. Brzhezinskaya, A. Erko, I. Yu. Kiyan, and E. F. Aziz, *Opt. Express*, 2014, **22**, 10747–10760. doi:10.1364/OE.22.010747.

[53] J. B. Bertrand, H. J. Wörner, H.-C. Bandulet, É. Bisson, M. Spanner, J.-C. Kieffer, D. M. Villeneuve, and P. B. Corkum, *Phys. Rev. Lett.*, Jan 2011, **106**, 023001. doi:10.1103/PhysRevLett.106.023001.

[54] M. Negro, M. Devetta, D. Facciala, A. G. Ciriolo, F. Calegari, F. Frassetto, L. Poletto, V. Tosa, C. Vozzi, and S. Stagira, *Opt. Express*, DEC 1 2014, **22**, 29778–29786. doi:10.1364/OE.22.029778.

[55] A. Kothe. *Charge Transfer to Solvent Dynamics in Iodide Aqueous Solution Studied at Ionization Threshold*. PhD thesis, Freie Universität Berlin, 12 2014. URL http://www.diss.fu-berlin.de/diss/receive/FUDISS_thesis_000000099263.

[56] P. Kruit and F. H. Read, *J. Phys. E: Sci. Instrum.*, 1983, **16**, 313–324. doi:10.1088/0022-3735/16/4/016. © IOP Publishing. Reproduced with permission. All rights reserved.

[57] A. Kothe, J. Metje, M. Wilke, A. Moguilevski, N. Engel, R. Al-Obaidi, C. Richter, R. Golnak, I. Yu. Kiyan, and E. F. Aziz, *Rev. Sci. Instrum.*, 2013, **84**, 023106. doi:10.1063/1.4791792.

[58] Website, 2016. URL http://www.ibsmagnet.de/de/fluxdensity/flussdichte_berechnung.php.

[59] G. Johansson, J. Hedman, A. Berndtsson, Klasson M., and R. Nilsson, *J. Electron Spectrosc. Relat. Phenom.*, 1973, **2**, 295–317. doi:10.1016/0368-2048(73)80022-2.

[60] L. Lablanquie, P. ad Andric, J. Palaudoux, U. Becker, M. Braune, J. Viefhaus, J. H. D. Eland, and F. Penet, *J. Electron Spectrosc. Relat. Phenom.*, 2007, **156-158**, 51–57. doi:10.1016/j.elspec.2006.11.062.

[61] Gwyn P. WilliamsX-Ray Data Booklet. Website, 2016. URL http://xdb.lbl.gov/Section1/Table_1-1a.htm.

[62] T. Tsuboi, Emily Y. Xu, Y. K. Bae, and K. T. Gillen, *Rev. Sci. Instrum.*, 1988, **59**, 1357–1362. doi:10.1063/1.1139722.

[63] Website, 2016. URL http://www.specs.de/cms/front_content.php?idcat=223.

[64] Franz Schäfers. *The BESSY Raytrace Program RAY*, chapter 2, pages 9–41. Springer Berlin Heidelberg, Berlin, Heidelberg, 2008. ISBN 978-3-540-74561-7. doi:10.1007/978-3-540-74561-7_2.

[65] I. Velchev, W. Hogervorst, and W. Ubachs, *J. Phys. B: At., Mol. Opt. Phys.*, 1999, **32**, L511. doi:10.1088/0953-4075/32/17/105.

[66] A. Weingartshofer, J. K. Holmes, G. Caudle, E. M. Clarke, and H. Krüger, *Phys. Rev. Lett.*, Aug 1977, **39**, 269–270. doi:10.1103/PhysRevLett.39.269.

[67] T. E. Glover, R. W. Schoenlein, A. H. Chin, and C. V. Shank, *Phys. Rev. Lett.*, April 1996, **76**, 2468–2471. doi:10.1103/PhysRevLett.76.2468.

[68] J. M. Schins, P. Breger, P. Agostini, R. C. Constantinescu, H. G. Muller, A. Bouhal, G. Grillon, A. Antonetti, and A. Mysyrowicz, *J. Opt. Soc Am. B*, 1996, **13**, 197–200. doi:10.1364/JOSAB.13.000197.

[69] N. B. Delone, S. P. Goreslavsky, and V. P. Krainov, *J. Phys. B: At., Mol. Opt. Phys.*, September 1989, **22**, 2941–2945. doi:10.1088/0953-4075/22/18/016.

[70] D. M. Murphy, J. R. Anderson, P. K. Quinn, L. M. McInnes, F. J. Brechtel, S. M. Kreidenweis, A. M. Middlebrook, M. Posfai, D. S. Thomson, and P. R. Buseck, *Nature*, March 1998, **392**, 62–65. doi:10.1038/32138.

[71] P. K. Quinn, D. J. Coffman, T. S. Bates, T. L. Miller, J. E. Johnson, K. Voss, E. J. Welton, and C. Neusüss, *J. Geophys. Res.-Atmos.*, 2001, **106**, 20783–20809. doi:10.1029/2000JD900577.

[72] S. W. Hunt, M. Roeselová, W. Wang, L. M. Wingen, E. M. Knipping, D. J. Tobias, D. Dabdub, , and B. J. Finlayson-Pitts, *J. Phys. Chem. A*, 2004, **108**, 11559–11572. doi:10.1021/jp0467346.

[73] B. J. Finlayson-Pitts, M. J. Ezell, and J. N. Pitts, *Nature*, January 1989, **337**, 241–244. doi:10.1038/337241a0.

[74] S. Pechtl, G. Schmitz, and R. von Glasow, *Atmos. Chem. Phys.*, 2007, **7**, 1381–1393. doi:10.5194/acp-7-1381-2007.

[75] P. Jungwirth and D. J. Tobias, *J. Phys. Chem. B*, 2001, **105**, 10468–10472. doi:10.1021/jp012750g.

[76] P. Jungwirth and D. J. Tobias, *J. Phys. Chem. B*, 2002, **106**, 6361–6373. doi:10.1021/jp020242g.

[77] B. A. Bauer and S. Patel, *J. Chem. Phys.*, 2010, **132**, 024713. doi:10.1063/1.3269673.

[78] I. Gladich, P. B. Shepson, M. A. Carignano, and I. Szleifer, *J. Phys. Chem. A*, 2011, **115**, 5895–5899. doi:10.1021/jp110208a. PMID: 21319857.

[79] T. Ishiyama, T. Imamura, and A. Morita, *Chem. Rev.*, 2014, **114**, 8447–8470. doi:10.1021/cr4004133. PMID: 24678883.

[80] L. M. Pegram and M. T. Record, *J. Phys. Chem. B*, 2007, **111**, 5411–5417. doi:10.1021/jp070245z. PMID: 17432897.

[81] D. J. Tobias and J. C. Hemminger, *Science*, 2008, **319**, 1197–1198. doi:10.1126/science.1152799.

[82] R. Böhm, H. Morgner, J. Oberbrodhage, and M. Wulf, *Surf. Sci.*, 1994, **317**, 407 – 421. doi:10.1016/0039-6028(94)90296-8.

[83] B. L. Eggimann and J. I. Siepmann, *J. Phys. Chem. C*, 2008, **112**, 210–218. doi:10.1021/jp076054d.

[84] T. T. Duignan, D. F. Parsons, and B. W. Ninham, *J. Phys. Chem. B*, July 2014, **118**, 8700–8710. doi:10.1021/jp502887e.

[85] D. Liu, G. Ma, L. M. Levering, and H. C. Allen, *J. Phys. Chem. B*, 2004, **108**, 2252–2260. doi:10.1021/jp036169r.

[86] P. B. Petersen and R. J. Saykally, *J. Phys. Chem. B*, 2006, **110**, 14060–14073. doi:10.1021/jp0601825. PMID: 16854101.

[87] H.-t. Bian, R.-r. Feng, Y.-y. Xu, Y. Guo, and H.-f. Wang, *Phys. Chem. Chem. Phys.*, 2008, **10**, 4920–4931. doi:10.1039/B806362A.

[88] M. Faubel, B. Steiner, and J.P. Toennies, *J. Electron Spectrosc. Relat. Phenom.*, OCT 1998, **95**, 159–169. doi:10.1016/S0368-2048(98)00208-4.

[89] M. Faubel and B. Steiner. *Photoelectron Spectroscopy at Liquid Water Surfaces*. Springer, 2000. pp 634-690.

[90] B. Winter, R. Weber, W. Widdra, M. Dittmar, M. Faubel, and Hertel I. V., *J. Phys. Chem. A*, 2004, **108**, 2625–2632. doi:10.1021/jp030263q. © 2006 American Chemical Society.

[91] B. Winter and M. Faubel, *Chem. Rev.*, 2006, **106**, 1176–1211. doi:10.1021/cr040381p. © 2006 American Chemical Society.

[92] B. Winter, *Nucl. Instrum. Meth. A*, 2009, **601**, 139 – 150. doi:10.1016/j.nima.2008.12.108. Special issue in honour of Prof. Kai Siegbahn.

[93] R. Weber, B. Winter, P. M. Schmidt, W. Widdra, I. V. Hertel, M. Dittmar, and M. Faubel, *J. Phys. Chem. B*, 2004, **108**, 4729–4736. doi:10.1021/jp030776x.

[94] B. Winter, R. Weber, P. M. Schmidt, I. V. Hertel, M. Faubel, L. Vrbka, and P. Jungwirth, *J. Phys. Chem. B*, 2004, **108**, 14558–14564. doi:10.1021/jp0493531.

[95] N. Kurahashi, S. Karashima, Y. Tang, T. Horio, B. Abulimiti, Y.-Ic. Suzuki, Y. Ogi, M. Oura, and T. Suzuki, *J. Chem. Phys.*, 2014, **140**, –. doi:10.1063/1.4871877.

[96] N. Ottosson, M. Faubel, S. E. Bradforth, P. Jungwirth, and B. Winter, *J. Electron Spectrosc. Relat. Phenom.*, 2010, **177**, 60 – 70. doi:10.1016/j.elspec.2009.08.007. Water and Hydrogen Bonds.

[97] S. Thürmer, R. Seidel, M. Faubel, W. Eberhardt, J. C. Hemminger, S. E. Bradforth, and B. Winter, *Phys. Rev. Lett.*, Oct 2013, **111**, 173005. doi:10.1103/PhysRevLett.111.173005.

[98] Y.-I. Suzuki, K. Nishizawa, N. Kurahashi, and T. Suzuki, *Phys. Rev. E*, Jul 2014, **90**, 010302. doi:10.1103/PhysRevE.90.010302.

[99] Y. Hiranuma, K. Kaniwa, M. Shoji, and F. Mafuné, *J. Phys. Chem. A*, 2011, **115**, 8493–8497. doi:10.1021/jp204195t.

[100] A. W. Potts and W. C. Price, *Proc. R. Soc. Lond. A*, 1972, **326**, 181–197. URL http://www.jstor.org/stable/pdf/78047.pdf.

[101] K. Nishizawa, N. Kurahashi, K. Sekiguchi, T. Mizuno, Y. Ogi, T. Horio, M. Oura, N. Kosugi, and T. Suzuki, *Phys. Chem. Chem. Phys.*, 2011, **13**, 413–417. doi:10.1039/C0CP01636E.

[102] M. Born, *Zeitschrift für Physik*, 1920, **1**, 45–48. doi:10.1007/BF01881023.

[103] M. Lundholm, H. Siegbahn, S. Holmberg, and M. Arbman, *J. Electron Spectrosc. Relat. Phenom.*, 1986, **40**, 163 – 180. doi:10.1016/0368-2048(86)80015-9.

[104] B. Winter, R. Weber, I. V. Hertel, M. Faubel, P. Jungwirth, E. C. Brown, and S. E. Bradforth, *J. Am. Chem. Soc.*, 2005, **127**, 7203–7214. doi:10.1021/ja042908l. PMID: 15884962.

[105] P. Wernet, D. Nordlund, U. Bergmann, M. Cavalleri, M. Odelius, H. Ogasawara, L. Å. Näslund, T. K. Hirsch, L. Ojamäe, P. Glatzel, L. G. M. Pettersson, and A. Nilsson, *Science*, 2004, **304**, 995–999. doi:10.1126/science.1096205.

[106] A. Nilsson, D. Nordlund, I. Waluyo, N. Huang, H. Ogasawara, S. Kaya, U. Bergmann, L.-Å. Näslund, H. Öström, Ph. Wernet, K.J. Andersson, T. Schiros, and L.G.M. Pettersson, *J. Electron Spectrosc. Relat. Phenom.*, 2010, **177**, 99 – 129. doi:10.1016/j.elspec.2010.02.005. Water and Hydrogen Bonds.

[107] D. Nordlund, M. Odelius, H. Bluhm, H. Ogasawara, L.G.M. Pettersson, and A. Nilsson, *Chem. Phys. Lett.*, 2008, **460**, 86 – 92. doi:10.1016/j.cplett.2008.04.096.

[108] K. M. Lange. *Structure and Dynamics of Water and Ions in Solution - Soft X-Ray Absorption and Emission Studies*. PhD thesis, Freie Universität Berlin, 2012. URL http://www.diss.fu-berlin.de/diss/receive/FUDISS_thesis_000000037215.

[109] M. Faubel, B. Steiner, and J. P. Toennies, *J. Chem. Phys.*, 1997, **106**, 9013–9031. doi:10.1063/1.474034.

[110] K. R. Wilson, B. S. Rude, J. Smith, C. Cappa, D. T. Co, R. D. Schaller, M. Larsson, T. Catalano, and R. J. Saykally, *Rev. Sci. Instrum.*, 2004, **75**, 725–736. doi:10.1063/1.1645656.

[111] M. Faubel, S. Schlemmer, and J.P. Toennies, *Zeitschrift für Physik D-Atoms, Molecules and Clusters*, 1988, **10**, 269–277. doi:10.1007/BF01384861.

[112] N. Preissler, F. Buchner, T. Schultz, and A. Lübcke, *J. Phys. Chem. B*, 2013, **117**, 2422–2428. doi:10.1021/jp304773n.

[113] M. P. Seah and W. A. Dench, *Surf. Interface Anal.*, 1979, **1**, 2–11. doi:10.1002/sia.74001010.

[114] S. Hellmann, K. Rossnagel, M. Marczynski-Bühlow, and L. Kipp, *Phys. Rev. B*, Jan 2009, **79**, 035402. doi:10.1103/PhysRevB.79.035402.

[115] S. Hellmann, C. Sohrt, M. Beye, T. Rohwer, F. Sorgenfrei, M. Marczynski-Bühlow, M. Kalläne, H. Redlin, F. Hennies, M. Bauer, A. Föhlisch, L. Kipp, W. Wurth, and K. Rossnagel, *New J. Phys.*, 2012, **14**, 013062. doi:10.1016/j.ccr.2006.02.014.

[116] B. Frietsch, R. Carley, K. Doebrich, C. Gahl, M. Teichmann, O. Schwarzkopf, Ph Wernet, and M. Weinelt, *Rev. Sci. Instrum.*, July 2013, **84**, 075106. doi:10.1063/1.4812992.

[117] D. A. Shirley, *Phys. Rev. B*, Jun 1972, **5**, 4709–4714. doi:10.1103/PhysRevB.5.4709.

[118] G. L. Warren and S. Patel, *J. Phys. Chem. B*, 2008, **112**, 11679–11693. doi:10.1021/jp8038835. PMID: 18712908.

[119] T. Ishiyama and A. Morita, *J. Phys. Chem. C*, 2007, **111**, 721–737. doi:10.1021/jp065191s.

[120] G. Archontis, A. Leontidis, and G. Andreou, *J. Phys. Chem. B*, 2005, **109**, 17957–17966. doi:10.1021/jp0526041.

[121] Jim Clark, 2016. URL http://www.chemguide.co.uk/atoms/properties/atradius.html.

[122] W. M. Campbell, K. W. Jolley , P. Wagner , K. Wagner , P. J. Walsh, K. C. Gordon, L. Schmidt-Mende, M. K. Nazeeruddin, Q. Wang, M. Grätzel, , and D. L. Officer, *J. Phys. Chem. C*, 2007, **111**, 11760–11762. doi:10.1021/jp0750598.

[123] A. Suzuki, K. Kobayashi, T. Oku, and K. Kikuchi, *Mater. Chem. Phys.*, 2011, **129**, 236 – 241. doi:10.1016/j.matchemphys.2011.04.010.

[124] M. Urbani, M. Grätzel, M. Kh. Nazeeruddin, and T. Torres, *Chem. Rev.*, 2014, **114**, 12330–12396. doi:10.1021/cr5001964.

[125] K. J. Elliott, A. Harriman, L. Le Pleux, Y. Pellegrin, E. Blart, C. R. Mayer, and F. Odobel, *Phys. Chem. Chem. Phys.*, 2009, **11**, 8767–8773. doi:10.1039/B905548G.

[126] M. Ethirajan, Y. Chen, P. Joshi, and R. K. Pandey, *Chem. Soc. Rev.*, 2011, **40**, 340–362. doi:10.1039/B915149B.

[127] Y. Zhou, X. Liang, and Z. Dai, *Nanoscale*, 2016, **8**, 12394–12405. doi:10.1039/C5NR07849K.

[128] S.-K. Lee and I. Okura, *Analyst*, 1997, **122**, 81–84. doi:10.1039/A604885D.

[129] I. Okura, *J. Porphyrins Phthalocyanines*, 2002, **06**, 268–270. doi:10.1142/S1088424602000300.

[130] F. S. Woo, M. Cahiwat-Alquiza, and H. C. Kelly, *Inorg. Chem.*, 1990, **29**, 4718–4723. doi:10.1021/ic00348a027.

[131] O. Horváth, R. Huszánk, Z. Valicsek, and G. Lendvay, *Coord. Chem. Rev.*, 2006, **250**, 1792 – 1803. doi:10.1016/j.ccr.2006.02.014. 16th International Symposium on the Photochemistry and Photophysics of Coordination Compounds.

[132] M. Gouterman, *J. Mol. Spectrosc.*, 1961, 138–163. doi:10.1016/0022-2852(61)90236-3.

[133] M. Gouterman, *J. Mol. Spectrosc.*, 1963, 108–127. doi:10.1016/0022-2852(63)90011-0.

[134] D. Lamoen and M. Parrinello, *Chem. Phys. Lett.*, 1996, **248**, 309 – 315. doi:10.1016/0009-2614(95)01335-0.

[135] M.-S. Liao and S. Scheiner, *J. Chem. Phys.*, 2002, **117**, 205–219. doi:10.1063/1.1480872.

[136] M. Gouterman. *The Porphyrins, Physical Chemistry Part A*, vol. III, chapter 1, pages 1–165. Academic Press New York, 1978.

[137] J. M. García-Lastra, P. L. Cook, F. J. Himpsel, and A. Rubio, *J. Chem. Phys.*, 2010, **133**, 151103. doi:10.1063/1.3497188.

[138] F. Paulat and N. Lehnert, *Inorg. Chem.*, 2008, **47**, 4963–4976. doi:10.1016/j.chemphys.2007.02.021. PMID: 18438984.

[139] Martin Gouterman, *J. Chem. Phys.*, 1959, **30**, 1139–1161. doi:10.1063/1.1730148.

[140] S. Sorgues, L. Poisson, K. Raffael, L. Krim, B. Soep, and N. Shafizadeh, *J. Chem. Phys.*, 2006, **124**, –. doi:10.1063/1.2176612.

[141] S. C. M. Gandini, E. A. Vidoto, R. Nascimento, O, and M. Tabak, *J. Ionorg. Biochem.*, 2003, **94**, 127–137. doi:10.1016/S0162-0134(02)00615-3.

[142] S. B. Brown and I. R. Lantzke, *Biochem. J.*, 1969, **115**, 279–285. doi:10.1042/bj1150279.

[143] P. A. Adams, D. A. Baldwin, C. E. Hepner, and J. M. Pratt, *Bioinorg. Chem.*, 1978, **9**, 479 – 494. doi:10.1016/S0006-3061(00)80132-5.

[144] G. S. Collier, J. M. Pratt, C. R. De Wet, and C. F. Tshabalala, *Biochem. J.*, 1979, **179**, 281–289. doi:10.1042/bj1790281.

[145] E. F. Aziz, N. Ottosson, S. Bonhommeau, N. Bergmann, W. Eberhardt, and M. Chergui, *Phys. Rev. Lett.*, Feb 2009, **102**, 068103. doi:10.1103/PhysRevLett.102.068103.

[146] K. Atak, R. Golnak, J. Xiao, E. Suljoti, M. Pflüger, T. Brandenburg, B. Winter, and E. F. Aziz, *J. Phys. Chem. B*, 2014, **118**, 9938–9943. doi:10.1021/jp505129m. PMID: 25068599.

[147] C. Asher, K. A. de Villiers, and T. J. Egan, *Inorg. Chem.*, 2009, **48**, 7994–8003. doi:10.1021/ic900647y. PMID: 19572726.

[148] A. Marcelli, I. Jelovica Badovinac, N. Orlic, P. R. Salvi, and C. Gellini, *Photochem. Photobiol. Sci.*, 2013, **12**, 348–355. doi:10.1039/C2PP25247C.

[149] K. Kimura. *Handbook of HeI Photoelectron Spectra of Fundamental Organic Molecules: Ionization Energies, ab initio Assignments, and Valence Electronic Structure for 200 Molecules.* Japan Scientific Societies Press, 1981.

[150] T. B. Douglas, *J. Am. Chem. Soc.*, 1948, **70**, 2001–2002. doi:10.1021/ja01186a005.

[151] Y. Nakato, K. Abe, and H. Tsubomura, *Chem. Phys. Lett.*, 1976, **39**, 358 – 360. doi:10.1016/0009-2614(76)80095-4.

[152] S. C. Khandelwal and J. L. Roebber, *Chem. Phys. Lett.*, 1975, **34**, 355 – 359. doi:10.1016/0009-2614(75)85292-4.

[153] S. Kitagawa, I. Morishima, T. Yonezawa, and N. Sato, *Inorg. Chem.*, 1979, **18**, 1345–1349. doi:10.1021/ic50195a038.

[154] P. Jaramillo, K. Coutinho, B. J.C. Cabral, and S. Canuto, *Chem. Phys. Lett.*, 2011, **516**, 250 – 253. doi:10.1016/j.cplett.2011.10.016.

[155] R. Al-Obaidi, M. Wilke, M. Borgwardt, J. Metje, A. Moguilevski, N. Engel, D. Tolksdorf, A. Raheem, T. Kampen, S. Mähl, I. Yu. Kiyan, and E. F. Aziz, *New J. Phys.*, 2015, **17**, 093016. doi:10.1088/1367-2630/17/9/093016.

List of publications

Parts of this thesis have been published in the following article:

1. **Monochromatization of femtosecond XUV light pulses with the use of reflection zone plates**
   Jan Metje, Mario Borgwardt, Alexandre Moguilevski, Alexander Kothe, Nicholas Engel, Martin Wilke, Ruba Al-Obaidi, Daniel Tolksdorf, Alexander Firsov, Maria Brzhezinskaya, Alexei Erko, Igor Yu. Kiyan, and Emad F. Aziz
   Optics Express Vol. 22, Issue 9, pp 10747-10760 (2014),
   DOI: 10.1364/OE.22.010747

In addition to this thesis, I have contributed in the following articles during my PhD:

1. **Time-of-flight electron spectrometer for a broad range of kinetic energies**
   Alexander Kothe, Jan Metje, Martin Wilke, Alexandre Moguilevski, Nicholas Engel,Ruba Al-Obaidi, Clemens Richter, Ronny Golnak, Igor Yu. Kiyan, and Emad F. Aziz
   Review of Scientific Instruments Vol. 84, 023106 (2013)
   DOI: 10.1063/1.4791792

2. **Laser-assisted electron scattering in strong-field ionization of dense water vapor by ultrashort laser pulses**
   Martin Wilke, Ruba Al-Obaidi, Alexandre Moguilevski, Alexander Kothe, Nicholas Engel, Jan Metje, Igor Yu. Kiyan and Emad F. Aziz
   New Journal of Physics Vol. 16 083032 (2014)
   DOI: 10.1088/1367-2630/16/8/083032

3. **Ultrafast photoelectron spectroscopy of solutions: Space-charge effect**
   R. Al-Obaidi, M. Wilke, M. Borgwardt, J. Metje, A. Moguilevski, N. Engel, D. Tolksdorf, A. Raheem, I. Yu. Kiyan, E. F. Aziz, T. Kampen and S. Mähl
   New Journal of Physics Vol. 17 093016 (2015)
   DOI: 10.1088/1367-2630/17/9/093016

Abstract

Ultrashort laser pulses allow the investigation of electron dynamics in materials through a variety of time-resolved spectroscopical methods. Especially the application of transient photoelectron spectroscopy in a pump-probe scheme enables simultaneously the investigation of the binding energy of excited electronic states and their relaxation dynamics. To expand the application area of transient photoelectron spectroscopy, the extension of the available photon energies of the probe laser from the spectral range of UV light through the range of XUV radiation until the range of soft X-ray radiation, while at the same time conserving the characteristics of the ultrashort laser pulses stands in the focus of the technical development.

This thesis contributes to this field through the development and commissioning of a laser based setup for ultrafast pump-probe photoelectron spectroscopy of liquids. The setup enables the application of UV-IR pump-laser pulses and XUV probe-laser pulses. The XUV radiation is generated from femtosecond IR laser pulses in the nonlinear optical process of high harmonic generation in a rare gas. From the resulting XUV frequency comb, the 21^{st} harmonic of the IR laser is chosen for the spectroscopy experiment. Special care has been taken to preserve the ultrashort time duration of the XUV radiation upon monochromatizing the HHG spectrum. At the same time, the beamline was constructed with two optical elements only, in order to provide stable beam pointing, and a high throughput of photons. The result is a beamline, that consists of an ORZP monochromator, and a toroidal mirror. The ORZP is a new type of monochromator developed at the synchrotron BESSY II. It combines a high diffraction efficiency with a small elongation of the temporal profile of the XUV laser pulses. To evaluate the ORZP performance, the monochromatized XUV radiation has been systematically characterized with respect to focus size, spectral width and pulse duration at the point of the PES experiment.

In the second part of this work, the application of the XUV light source to two model systems was evaluated. The first system of aqueous sodium halide solutions serves as a model for ionic solvation, and were investigated with the use of static XUV PES. The study reveals that the HHG light source adds further aspects to existing synchrotron based studies. The second system of a hemin-DMSO solution serves as a model for natural, organic dyes in solution and was investigated with transient PES.

Kurzdarstellung

Ultrakurze Laserpulse ermöglichen über eine Vielzahl zeitaufgelöster Spektroskopieverfahren die Untersuchung der Elektronendynamik von Materialien. Insbesondere mittels des Anregungs-Abfrage-Schemas erlaubt transiente Photoelektronenspektroskopie die gleichzeitige Bestimmung von Bindungsenergien und Lebensdauern angeregter elektronischer Zustände. Um die Möglichkeiten transienter Photoelektronenspektroskopie auszubauen steht die Erweiterung der verfügbaren Photonenenergien vom Spektralbereich des UV-Lichts über den Bereich der XUV-Strahlung bis hin zu weicher Röntgenstrahlung, bei gleichzeitigem Erhalt der Lasercharakteristika, im Fokus der technischen Entwicklung.
Diese Arbeit trägt zu dem Feld durch die Entwicklung und Inbetriebnahme eines Versuchsaufbau für ultraschnelle Anregungs-Abfrage-Photoelektronenspektroskopie von Flüssigkeiten bei. Der Aufbau ermöglicht die Verwendung von UV-IR Laserpulsen zur Anregung und die Verwendung eines XUV Abfragelaser. Die XUV Strahlung wird durch den optisch nichtlinearen Prozess der Erzeugung hoher Harmonischer eines IR-Femtosekundenlasers in einem Edelgas gewonnen. Aus dem erzeugten XUV Frequenzkamm wird die 21ste Harmonische des IR-Lasers für das Spektroskopieexperiment ausgewählt. Besonderes Augenmerk lag dabei auf dem Erhalt der ultrakurzen Pulsdauer der XUV-Strahlung beim monochromatisieren des HHG Spektrums. Gleichzeitig wurde die Beamline mit wenigen optischen Elementen konstruiert, um eine möglichst stabile Strahllage und eine hohe Transmission von Photonen zu erreichen. Als Resultat entstand eine Beamline, die aus einem ORZP-Monochromator und einen Refokussierspiegel besteht. Die ORZP ist ein neuer Monochromatortyp, der am Synchrotron BESSY II entwickelt wurde. Er bietet eine hohe Beugungseffizienz bei gleichzeitiger geringer Verlängerung der XUV Laserpulse. Um die Leistung der ORZP zu bewerten, wurde die monochromatisierte XUV-Strahlung systematisch mit Hinblick auf Fokusgröße, Spektralbreite und Pulsdauer am Ort des PES-Experiments charakterisiert.
Im zweiten Teil dieser Arbeit wurde die Anwendung der XUV Lichtquelle auf zwei Modellsysteme untersucht. Im ersten System dienten wässrige Natriumhalogenidlösungen als Modell für die Solvatisierung von Ionen und wurden mittels statischer XUV PES untersucht. Die Studie zeigt die Möglichkeiten der HHG-Lichtquelle, weitere Beiträge zu synchrotronbasierten Studien zu leisten. Das zweite System einer Hämin-DMSO-Lösung dient als Modell für natürliche, organische Farbstoffe in Lösung und wurde mittels transienter PES untersucht.

Danksagung

Im Laufe meiner Doktorarbeit hat mich eine Reihe von Menschen auf die verschiedenste Art begleitet und unterstützt. Diesen Menschen möchte ich an dieser Stelle meinen Dank aussprechen.

Allen voran bedanke ich mich bei Prof. Emad Aziz für die Möglichkeit, meine Doktorarbeit in seiner Forschungsgruppe am Helmholtz-Zentrum Berlin durchführen zu können. Er hat mich während der Zeit immer unterstützt und mir die Freiheit gelassen, meine Ideen für den Versuchsaufbau umzusetzen.

Außerdem möchte ich mich bei Prof. Bernd Abel für seine Bereitschaft bedanken, als Zweitgutachter für meine Arbeit zur Verfügung zu stehen und diese so zeitnah zu bewerten sowie als Mitglied der Prüfungskommission meiner Disputation zur Verfügung zu stehen und dafür extra aus Leipzig nach Berlin anzureisen.

Die wissenschaftlichen Gespräche mit Prof. Alexei Erko über die Zonenplatte während der Planung unseres Experiments habe ich sehr geschätzt. Darüber hinaus bedanke ich mich bei Ihm für die Einführung in die Technik des Raytracing.

Bei Dr. Igor Kiyan bedanke ich mich für die Leitung unseres Labors, für die individuelle Betreuung während allen Phasen meiner Promotion und für die vielen Anregungen, die er mir in der Zeit gegeben hat.

Allen aktuellen und ehemaligen Doktoranden und Masterstudenten des Laserlabors danke ich für die gemeinsame Zeit und die Unterstützung, die wir uns bei den Experimenten zukommen lassen haben.

Insbesondere möchte ich mich bei Martin Wilke bedanken für seine Fähigkeit, immer wieder Denkanstöße zu allen möglichen Fragen zu geben und für seine Bereitschaft, als studentisches Mitglied meiner Prüfungskommission zur Verfügung zu stehen.

Mario Borgwardt danke ich für die Zusammenarbeit während der wirklich wichtigen Zeit der Charakterisierung der Zonenplatte und für die Einführung in Mathematica.

Für die vielen kleinen und großen Hilfen sowie die Gespräche im gemeinsamen Büro möchte ich mich bei Dr. Ruba Al-Obaidi bedanken. Außerdem bedanke ich mich bei ihr und Azhr Raheem dafür, dass sie meine vielen Fragen zum Islam und zur Kultur des Irak so geduldig beantwortet haben.

Bei Alexandre "Sascha" Moguilevski bedanke ich mich für die gemeinsame Arbeit mit dem Laser und die Diskussionen über Laser und Optik.

Für die Einführung in Python und für das umfangreiche Messprogramm unseres Pump-Probe-Experiments möchte ich mich bei Daniel Tolksdorf bedanken.

Dr. Ronny Golnak danke ich für die vielen Gespräche und Tipps bei allen technischen Fragen und die gemeinsame Zeit, die wir außerhalb von HZB und Physikinstitut verbracht haben.

Bei Rudolf Ringel bedanke ich mich für die Konstruktion der Vakuumkammern und Manipulatoren sowie die technischen Gespräche, die wir rund um dieses Thema geführt haben.

Bedanken möchte ich mich außerdem bei Dipl. Ing. Detlef Müller und seinem Team der Feinwerktechnik des Physikinstituts der Freien Universität Berlin für die Anfertigung der Vakuumkammern und Manipulatoren sowie für alle kleineren und größeren technischen Hilfen, mit denen sie unser Projekt begleitet haben.

Mein besonderer Dank gilt Dr. Sven Strickroth für die Zeit, in der wir uns getroffen haben um unsere Doktorarbeiten zu schreiben, für alle möglichen Tipps und Kniffe beim Programmieren und bezüglich TeX-Befehlen sowie für die Zeit, die wir neben unseren Doktorarbeiten miteinander verbracht haben.

Nicht zuletzt möchte ich meinen Eltern sowie Christiane und Olivia meinen herzlichen Dank aussprechen! Die unablässige Unterstützung, die ich auf meinem Lebensweg von Euch bekommen habe ist ein großartiges Geschenk.

Selbstständigkeitserklärung

Hiermit versichere ich, die vorliegende Arbeit selbstständig und ausschließlich unter Benutzung der angegebenen Quellen und Hilfsmittel verfasst zu haben.

Ich erkläre weiterhin, dass die vorliegende Arbeit nicht im Rahmen eines früheren Promotionsverfahrens an einer anderen Stelle eingereicht worden ist.
Berlin, den 15.09.2016

Jan Metje